ESTIMATING SUBMARINE GROUNDWATER DISCHARGE IN THE CILICIAN BASIN BY RADIOACTIVE ISOTOPE TRACERS AND HYDRODYNAMIC MODELING

A THESIS SUBMITTED TO
THE GRADUATE SCHOOL OF MARINE SCIENCES
OF
MIDDLE EAST TECHNICAL UNIVERSITY

BY

BURAK KUYUMCU

IN PARTIAL FULFILLMENT OF THE REQUIREMENTS
FOR
THE DEGREE OF MASTER OF SCIENCE
IN
OCEANOGAPHY

JULY 2023

Approval of the thesis:

ESTIMATING SUBMARINE GROUNDWATER DISCHARGE IN THE CILICIAN BASIN BY RADIOACTIVE ISOTOPE TRACERS AND HYDRODYNAMIC MODELING

submitted by **BURAK KUYUMCU** in partial fulfillment of the requirements for the degree of **Master of Science** i**n Oceanography, Middle East Technical University** by,

Prof. Dr. Barış Salihoğlu
Director, **Institute of Marine Sciences, METU** _____

Prof. Dr. Bettina A. Fach-Salihoğlu
Head of the Department, **Oceanography, METU** _____

Assoc. Prof. Dr. Ekin Akoğlu
Supervisor, **Marine Biology and Fisheries, METU** _____

Assist. Prof. Dr. Korhan Özkan
Co-Supervisor, **Marine Biology and Fisheries, METU** _____

Examining Committee Members:

Prof. Dr. Zübeyde Hatipoğlu Bağcı
Department of Geological Engineering, Mersin University _____

Assoc. Prof. Dr. Ekin Akoğlu
Marine Biology and Fisheries, METU _____

Assist. Prof. Dr. Korhan Özkan
Marine Biology and Fisheries, METU _____

Assist. Prof. Dr. Nüvit Berkay Başdurak
Oceanography, METU _____

Assoc. Prof. Dr. Koray Özhan
Oceanography, METU _____

Date: 26.07.2023

I hereby declare that all information in this document has been obtained and presented in accordance with academic rules and ethical conduct. I also declare that, as required by these rules and conduct, I have fully cited and referenced all material and results that are not original to this work.

Name Last name : Burak Kuyumcu

Signature :

ABSTRACT

ESTIMATING SUBMARINE GROUNDWATER DISCHARGE IN THE CILICIAN BASIN BY RADIOACTIVE ISOTOPE TRACERS AND HYDRODYNAMIC MODELING

Kuyumcu, Burak
Master of Science, Oceanography
Supervisor: Assoc. Prof. Dr. Ekin Akoğlu
Co-Supervisor: Assist. Prof. Dr. Korhan Özkan

July 2023, 132 pages

The Northeastern Levantine Sea has an oligotrophic nature, however, rising agricultural and industrial activities along its coasts pose a major eutrophication risk. There is a urgent necessity to identify and assess coastal water and nutrient inputs in order to have effective ecosystem management. In this study, submarine groundwater discharge rates and associated nutrient fluxes into the Cilician Basin were estimated for the first time, utilizing a 228-Radium mass-balance approach and numerical modeling. Two basin-wide cruises were conducted (April 2022 & September 2022) in addition to two catchment surveys (March 2022 & September 2022) to obtain Radium and nutrient samples for seawater (#207 samples both), rivers (#28 samples both), and groundwater (#33 samples both) in 2022. A box model was established, defining each source and sink of 228-Radium activities measured by gamma spectrometry. Nutrient loads were determined by integrating estimated fluxes with the median nutrient concentrations in groundwater samples. Moreover, a Lagrangian particle tracking model was utilized to estimate the residence time of the basin, which then used in the offshore water exchange

calculations in the mass balance equation. The outcome of the model indicated there was substantial seasonal and interannual variation in the residence time, particularly for the surface layer, 0-150 m depth. The highest variation was found between the wet and dry season of 2019 with 24 and 74 days, respectively, for the surface layer. The gamma spectrometry results yielded approximately 24.97 x 10^{13} dpm 228-Radium inventory in the defined box for the wet season, and the inventory of İskenderun bay was found as 5.57 x 10^{12} dpm. There was significant 228-Radium enrichment in the basin, especially in the İskenderun bay and near the western boundary. The mass balance revealed that the submarine groundwater discharge may have contributed at least 121 km^3 per year to the water budget the Cilician Basin where the total annual riverine discharge was approximately 13 km^3. A large range of groundwater endmember 228-Radium activity was determined using both the literature data and groundwater activities measured within this study. The highest endmember activity was used for the most conservative submarine groundwater discharge rate and the lowest activity was used to calculate maximum discharge estimates. Correspondingly, submarine groundwater discharge associated nutrient loads were 0.27, 37.73, and 50.92 kT/year of PO_4-P, DIN-N, and SiO_4-Si, respectively, in the most conservative scenario. Comparison with riverine nutrient loads calculated by one wet season and one dry season sample for each river indicated the submarine groundwater discharge corresponded to at least 66%, 106%, and 96% of riverine P-PO_4, DIN-N, and SiO_4-Si inputs, respectively, using a conservative approach. Furthermore, the elevated dissolved inorganic nitrogen to phosphate ratio of 139 found for the groundwater suggested that it might be a contributing factor to the severe phosphorus limitation in the area. Therefore, it may have an effect on primary production by changing the structure of phytoplankton communities and the interaction between trophic levels. The study emphasized that the submarine groundwater discharge might have a fundamental role in the water and nutrient budgets of the Cilician Basin despite the caveats regarding temporal variations and the wide range of groundwater end-member activities, as no saline

groundwater sample was sampled in the study. Further investigation is required to have a better understanding on the spatiotemporal variations in submarine groundwater discharge and its potential effects on primary production as significant fluctuations might occur due to the variations in residence time and nutrient concentrations.

Keywords: Cilician Basin, Land-sea interactions, Radium, Residence time, Submarine groundwater discharge

ÖZ

KİLİKYA BASENİNDE DENİZALTI SU ÇIKIŞLARININ RADYOAKTİF İZOTOP İZLEYİCİLER VE HİDRODİNAMİK MODELLEME İLE TAHMİN EDİLMESİ

Kuyumcu, Burak
Yüksek Lisans, Oşinografi (Deniz Bilim)
Tez Yöneticisi: Doç. Dr. Ekin Akoğlu
Ortak Tez Yöneticisi: Dr. Öğr. Üyesi Korhan Özkan

Temmuz 2023, 132 sayfa

Kuzeydoğu Levant Denizi'nin oligotrofik yapısına rağmen, kıyı bölgelerinde sürekli artmakta olan endüstriyel ve tarımsal faaliyetler ciddi bir ötrofikasyon riski oluşturmaktadır. Etkili bir ekosistem yönetimine sahip olmak için kıyısal su ve besin girdilerinin belirlenmesi ve değerlendirilmesi acil bir gerekliliktir. Bu çalışmada, 228-Radyum kütle dengesi yaklaşımı ve sayısal modelleme kullanılarak, Kilikya Havzası'na denizaltı su çıkışları ve buna bağlı besin tuzu akışları ilk kez tahmin edilmiştir. Deniz suyu (207 adet), nehirler (28 adet) ve yeraltısularından (33 adet) besin tuzu ve Radyum örnekleri elde etmek amacıyla, 2022 yılında iki (Mart 2022 & Eylül 2022) havza örnekleme çalışmasına ek olarak, iki de (Nisan 2022 & Eylül 2022) basen çapında deniz araştırma seferi gerçekleştirilmişir. Gama spektrometrisi ile ölçülen 228-Radyum girdi ve çıktıları belirlenerek bir kutu model oluşturulmuştur. Besin tuzu yükleri, tahmini akıların yeraltı suyu numunelerindeki besin tuzu konsantrasyonlarının medyanları ile entegre edilmesiyle belirlenmiştir. Ayrıca, kütle dengesi denkleminde açık deniz su değişimi hesaplarında kullanılmak üzere, havzanın su ikamet süresini tahmin etmek için bir Lagrangian parçacık izleme

modeli kullanılmıştır. Modelin sonucu, özellikle 0-150 m derinlikteki yüzey tabakası için, ikamet süresinde önemli mevsimsel ve yıllar arası değişkenlik olduğunu göstermiştir. En yüksek varyasyon, yüzey tabakası için sırasıyla 24 ve 74 gün ile 2019 yılının yağışlı ve kurak mevsimi arasında bulunmuştur. Gama spektrometri sonuçları, ıslak mevsim için Kilikya Baseni'nde tanımlanan kutuda yaklaşık 24.97 x 10^{13} dpm 228-Radyum envanteri olduğunu göstermiş, İskenderun Körfezi envanteri ise 5.57 x 10^{12} dpm olarak hesaplanmıştır. Havzada, özellikle İskenderun Körfezi'nde ve batı sınırına yakın bölgelerde önemli ölçüde 228-Radyum zenginleşmesi gözlemlenmiştir. Kütle dengesi, denizaltı su çıkışlarının, toplam yıllık nehir deşarjının yaklaşık 13 km^3 olan Kilikya Baseni su bütçesine yılda en az 121 km^3 katkıda bulunabileceğini ortaya koymuştur. Hem literatür verileri hem de bu çalışmada ölçülen yeraltı suyu aktiviteleri kullanılarak geniş aralıklı yeraltı suyu uç 228-Radyum aktivite aralığı belirlenmiştir. En korunumlu denizaltı su çıkışı miktarı için en yüksek yeraltı suyu uç aktivitesi ve maksimum deşarj tahminlerini hesaplamak için en düşük aktivite kullanılmıştır. Buna bağlı olarak, en korunumlu senaryo için, denizaltı suyu çıkışı ile ilişkili besin tuzu yükleri PO_4-P, DIN-N ve SiO_4-Si için sırasıyla 0.27, 37.73, ve 50.92 kT/yıl olarak tahmin edilmiştir. Her nehir için bir ıslak mevsim ve bir kuru mevsim numunesi ile hesaplanan nehir besin yükleri ile karşılaştırma, korunumlu bir yaklaşımla tahmin edilen denizaltı suyu çıkışlarının, nehir kaynaklı P-PO_4, DIN-N ve SiO_4-Si besin tuzlarının sırasıyla en az %66, %106 ve %96'sına karşılık gelebileceği göstermiştir. Ayrıca, yeraltı suyu için bulunan toplam inorganik azotun fosfata oranının 139 olması, bunun bölgedeki ciddi fosfor sınırlamasına katkıda bulunan bir faktör olabileceğini öne sürmektedir. Bu nedenle, denizaltı su çıkışlarının fitoplankton topluluklarının yapısını ve trofik seviyeler arasındaki etkileşimi değiştirerek birincil üretim üzerinde etkisi olabilir. Bu çalışma, zamansal değişimlere ve tuzlu yeraltı suyu örneklenmemesi sebebiyle kabul edilen geniş yeraltı suyu uç aktivite aralığına rağmen, denizaltı suyu çıkışlarının Kilikya Baseni'nin su ve besin tuzu bütçelerinde temel bir role sahip olabileceği vurgulamıştır. Su ikamet süresi ve besin tuzu konsantrasyonlarındaki değişiklikler

nedeniyle önemli dalgalanmalar meydana gelebileceğinden, denizaltı su çıkışlarının mekansal-zamansal değişimleri ve birincil üretim üzerindeki potansiyel etkilerini daha iyi anlamak için daha fazla araştırmaya ihtiyaç vardır.

Anahtar Kelimeler: Kilikya Baseni, Kara-deniz etkileşimleri, Radyum, Su ikamet süresi, Denizaltı su çıkışları

To my everlasting source of love and strength — my family.

ACKNOWLEDGMENTS

I am grateful to my supervisor Assoc. Prof. Dr. Ekin Akoğlu, whose insightful guidance and expertise have been invaluable throughout this research.

I also extend my appreciation to my co-supervisor, Assist. Prof. Dr. Korhan Özkan, for his visionary leadership, expert guidance, and insightful critiques.

I would like to express my sincere thanks to Assoc. Prof. Dr. Koray Özhan, Assoc. Prof. Dr. Süleyman Fatih Özmen, Prof. Dr. Kanchan Maiti, Assist Prof. Dr. Nüvit Berkay Başdurak, Prof. Dr. Zübeyde Hatipoğlu Bağcı, Prof. Dr. Serdar Bayari, Dr. Hasan Örek, Prof. Dr. Bettina Fach Salihoğlu, Dr. Yeşim Ak Örek, Prof. Dr. Süleyman Tuğrul, Prof. Dr. Ahmet Cevdet Yalçıner, Prof. Dr. Erik Jeppesen and Prof. Dr. Meryem Beklioğlu for their guidance and support.

A special note of gratitude goes to my Aquatic Ecology research group, which has fostered an environment of collaboration. I would like to express my appreciation to Serhat Ertuğrul, İdil Ilgaz Kaya, Yeşim Ayar, Meltem Koru, Hasan Arslan, Tekin Yılmaz, Dr. Mustafa Korkmaz, Eric Rayne, Dr. Hassan Al-Najjar, Dr. Md. Masum Billah, Onat Arıkan, Kardelen Anık, and Ali Değermenci for their sincere friendship.

I would also like to acknowledge Aquatic Ecosystem MOdeling Network – Junior (AEMON-J). In particular, Dr. Michael Meyer, your support and friendship have been invaluable.

I would also like to express my gratitude to Buse Uysaler for her continuous support.

I want to express my heartfelt gratitude to Serim Doğaç Sayar for his exceptional companionship and unwavering support. I would like to especially acknowledge Gözde Yılmaz Sayar, whose support has held immense significance for me.

I extend my gratitude to Ahmet Bedirhan Işık, Alperen Kuzu, and Hasan Ödemiş for their camaraderie, unwavering support during challenging periods, and the multitude of memories.

I wish to thank Can Güneş, Mertcan Esti, Ahmet Acet, Halil Ceylan, Mehmet Gökhan Aygün, Şuayip Irgav, Batu Kiseli, Alper Çağal, İbrahim Eseroğlu, Emre Yiğit, Muhammed Yusuf Öztürk, Harun Çimener, and Servet Meriç Kürşad for their friendship and support.

I also thank the R/V Bilim-2 crew and the chemistry laboratory staff.

In this heartfelt acknowledgment, I want to honor the profound influence of my uncle, Tarkan Terzioğlu. His legacy continues to serve as a fount of motivation, underscoring his extraordinary character and the resilience he instilled in me.

I extend my deepest gratitude to my mother Işıl Kuyumcu, my father Haluk Kuyumcu, and my brother Furkan Kuyumcu. Anneme, babama ve kardeşime destekleri, anlayışları ve bana olan inançları için teşekkür ederim.

I want to sincerely convey my feelings to my dearest, Meltem Koru, who has always been my unwavering supporter through her boundless love.

Lastly, I am indebted to the many individuals who have left their mark on my academic journey, whether through profound discussions or simple gestures of kindness.

This work is partially funded by the Scientific and Technological Research Council of Türkiye under grant number 120Y082, METU BAP TEZ-YL-701-2023-11121, and the Marine Ecosystem and Climate Research Center (DEKOSIM).

TABLE OF CONTENTS

LIST OF TABLES

LIST OF FIGURES

FIGURES

LIST OF ABBREVIATIONS

AD: Anno Domini

AMC: Asia Minor Current

ANOVA: Analysis of Variance

AR: Activity Ratio

BC: before Christ

C: Centigrade

CMEMS: Copernicus Marine Environment Monitoring Service

CTD: Conductivity-Temperature-Depth

DEKOSIM: Marine Ecosystem and Climate Research Center

DIN: Dissolved Inorganic Nitrogen

DIP: Dissolved Inorganic Phosphorus

DL: Deep Layer

DO: Dissolved Oxygen

dpm: Disintegration per minute

DW: Deep Water

EMDW: Eastern Mediterranean Deep Water

GEBCO: The General Bathymetric Chart of the Oceans

IL: Intermediate Layer

keV: kiloelectron-volts

kg: kilogram

km: kilometer

kT: kiloTon

L: Liter

lat: latitude

LE: Lattakia Eddy

LEC: Libyo-Egyptian Current

LIW: Levantine Intermediate Water

lon: longitude

LSU: Louisiana State University

LSW: Levantine Surface Water

m: meter

M: Molar

MAW: Modified Atlantic Water

METU: Middle East Technical University

min: minute

ml: milliliter

MMJ: Mid-Mediterranean Jet

N: Nitrogen

NH_4: Ammonium

nm: nanometer

NO_2: Nitrite

NO_3: Nitrate

P: Phosphorus

PO_4: Phosphate

ppt: parts per thousand

RT: Residence Ti

SC: Specific Conductivity

SGD: Submarine Groundwater Discharge

Si: Silicon

SiO_4: Silicate

SL: Surface Layer

TARD: Total Annual River Discharge

TARLA: Turkish Acceleration and Radiation Laboratory

TIN: Total Inorganic Nitrogen

TSS: Total Suspended Solids

TUBITAK: The Scientific and Technological Research Council of Turkey

vs: versus

WMDW: Western Mediterranean Deep Water

yr: year

CHAPTER 1

INTRODUCTION

Water is the most important resource which life on earth is strongly dependent on. The vast majority of the approximately 1.4×10^9 km³ (Maidment, 1993) water on our planet is the ocean, and it is very laborious and expensive to treat this salty water to be used for drinking, agricultural or other fresh water needs. For this reason, humans are making an effort to use readily available freshwater reservoirs on earth or underground. The majority of available fresh water constitutes a small amount of the total water budget and is found in glaciers and groundwater. The amount of fresh groundwater is about 100 times that of surface fresh water, but it is not as easy to access and use (Fitts, 2013). In recent years, as a result of the development and increasing value of water resources management methods, an increasing number of studies focused on groundwater. Accordingly, the significance of groundwater in the global water cycle and its impact on the mass balances of water, nutrients, and other elements has become clearer (Zektser et al., 2006). Quantifying the exact amount of groundwater flux has significant challenges, therefore, a high degree of uncertainty and margin of error have existed in the amount of groundwater estimations used in the water budget calculations until the beginning of the 2000s (Zektser et al., 2006). Especially in the last two decades, with the development of various measuring devices and methods, groundwater studies have gained momentum, and land-sea interactions have begun to be studied more comprehensively and accurately in terms of biological, physical, and chemical aspects (Santos et al., 2021; Taniguchi et al., 2019).

Submarine groundwater discharge studies are challenging due to the heterogeneous distribution of submarine groundwater discharges in time and space (Taniguchi et al., 2019). Furthermore, direct measurements are almost impossible because groundwater is in contact with very complex systems, and there are various

independent factors affecting its composition and amount, such as catchment geology, hydrological factors, and anthropogenic activities (Burnett et al., 2006; Moore, 2010; Santos et al., 2021; Taniguchi et al., 2019). The significance of submarine groundwater discharges are known, but is mostly ignored in water budget calculations due to the difficulties mentioned above. Kohout (1966) noted that the Roman philosopher, historian, and geographer Strabo (63 BC to AD 21) mentioned a submarine spring in the Mediterranean off the coast of Latakia, Syria. In addition, the existence and use of submarine groundwater in the Black Sea, with its sources dating back to the 1st century AD, was mentioned (Pliny the Elder, 1st century AD) (Taniguchi et al., 2002).

Submarine Groundwater Discharge (SGD) is defined as the outflows directly from the seafloor, regardless of its drivers and content (Burnett et al., 2003). The main factors contributing to the SGD are the hydraulic gradient between the land and the sea, the circulation caused by the tidal currents or waves, the density gradient due to the salinity difference, the temporal changes of the sea level and in-aquifer dynamics, and the pore water movements (George et al., 2020; Michael et al., 2011; Santos et al., 2012; Taniguchi et al., 2019). Garcia-Orellana et al. (2021) divided the pathways of SGD into five groups according to the characteristics of these factors: Terrestrial groundwater discharge, density-driven seawater circulation, seasonal exchange of seawater, shoreface circulation of seawater and centimeter-scale porewater exchange (Figure 1.1). Terrestrial groundwater discharge and density-driven seawater circulation contain freshwater and only these two provide a net water input to the sea (Garcia-Orellana et al., 2021). Other pathways are caused by recirculation and are generally considered saline SGD (Garcia-Orellana et al., 2021; Taniguchi et al., 2002). In addition, fresh and saline SGD can be mixed with hydrodynamic processes and brackish SGD can be seen in the open sea (Santos et al., 2021). All these processes have different temporal and spatial scales. Porewater movements are usually on the centimeter scale and have a temporal scale range from seconds to hours (Taniguchi et al., 2019). On the other hand, seasonal sea level and aquifer

fluctuations can have time scales ranging from tens of meters to days and months (Taniguchi et al., 2019).

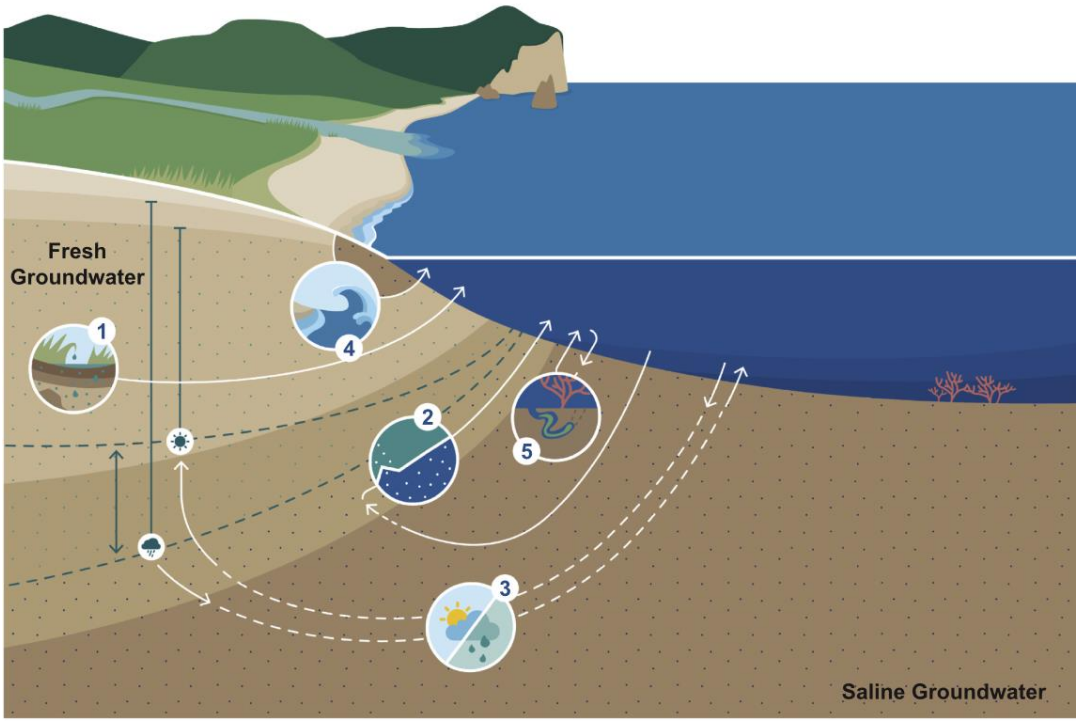

Figure 1.1. Schematic depiction of an unconfined coastal aquifer with key Submarine Groundwater Discharge channels subdivided by driving mechanism: 1) Terrestrial groundwater discharge (typically fresh groundwater); 2) Density-driven seawater circulation; 3) Seasonal exchange of seawater; 4) Shoreface seawater circulation; and 5) centimeter-scale porewater exchange (taken from Garcia-Orellana et al., 2021)

Groundwater usually contains high amounts of nutrients (Lecher et al., 2015; Rodellas et al., 2015; Santos et al., 2021), metals (Mayfield et al., 2021; Trezzi et al., 2017) and pollutants (B. A. Anderson et al., 2010; Fan et al., 2009; Knee & Paytan, 2012). The high amounts of nutrients can contribute algal blooms and eutrophication with the increase of anthropogenic pressures such as agricultural activities, industrial pollution, and land use changes (Hu et al., 2006; Hwang et al., 2005; Lecher et al., 2017). Groundwater, which generally has a high dissolved inorganic nitrogen (DIN) to dissolved inorganic phosphorus (DIP) ratio (>16), increases primary production by reducing nitrogen limitation in coastal waters (Beusen et al., 2013; Santos et al., 2021). Enhanced primary productivity reduces water quality, and may cause

hypoxic/anoxic conditions and damage to fish and invertebrate habitats (Montiel et al., 2019; Paerl & Otten, 2013). However, submarine groundwater discharge does not always contribute to adverse conditions. Studies in Obama Bay, Japan (Utsunomiya et al., 2017) and the Mauritius tidal region have found that submarine groundwater discharge can have positive effects on fish by increasing the growth rates (Lilkendey et al., 2019).

The effects of submarine groundwater discharge may vary based on different discharge rates and nutrient loads. Although the effects of SGD are widespread, the spatiotemporal heterogeneity necessitates research at high temporal and spatial scales in a study area. Hydrological and meteorological conditions in different seasons, geophysical and morphological structures of aquifers, anthropogenic factors, especially agricultural and industrial pressures, are the main reasons for this heterogeneity seen in submarine groundwater discharge. Changing climatic conditions and increasing anthropogenic pressures have given substantial importance to SGD studies in terms of accurate determination of water, nutrients, and metal budgets.

The Mediterranean basin has many submarine aquifers, and thus, needs special attention as SGD contributes significantly to the water and nutrient budgets (Bayari et al., 2011; Luijendijk et al., 2020; Rodellas et al., 2015). The basin was formed due to the geological changes in the Tethys Ocean floor caused by the movements of the African and Arabian plates over time (Bakalowicz, 2015). The continental margins have been the setting of extensive carbonate formation under tropical climate since the Late Triassic and Mediterranean karsts have formed millions of years of subaerial exposure during the Late Jurassic, Early Cretaceous, Oligocene and Miocene (Bakalowicz, 2015). Karst, which is ubiquitous in the region, generally forms karst springs with 10-20 m^3/s flow rate and is the main source of intense groundwater outflows (Zektser & Everett, 2004). Surface water and rain water can drain directly from the cavities of the structure in the karstic geography, resulting a high amount of observed groundwater discharges. In karstic carbonate regions, where SGD is typically transmitted to the ocean through cracks or preferred flow ways, fresh

groundwater might be the main SGD component locally (Santos et al., 2021). In regions with high karst content, such as the Mediterranean drainage basin, SGD can have major effects on alkalinity (Kolker et al., 2021). Kolker et al. (2021) concluded that fresh portion of SGD (FSGD) has a substantial impact on the total alkalinity budget of the Eastern Mediterranean Sea especially in the winter. They estimated that FSGD may contribute to the marine water budget up to 37% and 30% of the riverine input and the input from Black Sea to the total alkalinity budget respectively (Kolker et al., 2021). Furthermore they estimated the total alkalinity of 4656-6984 μmol kg^{-1} for the Mersin-Erdemli basin coastal aquifers based on the study of Demirel and Güler (Demirel & Güler, 2006). Although the SGD contributes to the alkalinity budget, some studies show that it may lower the pH. Low-pH groundwater may have a strong impact on the coastal systems and can cause coastal acidification (Cardenas et al., 2020; De Weys et al., 2011; Wang et al., 2014).

Mediterranean Sea is oligotrophic by nature due to its anti-estuarine circulation and limited nutrient inputs (Béthoux et al., 1998). Nutrient-poor Atlantic Surface Water flows into the Mediterranean Sea through the Gibraltar Street. This water mass, which moves eastward to balance the high amount of evaporation (~700 mm/year net loss) in the Mediterranean, becomes warmer and saltier as it progresses, and cools and condenses in winter, forming Levantine Intermediate Water (LIW) with down-welling (Alhammoud et al., 2005; Mariotti et al., 2002; Powley et al., 2017). Other main water masses are Atlantic or Modified Atlantic Water and Deep water (Figure 1.2). The deep waters are divided by Strait of Sicily into Western Mediterranean Deep Water (WMDW) and Eastern Mediterranean Deep Water (EMDW). EMDW is the most stagnant water mass in the entire Mediterranean Sea with a residence time of approximately 150 years (Powley et al., 2016). The thermohaline circulation causes bioavailable nutrients to exit the Strait of Gibraltar back to the Atlantic Ocean before returning to the photic zone (Alhammoud et al., 2005; Malanotte-Rizzoli et al., 2014; Powley et al., 2017). Therefore, LIW is very important not only for the Mediterranean but also for the biogeochemistry of the Atlantic Ocean. One of the regions where the formation of this important layer is the Cilician Basin

(Northeastern Levantine Basin) (Fach et al., 2021; Ozsoy et al., 1993; Sur et al., 1992).

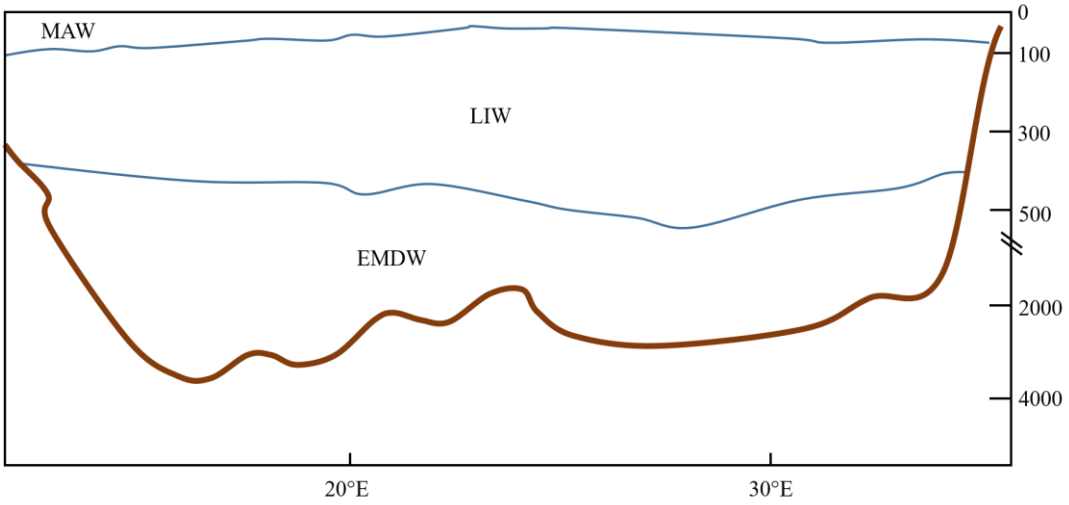

Figure 1.2. Mediterranean Water Masses (modified from Alhammoud et al., 2005) (y-axis depicts depth as meters)

Any nutrient inputs from land or atmosphere are likely to have a substantial impact on the biogeochemistry of the Mediterranean Sea because of its oligotrophic character (Rodellas et al., 2015). Despite the oligotrophic conditions in the open waters, eutrophic regions with high seasonal primary production can be observed in the coastal areas in the Cilician Basin (Akçay et al., 2018; Yilmaz et al., 1992).

In a recent numerical modelling study, maximum and minimum fresh submarine groundwater discharge in the Cilician Basin are estimated to be 250.09 x 10^6 m^3/yr and 0.72 x 10^6 m^3/yr, respectively, with the best estimation equals to 75.34 x 10^6 m^3/yr (Luijendijk et al., 2020). Rodellas et al. (2015) demonstrated that the total SGD contributes up to (0.3–4.8) x 10^{12} m^3 y^{-1} to the Mediterranean Sea, which is equal to or greater than the riverine discharge by a factor of 16. Furthermore, they showed the significant nutrient contribution of SGD with high DIN to DIP ratios (80-430), by flux rates of 190 x 10^9, 0.7 x 10^9 and 110 x 10^9 moles per year for nitrogen, phosphorous, and silica, respectively, which are comparable to riverine and atmospheric inputs (Rodellas et al., 2015). The high DIN:DIP ratios suggest that, in addition to atmospheric deposition (Krom et al., 2010), SGD might be a substantial

factor for phosphorus limitation in the Mediterranean Sea which has an approximate nitrate (NO_3^-) to phosphate (PO_4^{3-}) ratio of 28 in the deep water (Krom et al., 2004). The phosphorus limitation is stronger in the Eastern Mediterranean Sea (Pujo-Pay et al., 2011). Krom et al. (2010) have found that the phosphorus limitation is associated with the nutrient inputs (i.e. atmospheric and riverine nutrient loads) in the Eastern Mediterranean Sea rather than diazotrophic nitrogen fixation. This supports the hypothesis that the SGD can be one of the important drivers of the phosphorus limitation in the area. Additionally, the DIN:DIP ratios of 60 and 690 measured in SGD from Dor Beach and Haifa, Israel, respectively, can be further indications of the importance of SGD in the Levantine Sea (Weinstein et al., 2006, 2011).

The nutrient input from rivers and atmospheric deposition is a significant driver of eutrophication in the Levantine Sea, which can cause harmful algal blooms, oxygen depletion, and other negative impacts (Anderson et al., 2002; Paerl, 1997). However, the role of SGD as a source of nutrients and its potential impact on coastal eutrophication remain poorly understood.

The objective of this study is to quantify the submarine groundwater discharge and associated nutrient fluxes in the Cilician Basin by using 228-Radium isotope (^{228}Ra) mass balance approach by i) estimating a residence time for the Cilician Basin water masses to quantify the mixing of basin waters with the open sea in order to account for the major loss term in the ^{228}Ra mass balance considering its half-life (5.75 years); ii) establishing well-defined ^{228}Ra inventories for the Cilician Basin and İskenderun Bay as well as the ^{228}Ra activities of surrounding surface waters and groundwater; iii) quantifying the submarine groundwater discharge by constructing a ^{228}Ra mass balance assuming steady-state; and iv) determining nutrient fluxes associated with the submarine groundwater discharge and evaluate its potential impacts on the primary production.

Therefore, this study's results will help fill this knowledge gap, especially regarding prevalent phosphorus limitation, which can be strongly sustained by SGD. Moreover, this is the first study to unravel the SGD rates and associated nutrient fluxes in the region as SGD might be the key element in establishing a well-defined

water and nutrient budget in the Cilician Basin. Thus, it will improve our understanding of the biogeochemical and hydrological dynamics in the Cilician Basin including nutrient cycling, water quality, and coastal acidification. Overall, this study's findings will improve our understanding of the biogeochemical processes occurring in the region, which is necessary to manage and conserve coastal ecosystems sustainably.

CHAPTER 2

MATERIAL & METHODS

2. 1. Study Area

The study area is the Cilician Basin, Northeastern Mediterranean Sea, including İskenderun Bay (Gulf of Alexandretta) and Mersin Bay (Figure 2.1), where intense agricultural and industrial activities occur along its catchments (Güler et al., 2012; Isola et al., 2017; Polat, 2007). It has a mean depth of ~520 m and surface area of ~28,000 km². The Cilician Basin and the Latakia Basin connect via a 700-meter-deep waterway located almost halfway between Cyprus and İskenderun Bay (Ozsoy et al., 1993).The circulation dynamics dominated by year-long persistent Asia Minor Current, which is the northern branch of Mid-Mediterranean Jet (Robinson et al., 1991) or Libyo-Egyptian Current (Menna et al., 2021) (Figure 2.1). The area's circulation is influenced by the current's meanders and the mesoscale eddies that spiral out (Fach et al., 2021; Robinson et al., 2001). Furthermore, spatiotemporal variations in recurrent yet not permenant Latakia eddy might play an important role in the circulation dynamics of the area (Robinson et al., 1991). The basin has four main water masses: Levantine Surface Water (LSW), Mediterranean Atlantic Water (MAW), LIW, and Deep Water (DW). Heat and high evaporation rates generates this thin surface layer in summer, characterized by its high salinity and temperature (Hecht et al., 1988). LSW is carried by the Asia Minor Current as it flows westward into the Aegean Sea (Alhammoud et al., 2005). In addition, the Cilician Basin has been shown to be a potential formation place for LIW (Fach et al., 2021; Ozsoy et al., 1993; Sur et al., 1992); thus, basin dynamics are essential not only for the basin itself but for the whole Mediterranean Sea and even the Atlantic Ocean.

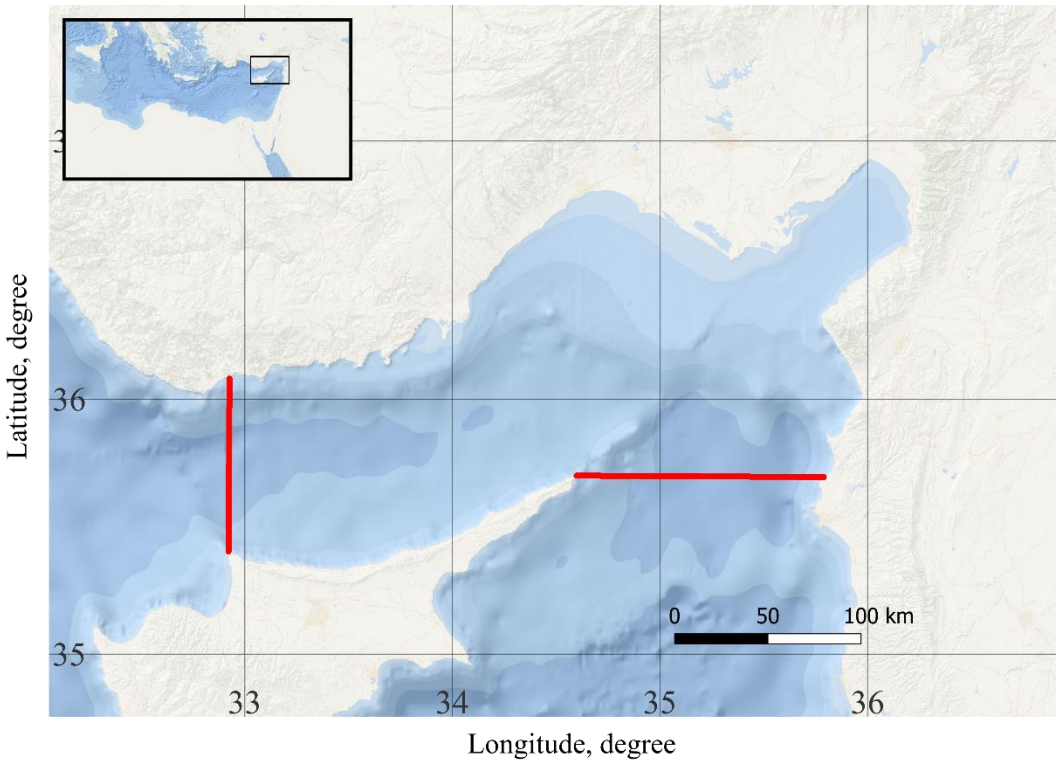

Figure 2.1 Study Area - Red lines on the map represents the boundaries set to designate borders for the models

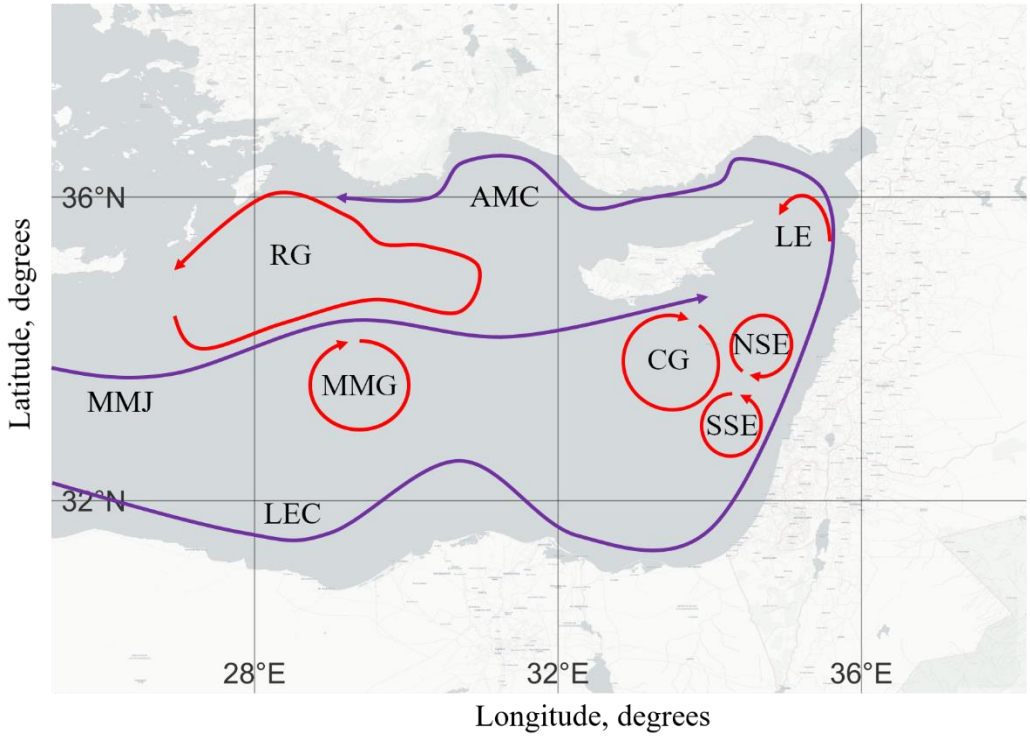

Figure 2.2. Major currents (purple), eddies and gyres (red). AMC: Asia Minor Current, CG: Cyprus Gyre, LE: Latakia Eddy, LEC: Libyo-Egyptian Current, MMG: Mersa-Matruh Gyre, MMJ: Mid-Mediterranean Jet, NSE: North Shikmona Eddy, RG: Rhodes Gyre, SSE: South Shikmona Eddy (Modified from Menna et al., (2021) and Robinson et al., (1991))

The Cilician Basin has an oligotrophic nature due to the rapid anti-estuarine circulation, with low nutrient concentrations and primary production (Tugrul et al., 2019). Yılmaz & Tugrul (1998) showed that offshore surface waters have an average NO_3^- and PO_4^{3-} concentrations of 0.2 μM and <0.02 μM in late-summer, 0.8 μM and 0.03 μM in early-spring time respectively, during 1991-1994, in an anticyclonic region of the basin. They reported that the NO_3^- and PO_4^{3-} concentrations were nearly stable along the entire deep water column converging to an average value of 5.5 μM and 0.2 μM, respectively. Furthermore, the resulting NO_3^- to PO_4^{3-} ratios ranged between 5-20 and went up to 120 at the top of the nutricline and practically stable in the deep water with an average value of 28 (Yılmaz & Tugrul, 1998). Overall, the large ratios with respect to the Redfield ratio pointed out that the basin is phosphorus limited, as in the case of the entire Eastern Mediterranean Sea (Krom et al., 2004; Redfield, 1963; Tugrul et al., 2019). More recent studies have found similar ranges and patterns for DIN and PO_4^{3-} in the offshore waters of the Cilician Basin, however, much higher concentrations found in the coastal waters of İskenderun Bay and Mersin Bay revealed elevated primary production levels probably caused by river, wastewater discharges and other catchment based sources (Akçay, 2015; Polat, 2007; Yucel, 2018). Riverine and atmoshpheric nutrient inputs previously reported as 1.2×10^9 mol km^{-2} yr^{-1} and 10×10^9 mol km^{-2} yr^{-1} for DIN, 0.04×10^9 mol km^{-2} yr^{-1}, 0.06×10^9 mol km^{-2} yr^{-1} for PO_4^{3-} and 1.54×10^9 mol km^{-2} yr^{-1}, 0.16×10^9 mol km^{-2} yr^{-1} for dissolved silicate (Si_{dis}), respectively (Koçak et al., 2010).

The catchment is largely dominated by karstic geology with neritic limestone from Miocene (General Directorate of Mineral Research and Exploration, Türkiye, 2002) (Figure 2.3). The area between the Taurus Mountains and the sea is mostly occupied with undifferentiated Quaternary sediments in Adana (General Directorate of Mineral Research and Exploration, Türkiye, 2002). Although peridotite is frequently

observed around Samandağ, limestones are once again evident to the east of İskenderun Bay (General Directorate of Mineral Research and Exploration, Türkiye, 2002). Five largest rivers in the catchment are, Ceyhan, Seyhan, Asi (Oronthes), Göksu, and Anamur (Dragon) rivers according long term annual mean discharge rates and their total disccharge accounts for more than 95% of total riverine discharge into the basin (General Directorate of State Hydraulic Works, Türkiye, 2018).

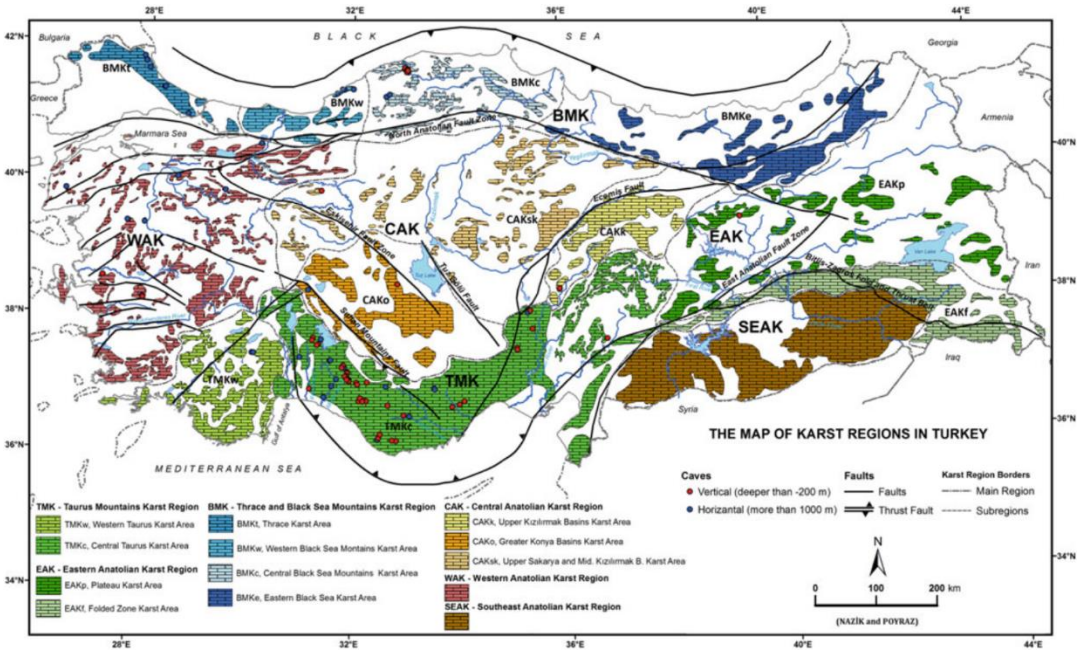

Figure 2.3. Karst map of Turkey (Nazik et al., 2019)

2. 2. Sampling and Analysis Strategy

In 2022, two basin-wide cruises (April & September), as well as two catchment surveys (March & September), were performed to acquire Radium and nutrient samples for seawater, rivers, and groundwater. In addition, total suspended sediment samples were collected from the rivers.

Sea water samples were collected for Radium and nutrient analyzes during the research cruises in April and September 2022 (hereafter wet season and dry season, respectively) and during field expeditions that were carried out in March and

September 2022 for river and groundwater samples., 250, 120, and 60 liter polyethylene tanks were utilized to collect, transport, and filter the samples. All the tanks were immersed in seawater, washed and air-dried prior to the sampling in order to get rid of any particles that may have absorbed Ra.

Mn-fibers supplied by Scientific Computer Instruments were used for seawater samples in the dry season, while the fibers used in the wet season had been cooked at METU-IMS. Fibers were impragnated by preparing a solution of 4 L of water and 325 grams of $KMnO_4$ at 65-70 C water temperature. 250 grams of acrylic fibers added to the solution and cooked for 15-20 minutes at 70-80 °C on a hot plate (Dulaiova & Burnett, 2004; Moore, 1976). Manganese-impragneted acrylic fibers were washed with Radium-free water until the water is clear. Both fibers were used for certain replicate samples to ensure equal efficiency of all the fibers employed.

Suspended solids carried by rivers may be a significant source of Radium. Therefore, total suspended solid (TSS) measurements were carried out for Göksu, Berdan, Seyhan, and Ceyhan rivers in the March expedition, and for Göksu, Berdan, Seyhan, Ceyhan, Anamur, Asi, Deliçay (Mersin), and Lamas rivers in the September cruise by filtering additional 1 L sample through previously dry-weighed glass microfiber filters (grade: GF/C). The filters were dried in a drying oven and then weighed. The differences between pre-weigh and post-weigh was assigned as TSS concentrations.

2. 2. 1. Cilician Basin Expeditions

Sea expeditions were carried out by Research Vessel Bilim 2, which operates within the body of the Middle East Technical University Institute of Marine Sciences. 80, and 118 ^{228}Ra samples from 21 and 38 stations were taken in the wet (April 13-16, 2022) and dry (August 31 – September 4, 2022) season cruises, respectively (Figure 2.4 & Figure 2.5), at different depths determined by analyzing temperature, salinity, and density profiles simultaneously in the vessel to see variability between water masses at the coordinates and depths specified in table provided in **Appendix A**. In

addition, nutrients samples were taken along with each different Ra samples, excluding the replicates. The surface waters (3m depth) were collected with the help of the pump on the ship, and the deeper ones with the help of 12 Niskin bottles (12L each) on the Rosette sampler equipped with a Seabird 911 CTD (conductivity-temperature-depth) device. Pressure, conductivity, temperature and dissolved oxygen were measured by using Seabird 911. Water sample of 120 liters for the first 600 m depth, and 250 liters for deep layers were taken. The volumes were decided considering the potential detection limit of the analyzing instrument for ^{228}Ra, previous findings in the Mediterranean Sea that suggested much lower activities in the deep water (Rodellas et al., 2015), and logistics. Nutrient samples were taken into plastic bottles of 250 ml, and kept in the freezer immediately after collection to stop the biological activity.

The number of sampling stations were increased in the dry season cruise to have more precise estimations of ^{228}Ra inventory in the İskenderun Bay (Figure 2.6).

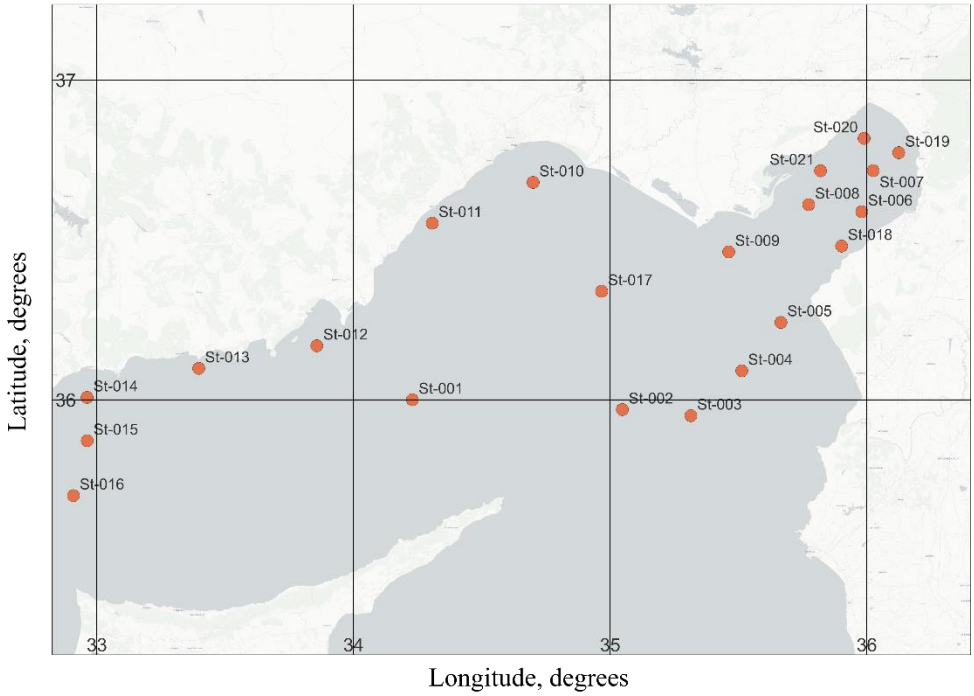

Figure 2.4. Wet season cruise sampling stations

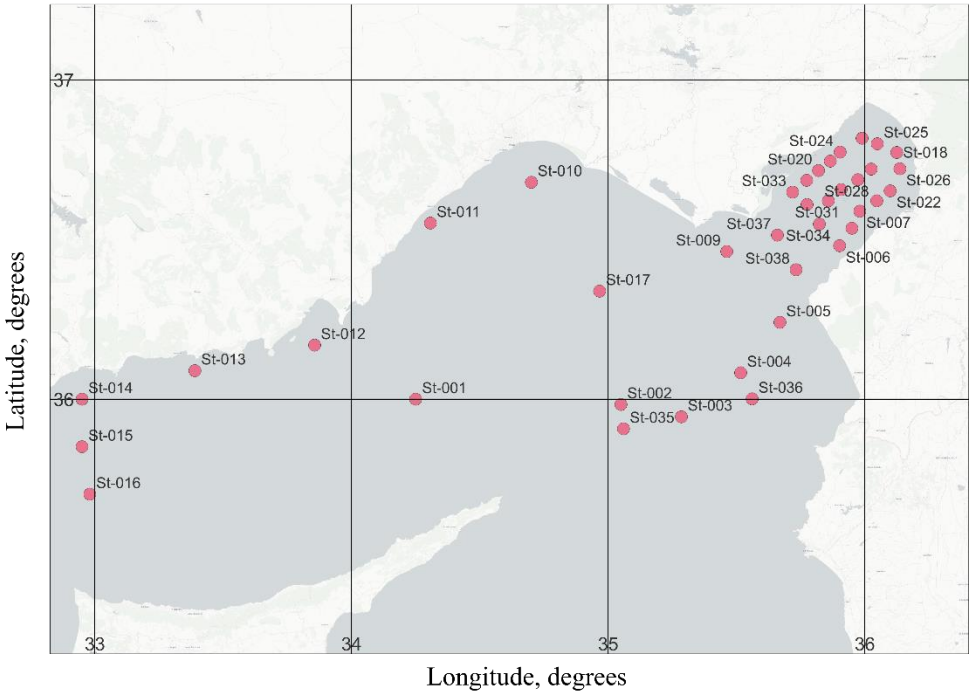

Figure 2.5 Dry season cruise sampling stations

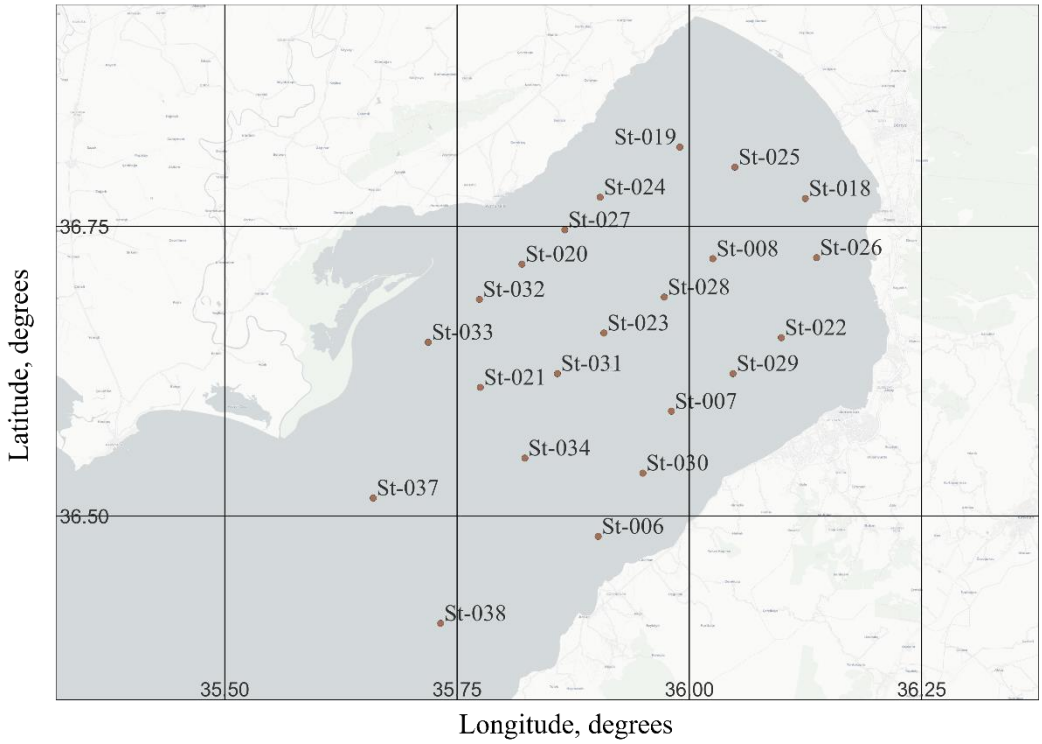

Figure 2.6. Dry season cruise İskenderun Bay sampling stations

The water was collected in labelled tanks and then filtered through previously fluffed 25 gr (dry weight) acrylic fibers impregnated with MnO_2 (Mn-fibers) (Charette et al., 2012). Raw fibers were placed to filter any particle that might stuck in the Mn-fiber, although the turbidity was low. Certain samples were passed through two serially connected cartridges to calculate the Ra absorption efficiency of the fibers (**Appendix B**). The filtration rate from acrylic fibers remained below 1 L/min from the beginning to the end (Moore & Reid, 1973). After this process, the fibers were labeled and stored in plastic zip-lock bags.

2. 2. 2. River and Groundwater Samplings

A total of nine rivers were sampled in addition to nine groundwater wells and a karstic uderground lake (Figure 2.7). The Ra samples taken in the catchment sampling surveys are listed in the table given in the **Appendix B**, along with the locations, and depths. While Radium samples were taken as 60 liters, nutrient samples were taken as 250 ml, as same with basin-scale cruises. The samples in rivers were collected with a portable pump, and with the help of pumps already existing and operating in wells. Prior to the water sampling in wells, at least three times of the volume of the well was discarded. The samples were directly taken into the 120 liter transfer tank, then passed them through different 1 μm filters for each sample, labelled and stored them. The filters were kept to analyze radium diffusion rates later. The filtered waters were transferred directly to 60 liter polyethylene tanks, and acrylic fibers were filtered in these tanks. The filtration rate from acrylic fibers remained below 1 L/min, then the fibers were labeled and stored in plastic zip-lock bags. In addition, specific conductivity (SC) and temperature of each sample was measured using a WTW 3110 hand-held probe.

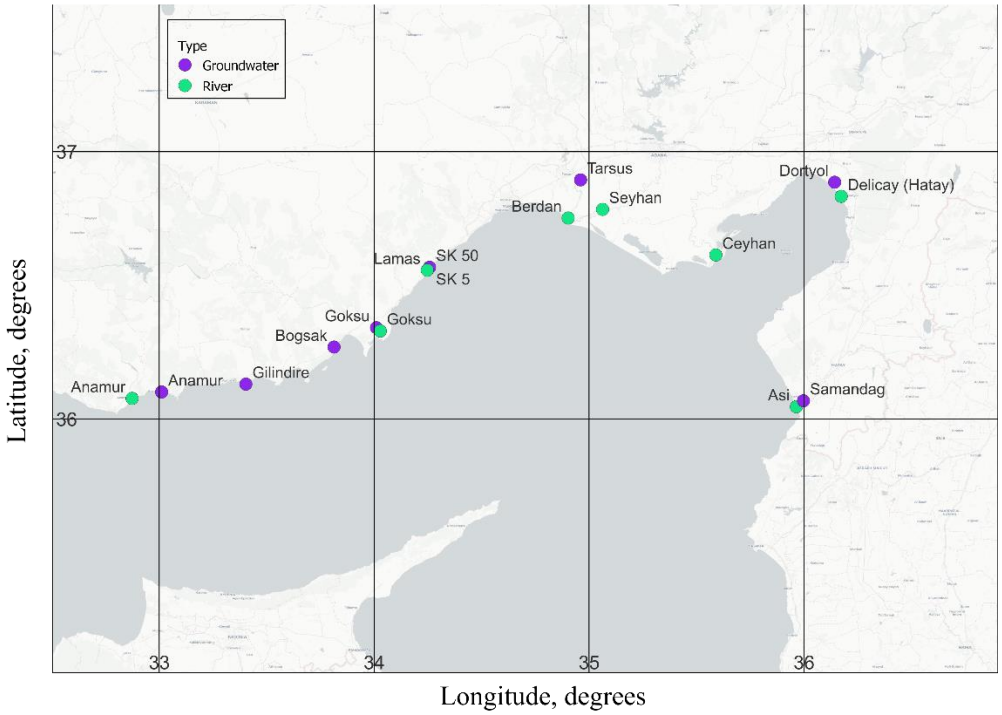

Figure 2.7. Catchment sampling stations

Annual riverine nutrient loads were calculated using weighted-average nutrient concentrations of one wet season sample and one dry season sample, according to monthly discharge rates in the most recent river fluxes reported by General Directorate of State Hydraulic Works of Türkiye (2018). Weighted averages were multiplied by long-term averages of annual fluxes and by fluxes of 2014-2015, seperately to observe the difference between long-term average assumption and the most recent fluxes. For wet and dry seasons concentrations, samples retrieved in March and September were used, respectively, if available. Otherwise, April and October concentrations were used in the calculations.

An additional survey conducted in April 2023 to measure DO levels in groundwater samples as anoxic conditions may cause Ra isotopes to escape from the Mn-fibers (Kousa et al., 2021; Vinson et al., 2013). DO concentrations were measured using YSI ProDSS handheld multiparameter meter, which is calibrated before every sampling with standard solutions and water-saturated air.

2. 2. 3. Radioisotope and Nutrient Analysis

2. 2. 3. 1. Radium Analysis by Gamma-ray Spectrometry

Radium activities were measured by gamma spectroscopy at Louisiana State University (LSU) using three Canberra well-type coaxial Germanium (Ge) detectors, two GCW3022 and one GCW353 models. ^{228}Ra activities of samples from the İskenderun Bay in the dry season cruise were measured with an ORTEC GWK model coaxial high purity Ge detector in Turkish Accelerator and Radiation Laboratory (TARLA) in order to check its usability for the thesis research as it may provide convenience for logistics. The detector used at TARLA was calibrated using 10.71 g of IAEA-RGTh-1 reference material prepared on behalf of the International Atomic Energy Agency by the Canada Centre for Mineral and Energy Technology. The detector has built-in shield on the sides and additional lead plates with a total thickness of 17.5 cm, were placed under the samples in order to create an environment similar to the well type detectors. The activities measured at TARLA were only used to calculate the ^{228}Ra inventory in the bay, and they were not used in the SGD estimations as the detector at LSU and the one at TARLA were not inter-calibrated, and using all the activities in one model might be inconsistent. In the SGD calculations, only the ^{228}Ra activities measured at LSU were considered.

The samples were sealed to achieve an equilibrium between Ra and its daughter isotopes, at least three weeks prior to the analysis. ^{226}Ra emissions were detected by the ^{214}Pb peak at 351.9 keV, the activity of ^{228}Ra was identified through the photopeak of its daughter ^{228}Ac at 911.6 keV. The analyses were carried out for 1-3 days, until the spectrum settled and had a plausible statistics. The measured ^{226}Ra activities were used solely to calculate ^{228}Ra to ^{226}Ra activity ratios as a potential tracer of water masses in the layers and of origins of Ra fluxes. Germanium detectors in the LSU were fundamentally responsible for some errors.

The surface activities were extrapolated through basin by DIVA method (Barth et al., 2014) using Ocean Data View software. Furthermore, activities measured at

TARLA for İskenderun Bay surface samples were interpolated using the Generic Mapping Tools version 6 (Wessel et al., 2019) and extrapolated using Surfer® (Golden Software, LLC) software employing Delaunay Triangulation and Krigging methods, respectively. The different methods were employed to identify potential differences and gain more insight into the 228Ra enrichment zones. The Delaunay triangulation is defined as the one with the lowest interpolation error for the isotropic function, considering a certain number of vertices (Chen & Xu, 2004). The kriging approach, which seeks to convey hypothesized patterns in irregularly spaced data, is a geostatistical gridding tool. Essentially, it is guessing the value of the function at a given place by calculating the weighted average of the known values of the function in the point's vicinity (Jassim & Altaany, 2013).

2. 2. 3. 2. Dissolved Inorganic Nutrient Analysis

The dissolved inorganic nutrients (NO_3^-, NO_2^-, NH_4^+, PO_4^{3-}, and Si) were measured by a four-channel Bran+Luebbe model Autoanalyzer using standardized colorimetric methods (Caspers, 1970; Grasshoff et al., 2007, SEAL Analytical Booklet) at the DEKOSIM laboratories at METU-IMS, which have passed the International QUASIMEME proficiency tests.

2. 3. SGD Estimations

2. 3. 1. 228-Radium Mass Balance

Radium isotopes (^{223,224,226,228}Ra) are generated by the disintegration of Thorium isotopes (^{227,228,230,232}Th) in Uranium-Thorium decay chains, and, unlike their parent Thorium, dissolves in seawater (Jenkins, 2003). The most important element influencing the exchange of Ra between solids and groundwater has been identified as the solution's ionic strength, which is mostly determined by the salinity of the groundwater (Garcia-Orellana et al., 2021, and references therein). High ionic

strength hinders the adsorption of Ra^{2+} and encourages the desorption of surface-bound Ra due to cationic exchange (Garcia-Orellana et al., 2021). Specific conductivity (SC) was used as a direct proxy of salinity of groundwater and river samples. Since Ra isotopes are conservative in seawater, decay at a constant rate and have higher concentration in groundwater, they are widely utilized as important geochemical tracers in SGD (Garcia-Orellana et al., 2021). All four isotopes have a different half-life, and therefore they correspond to different SGD pathways with different spatial and temporal scales (Taniguchi et al., 2019) (Figure 2.8 & Figure 2.9).

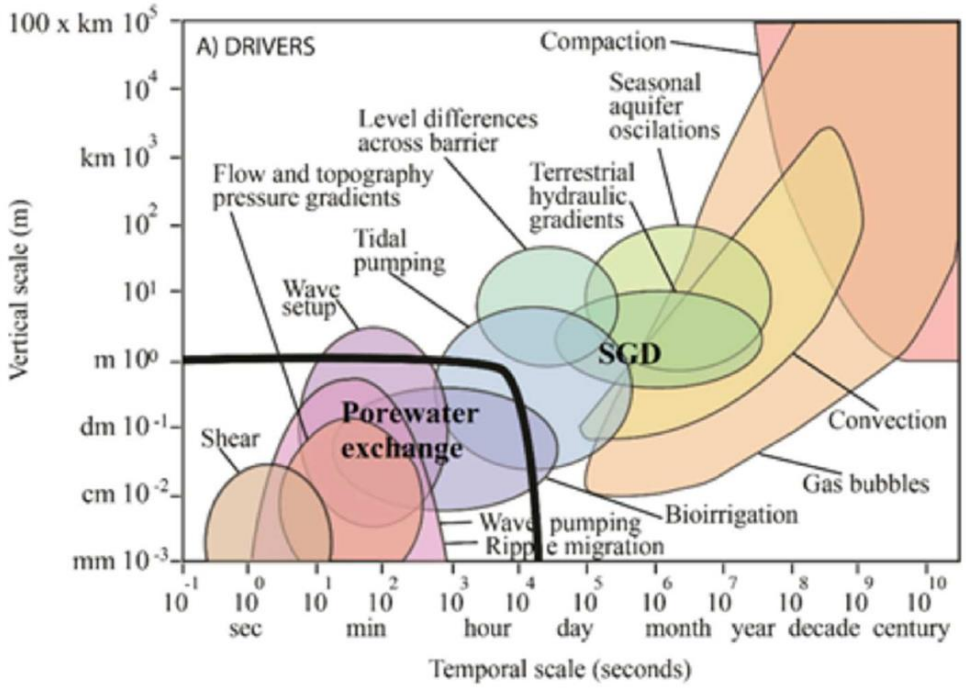

Figure 2.8. Temporal vs spatial scales for different SGD drivers (Taniguchi et al., 2019)

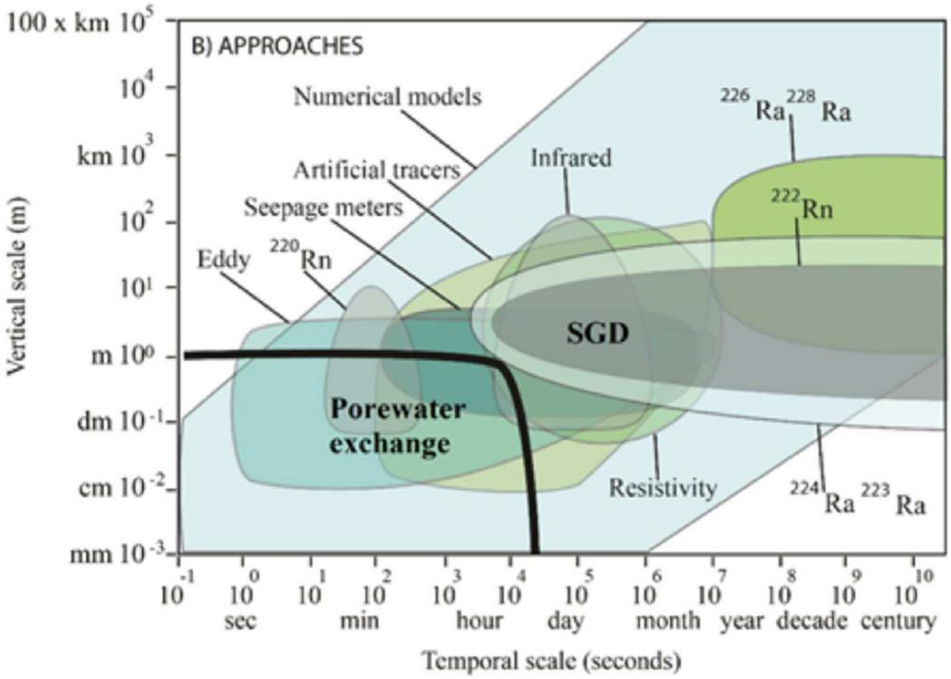

Figure 2.9. Temporal vs spatial scales for different SGD estimation approaches (Taniguchi et al., 2019)

As a tracer of SGD, ^{228}Ra isotope (half-life: ~5.75 years) was utilized, which is the suitable isotope considering its spatiotemporal scales and enables to investigate discharges driven by terresterial hydraulic head differences and seasonal water exchange in the aquifers, as the expected residence time of the basin is in the order of months to years. A mass balance approach was used assuming all the inputs are equal to outputs (Moore, 1996; Moore et al., 2008). The basin was divided into three water masses, namely, Surface Layer (SL) (0-150 m), Intermediate Layer (IL) (150-600 m), and Deep Layer (DL) (>600 m) according to the previous studies in the Mediterranean Sea (Rodellas et al., 2015; Sanchez-Cabeza et al., 2002). A box model was established for the upper 600 meters, the upper layer (UL), as the primary ^{228}Ra inputs take place in this layer, and ^{228}Ra influx from deep sediment (>600 m) was neglected (Moore et al., 2008; Rodellas et al., 2015). ^{228}Ra inputs were defined as atmospheric deposition, river fluxes (including desorption from suspended sediments), sediment diffusion, inflow from the southern boundary (Figure 2.10), and advection from the deep water layer, where the only outputs were specified as

radioactive decay, outflow from the western boundary, and vertical advection. Assuming steady-state conditions, the mass balance equation gives SGD input as the residual (Equation 1).

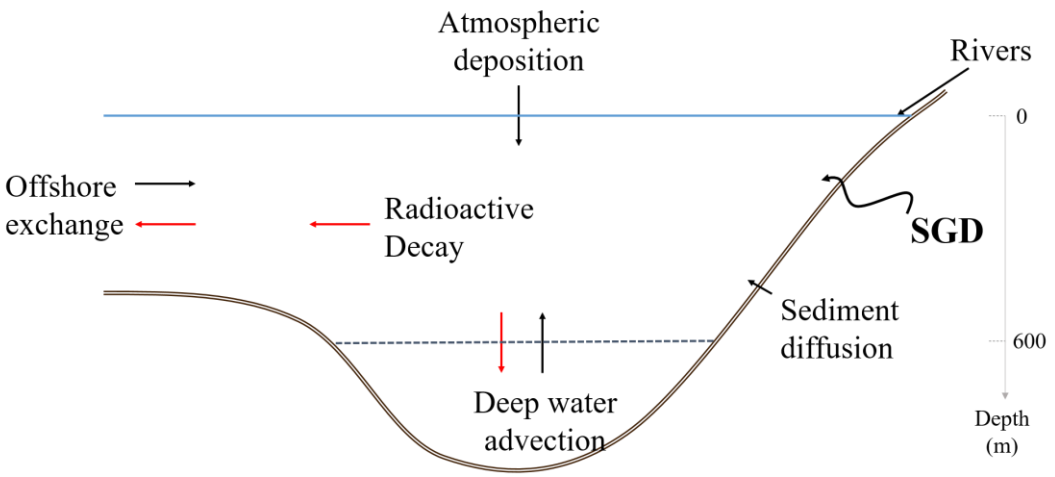

Figure 2.10. Schematic representation of the box model. The water surface is delimited by the blue solid line and dashed black line is the lower limit of the upper layer (UL), and the area below the dashed black line is the Deep Layer (DL). Black arrows indicate sources and red arrows indicate losses in the ^{228}Ra inventory.

$$F_{sgd} + F_{sed} + F_{riv} + F_{atm} + F_{adv_{in}} + F_{ex_{in}} = F_{dec} + + F_{adv_{out}} + F_{ex_{out}} \quad [1]$$

where, F_{sgd} (dpm/yr) is the ^{228}Ra input from SGD, F_{sed} (dpm/yr) is ^{228}Ra diffusion from sediment, F_{riv} (dpm/yr) is ^{228}Ra supplied by river fluxes, and F_{atm} (dpm/yr) is the atmospheric ^{228}Ra deposition. $F_{adv_{in}}$ (dpm/yr) is verticle advection input and $F_{ex_{in}}$ (dpm/yr) is offshore water exchange input, where $F_{adv_{out}}$ (dpm/yr), $F_{ex_{out}}$ (dpm/yr), and F_{dec} (dpm/yr) represent loss terms for vertical advection, offshore water exchange, and radioactive decay, respectively.

Vertical exchange term was estimated by establishing another ^{228}Ra mass balance equation for DL (Equation 2). In addition to the abovementioned neglected sediment input (F_{sed}), offshore water exchange ($F_{ex_{in}}$, $F_{ex_{out}}$) was also neglected as the residence time of EMDW (150 years) (Powley et al., 2016) is much larger than the half-life of ^{228}Ra (~5.25 years).

$$F_{adv_{out}} = F_{adv_{in}} + F_{dec} \quad [2],$$

Thus, the mass balance equation [2] can be arranged as Equation 3:

$$Q_{adv}\, x\, A_{UL_{ex}} = Q_{adv}\, x\, A_{DL} + V_{DL}\, x\, A_{DL} x\, \lambda \quad [3],$$

$$Q_{adv} = \frac{A_{DL} \times V_{DL} \times \lambda}{A_{UL_{ex}} - A_{DL}} \quad [4],$$

where Q_{adv} (km³/yr) is the exchange flux between DL and UL. A_{DL} (dpm/km³) and $A_{UL_{ex}}$ (dpm/km³) represent the activities per unit volume exchanged between the DL and UL, respectively. V_{DL} (km³) is the water volume of DL, and λ is the radioactive decay constant. Then, $F_{adv_{in}}$ (dpm/yr) and $F_{adv_{out}}$ (dpm/yr) can be calculated as in the Equation 5 and 6:

$$F_{adv_{in}} = A_{DL}\, x\, Q_{adv} \quad [5],$$

$$F_{adv_{out}} = A_{UL_{ex}}\, x\, Q_{adv} \quad [6].$$

Finally, $F_{ex_{in}}$ (dpm/yr) and $F_{ex_{out}}$ (dpm/yr) were calculated as the product of the activities of inflow from the southern boundary (A_{in}, dpm/km³) and outflow from the western boundary (A_{out}, dpm/km³), capturing ^{228}Ra enrichment in the basin, and the offshore water exchange rate, Q_{ex} (km³/yr):

$$F_{ex_{in}} = A_{in} \times Q_{ex} \quad [7],$$

$$F_{ex_{out}} = A_{out}\, x\, Q_{ex} \quad [8].$$

Q_{ex} (km³/yr) was estimated by dividing the volume of the box, V (km³), by residence time, τ (1/yr), the time that a water parcel resides within a water body before leaving through one of the boundaries. The residence time was computed by a Lagrangian particle tracking model (see **2. 4. 2.**).

Sediment diffusion rates were calculated by using the rates reported by Moore et al., (2008) according to the grain sizes and slopes. The grain size distribution given for the Northeastern Mediterranean Basin (Yemenicioglu & Tunc, 2013) were

extrapolated. Areas were calculated by digitizing the bathymetry data obtained from General Bathymetric Chart of the Oceans (GEBCO) Web Map Service (https://download.gebco.net/), using QGIS (version 3.26.0) software (QGIS Development Team, 2022).

River-borne ^{228}Ra was calculated multiplying total river discharge by weighted-average activity in the rivers. Further, desorption from suspended particles in the river water was estimated as a product of total suspended particles and the diffusion rate of 0.5 ± 0.4 disintegration per minute (dpm) per gram as it covers a major portion for the estimates in the literature (Moore & Shaw, 2008; Ollivier et al., 2008; Rodellas et al., 2015). Total ^{228}Ra input from river is represented by F_{riv}.

Ediger (2020) reported an annual atmospheric dust deposition of 20.25 $g \cdot m^{-2} \cdot y^{-1}$ in the Mersin Bay and İskenderun Bay. The estimation were extrapolated to the whole basin to have a conservative approach on SGD-derived ^{228}Ra. ^{228}Ra desorption rate was set to 2 $dpm.gr^{-1}$ considering that it is close to the highest documented value in the literature (Moore et al., 2008; Moore & Shaw, 2008; Rodellas et al., 2015). The total annual airborne dust deposition and the desorption rate was represented in the F_{atm}.

Decay term was calculated by multiplying the decay constant of ^{228}Ra, λ, ~0.12 y^{-1}, by the total ^{228}Ra inventory of the box defined. The inventory was estimated by defining the mean ^{228}Ra activities and volume of each layer using GEBCO bathymetry data and QGIS.

The residual SGD ^{228}Ra flux, F_{sgd} (dpm/yr), was divided by a range of ^{228}Ra activities (dpm/km^3) found in groundwater samples, end-member activities, in order to obtain the SGD rates. For end-members, the activities in the groundwater samples along the Cilician Basin coasts were used. In addition, the SGD rates were re-calculated using the first and third quartiles of end-member activities reported for the Mediterranean Sea as no saline groundwater sample was obtained in the catchment surveys (see Chapter 3 and Chapter 4), and it incorporates a large portion of the data

and eliminates abnormal concentrations. Therefore, using the quartiles as the range of end-member activity is suggested to be the best approach for characterizing ^{228}Ra concentration (Rodellas et al., 2015, and references therein).

2. 3. 2. SGD Associated Nutrient Fluxes

PO_4^{3-}, DIN, and Si fluxes through SGD were estimated by multiplying nutrient end-member concentrations with above-mentioned SGD rates. The nutrient fluxes were conservatively calculated only from the fresh portion of the submarine groundwater discharge. This approach assumes a net nutrient flux to the basin and does not account for potential biogeochemical changes in the aquifers or subterranean estuaries (Rodellas et al., 2015). Nutrient end-member concentration range was assigned as the first and third quartiles of measured concentrations in the groundwater samples. The percentage contribution range reported by Bayari et al., (2011) for a neighboring area with very similar geological and meteorological conditions located on the coast of Antalya, between Kalkan and Kumluca, in Turkey's Mediterranean coast, was used to estimate fresh SGD rates. Pore-water exchange was neglected as the ^{228}Ra, which has approximately 5.75 years of half-life, does not capture the necessary centimeter scales (Taniguchi et al., 2019). Therefore, our estimations only included long-scale recirculation processes as saline SGD (Rodellas et al., 2015).

2. 4. Residence Time

Residence time studies that are required to estimate offshore seawater exchange rates have been conducted using E.U. Copernicus Marine Service Information and a Lagrangian particle tracking model, OceanParcels (Delandmeter & van Sebille, 2019; Kehl et al., 2023). Furthermore, one ARGO float (World Meteorological Organization #6901876), which is an autonomous robotic instrument used for oceanographic research and data collection that drifts with the ocean currents and

gets profiles of temperature, salinity, pressure, and desired biogeochemical properties (Jayne et al., 2017), was investigated to observe their residence times in the basin and compare them with the model results.

2. 4. 1. Hydrodynamic Model Product

Copernicus Marine Environment Monitoring Service (CMEMS) has hydrodynamic analysis and forecasting products. Copernicus Marine Mediterranean Sea MultiYear Physical Product "MEDSEA_MULTIYEAR_PHY_006_004" of CMEMS used to obtain the daily velocity fields from 2016 to 2020, which has a horizontal grid resolution of about 4 km and one hundred and forty-one irregularly spaced depth levels (E.U. Copernicus Marine Service Information (CMEMS), accessed in 2022).

Annual fluxes were calculated by summing daily net fluxes through the boundary sections for a given year (Figure 2.11). The water volumes in the regions were found using the QGIS (version 3.26.0) software (QGIS Development Team, 2022) and the bathymetry data from the GEBCO. The water residence time for the entire water column was determined by dividing the calculated flow rates. The process was repeated for the years from 2016 to 2020, separately. Five consecutive years were selected in order to investigate inter-annual variations in the residence time.

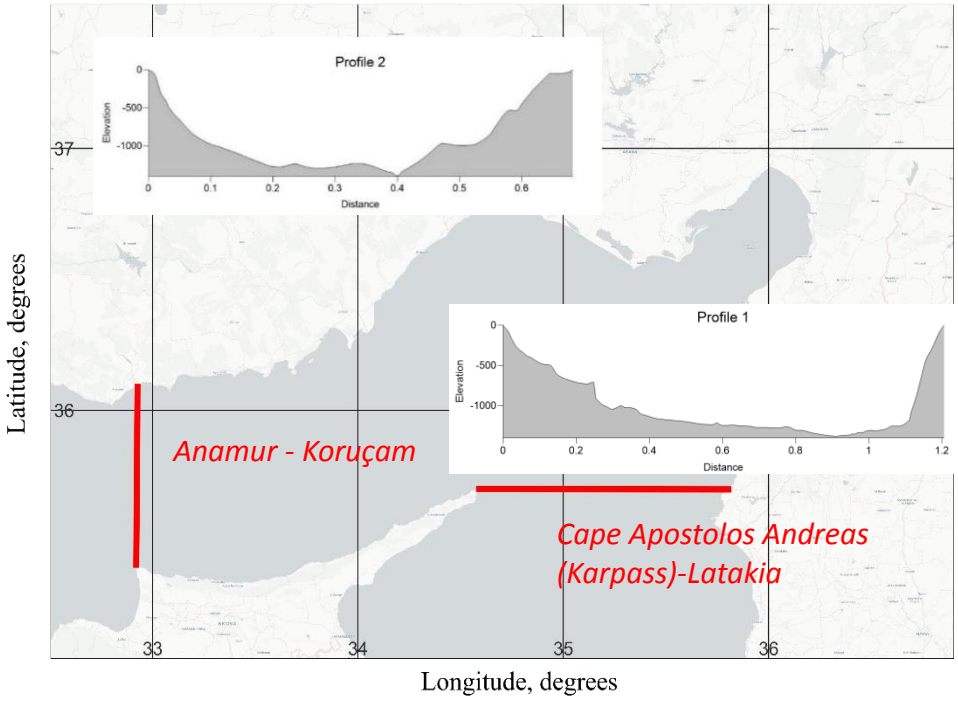

Figure 2.11. Boundaries and cross-sections used for Hydrodynamic Model Product method

2. 4. 2. Particle Tracking Model

OceanParcels enables the creation of Lagrangian particle tracking simulations using hydrodynamic model outputs and can be used to track particles (Delandmeter & van Sebille, 2019; Kehl et al., 2023). The necessary hydrodynamic data input was obtained from above-mentioned CMEMS product for the four years through 2019-2022, in order to carry out particles in a flow field. OceanParcels works only with two-dimensional flow data at the depth at which the particles are released, rather than following the particles according to three-dimensional circulation. The model inherently allows us to calculate residence time taking the return flow into account, contrary to the analytical method using hydrodynamic model product (**2. 4. 1**) which integrates daily net flows regardless of whether the water is going in and out of the same boundary, in other words, whether it returns or not.

For the Cilician Basin, a thousand particles were released in the water column with ten meter intervals until 600 meters depth at the southern boundary (Figure 2.12). Separate simulations were carried out for each depth. For the water residence time calculations, the departure times of the particles from the basin were determined. The residence time distributions of the particles were analyzed and the median departure times of the particles were used in the residence time estimates. Stuck particles – if any occurs – were removed from median calculations to avoid any geometry bias. The model script is given in the repository, *https://github.com/kuyumcu-b/thesis* under the MIT License. Further, the results interpolated with the DIVA tool of Ocean Data View software. The average residence time is considered as the offshore exchange rate in the ^{228}Ra mass-balance model.

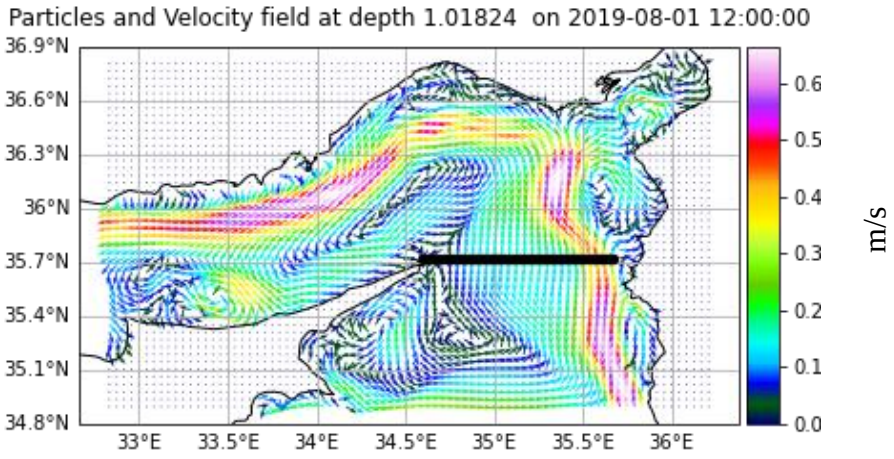

Figure 2.12. Particle release points and an example of flow field. Solid black lines shows particle release locations.

2. 5. Data and Statistical Analysis

Data and statistical analysis and visualization were conducted by RStudio version 2023.3.1.446 (Posit team, 2023), utilizing the programming language R (R Core Team, 2022) and the packages corrplot (Wei & Simko, 2021) for the correlation graph, effectsize (Ben-Shachar et al., 2020) for calculating effect size, ggmagnify

(Hugh-Jones, 2023), ggpubr (Kassambara, 2023a), RColorBrewer (Neuwirth, 2022), and scales (Wickham & Seidel, 2022) for visualization, PerformanceAnalytics (Peterson & Carl, 2020) and rstatix (Kassambara, 2023b) for statistical analysis, , readxl (Wickham & Bryan, 2023) and writexl (Ooms, 2023) to read and write data on excel sheets, and tidyverse (Wickham et al., 2019) for data wrangling.

Shapiro-Wilk test was used to identify normality in the dataset, by assuming normal distribution for p-value greater than 0.05. Correlation tests were carried out utilizing Pearson's product moment method. Analysis of variance (ANOVA) and Kruskal-Wallis tests were utilized to investigate differences between the means of different groups and effects sizes were calculeted by eta square approach.

CHAPTER 3

RESULTS

3. 1. Physico-chemical Results

3. 1. 1. Catchment Surveys

In addition to the in-situ recorded SC and temperature data, eighty-seven groundwater samples and eighteen riverine samples were analyzed for nutrient concentrations. Table 1 and Table 2 shows the SC values of the groundwater samples, and river samples, respectively, that had ^{228}Ra and ^{226}Ra activities measured. Pearson correlation test showed no significant correlation between SC values and radium activities in groundwater ($p = 0.70$ for ^{228}Ra, $p = 0.83$ for ^{226}Ra) and river samples ($p = 0.59$ for ^{228}Ra, $p = 0.70$ for ^{226}Ra). Note that, the highest SC in groundwater samples was 3460 µS/cm (Samandağ Well) which corresponded to a salinity value of approximately 2 parts per thousand (ppt). Therefore, there were no saline end-member of groundwater in our sample set. Also, the highest SC in river samples was 988 µS/cm.

Table 1. SC and Temperature values of groundwater samples

Sample ID	Station	Date	Campaign	SC (µS/cm)	Temperature (°C)
10	IMS SK5 (in-series) 1	10/19/2021	Pilot	670	22.2
13	IMS SK50 (in-series) 1	10/19/2021	Pilot	820	20.6
34	IMS SK50 – US fiber	12/15/2021	Pilot	852	19.5
35	IMS SK50 – TR fiber	12/15/2021	Pilot	852	19.5
39	Anamur Well	3/2/2022	Wet Season Catchment	731	17.5
40	Gilindire Cave	3/2/2022	Wet Season Catchment	2810	20.2
41	Boğsak Well	3/2/2022	Wet Season Catchment	2500	13.3
42	Göksu Well	3/2/2022	Wet Season Catchment	908	20.1
45	Tarsus Well	3/3/2022	Wet Season Catchment	2230	19.5
48	Dörtyol Well	3/4/2022	Wet Season Catchment	1122	20.1
51	Samandağ Well	3/4/2022	Wet Season Catchment	3460	17.9

Table 2. Specific conductivity (SC) values of river samples

Sample ID	Station	Date	Campaign	SC (µS/cm)
16	Lamas River (in-series) 1	10/20/2021	Pilot	415
31	Asi River – US fiber	12/13/2021	Pilot	897
32	Asi River – TR fiber	12/13/2021	Pilot	897
36	Lamas River – US fiber	12/15/2021	Pilot	481
37	Lamas River – TR fiber	12/15/2021	Pilot	481
38	Anamur River	3/2/2022	Wet Season Catchment	480
43	Göksu River	3/2/2022	Wet Season Catchment	428
44	Berdan River	3/3/2022	Wet Season Catchment	804
46	Seyhan River	3/3/2022	Wet Season Catchment	500
47	Ceyhan River	3/4/2022	Wet Season Catchment	705
49	Deliçay (Hatay) River	3/4/2022	Wet Season Catchment	307
50	Asi River	3/4/2022	Wet Season Catchment	988
52	Lamas River	3/10/2022	Wet Season Catchment	364

The April 2023 sampling survey revealed that none of the groundwater samples were anoxic (Table 3). Despite the fact that the DO concentrations in the Göksu-1 and Samandağ samples were low—between 1-2 mg/L—, nitrate concentrations (Table 8) combined with the DO prevented Ra from escaping off Mn-fibers (Vinson et al., 2013). According to Vinson et al. (2013), the existence of dissolved oxygen or nitrate creates thermodynamically stable circumstances for solid-phase metal oxides, facilitating the removal of Ra from groundwater.

Table 3. DO concentrations of groundwater samples, April 2023

Station	**DO, mg/L**	**DO, %**
Anamur	7.23	78.2
Gilindire	8.05	92.3
Boğsak	5.01	53.2
Göksu-2	4.32	48.0
Göksu-1	1.23	13.7
Tarsus	5.99	67.2
Dörtyol	7.75	85.3
Samandağ	1.81	19.9
SK50	3.92	43.4

3. 1. 2. Basin-scale Research Cruises

In the wet season expedition, a total of 75 samples of seawater were gathered from 21 distinct sampling locations, while the dry season expedition yielded 112 samples from 38 different stations. CTD profiles were acquired for each station, except in cases where solely 3-meter depth samples were procured. The Figure 3.1 presents salinity and temperature profiles of the stations. The sampling depths of Ra in addition to the 3 m, 600 m depths and 30 m from the seabed were determined by analyzing the profiles. For example, in St-001 (Figure 3.2); 40 m was decided to sample the low-end of the mixed surface layer, where 100 m was sampled to get the below of the layer and 250 m was sampled for the salinity maxima.

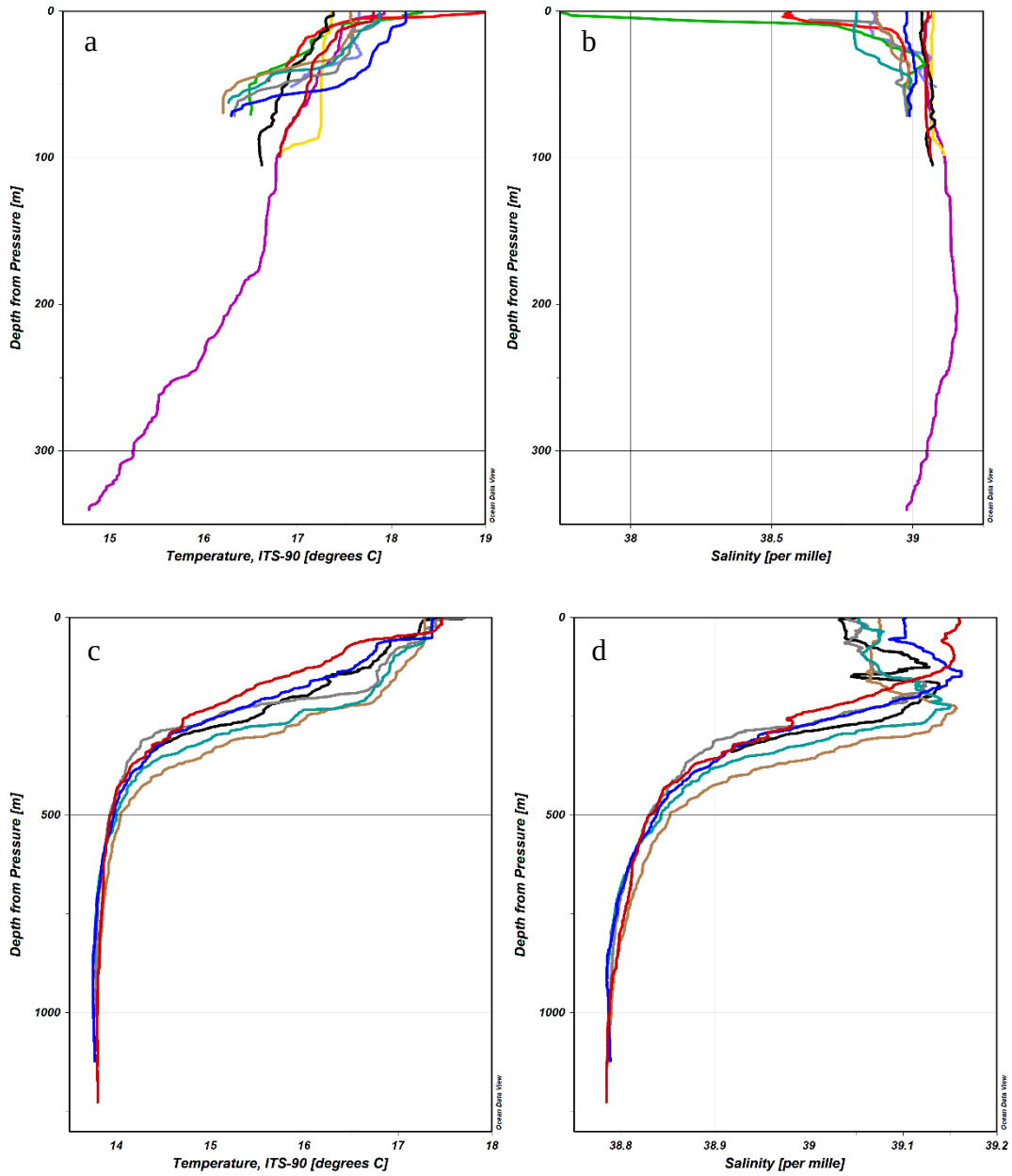

Figure 3.1. Temperature and salinity profiles in wet season for coastal (a, b) and offshore (c, d) stations.

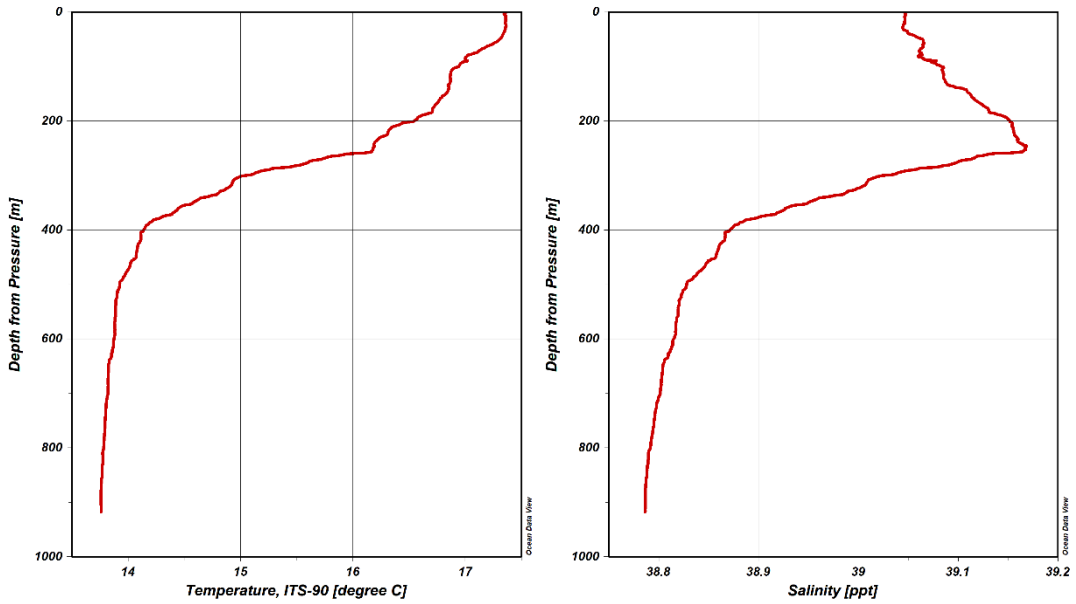

Figure 3.2. Temperature and salinity profiles of St-001 in the wet season

The first 30 meters of the water column was well mixed in the wet season cruise with almost constant temperature (17.36 ºC) and salinity (39.05) in the central station (St-001) (Figure 3.2). Then, the salinity gradually increased to its maximum, 39.17, while the temperature decreased to ~16.19 ºC at 250 meters depth. This salinity maximum area usually is the sign of LIW, which is found at between approximately 130 m and 290 m depths. After the salinity maxima, there was a sharp halocline through ~400 m, where the salinity dropped to 38.87. Salinity dropped further with depth afterwards, and had the minimum value of 38.79. Furthermore, dissolved oxygen (DO) concentrations reached their maximum between 30 m and 170 m depths with 196.25 µM.

Overall, the wet season surface salinities changed between 37.75 and 39.16 with an average value of 38.97. The variation was largely caused by the distance from river mouths, e.g. St-009 and St-011 had the minimum surface salinities. Interestingly, highest values were found in the western boundary stations (St-014, St-015, and St-016). Moreover, the surface DO values were generally higher in the coastal stations located in the vicinity of river discharge points, and St-011 (which is only 2.9 nautical miles away from the mouth of Lamas River) had the highest value of 217.91 µM.

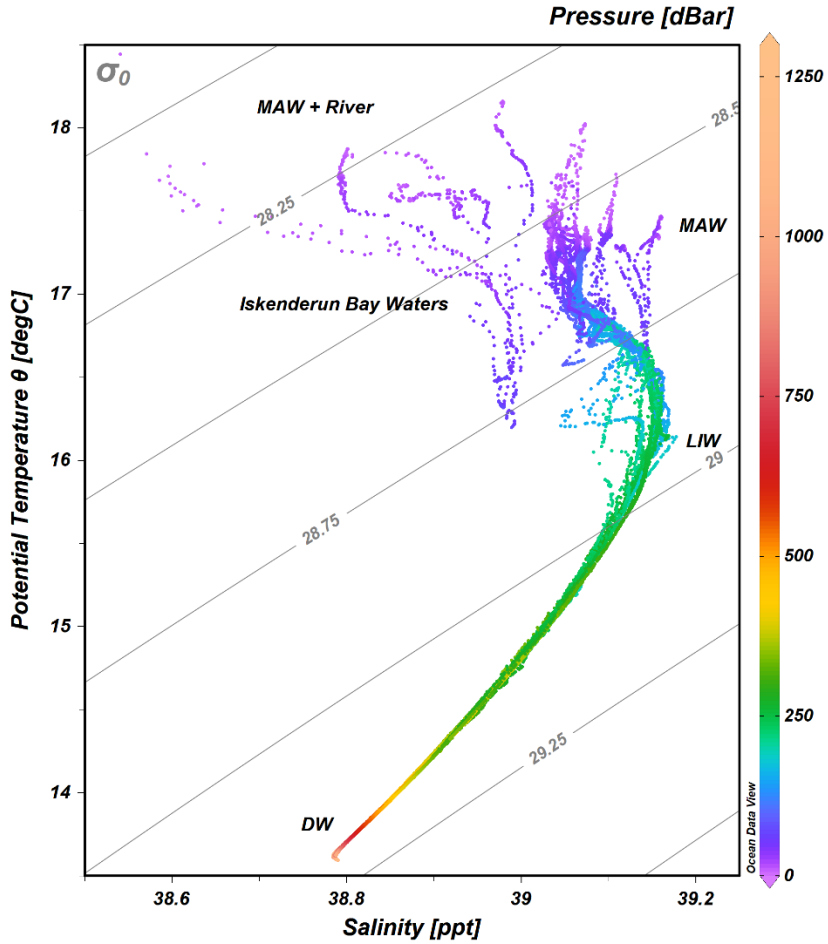

Figure 3.3. T-S (temperature-salinity) diagram showing the water bodies observed in wet season survey. Each dot shows the profile data on the stations, and the color palette shows the pressure/depth. Gray lines are isopycnals.

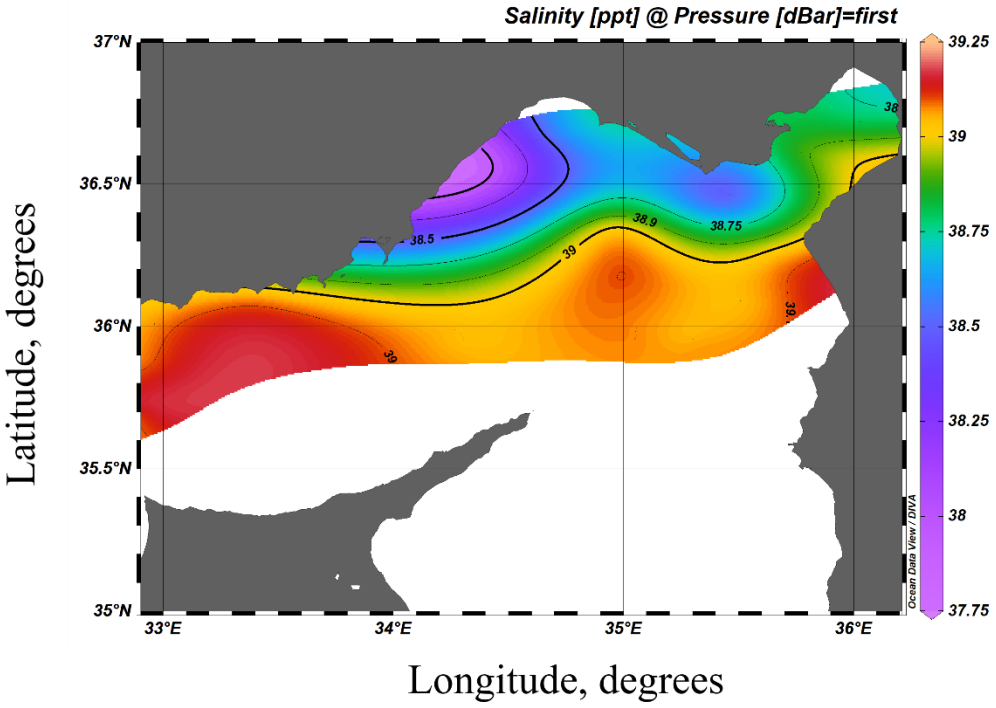

Figure 3.4. April 2022 Sea surface salinity map

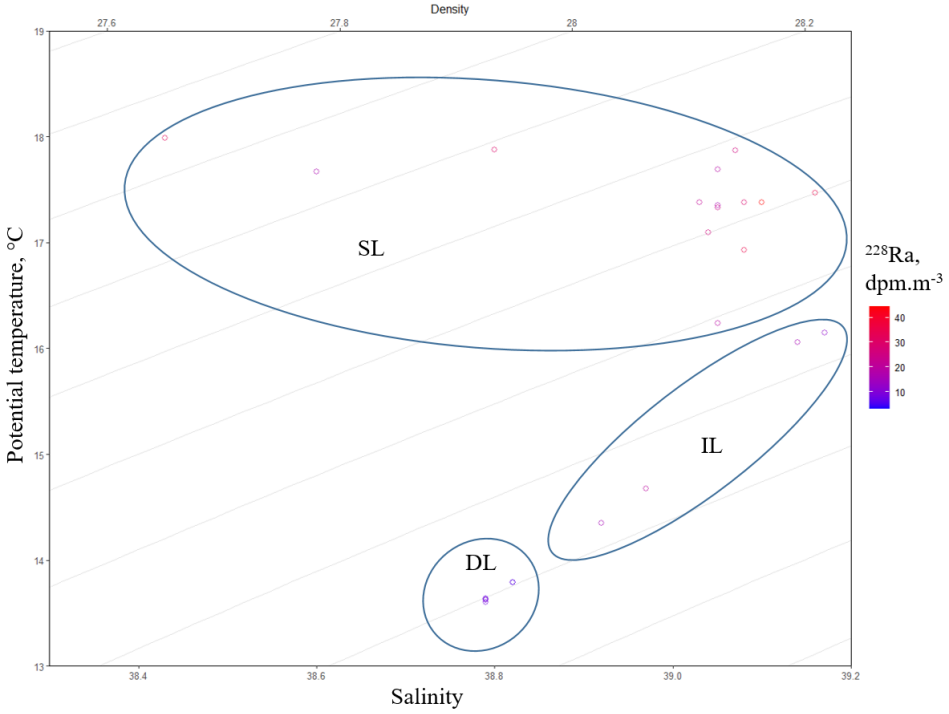

Figure 3.5. April, 2022 T-S Diagram in relation to ^{228}Ra activities. SL:Surface layer (0-150 m), IL: Intermediate layer (150-600 m), DL: Deep layer (>600 m)

In general, the salinity peaked at the surface of the offshore stations in the dry season, with a range between 39.4-39.6. The first 25 meters were strongly stratified and homogeneous with high temperature (~28.96 ºC), salinity (~39.60), and DO concentrations (191.00 µM). Shallow coastal stations except the ones located river mouths, also had the same well-mixed saline surface layer with salinity between 39.4 and 39.5. Below, a sharp thermocline was located until 50 m depth and temperature decreased to 16.73 ºC at 100 m. The halocline was even sharper and salinity decreased to 39.02 at ~37 m depth almost overlapping with the maximum DO concentration of 257.67 µM (115.18% saturation). Then, salinity rose again to 39.12 at almost 150 m depth, where the center of LIW appeared. Figure 3.6 delineates a high salinity, high temperature LSW in the upper ~30 meters, which lies on top of the MAW placed between ~35 and90 m. Below MAW, LIW covered the depths between ~90 to ~250 meters. The salinity decreased smoothly in the DW with depth and had a minimum value of 38.75.

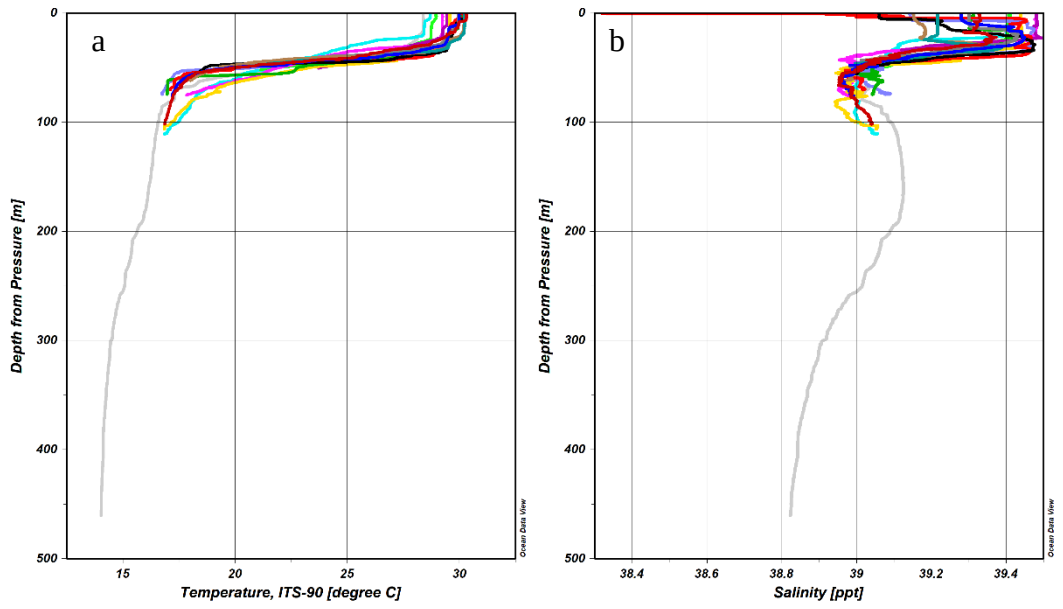

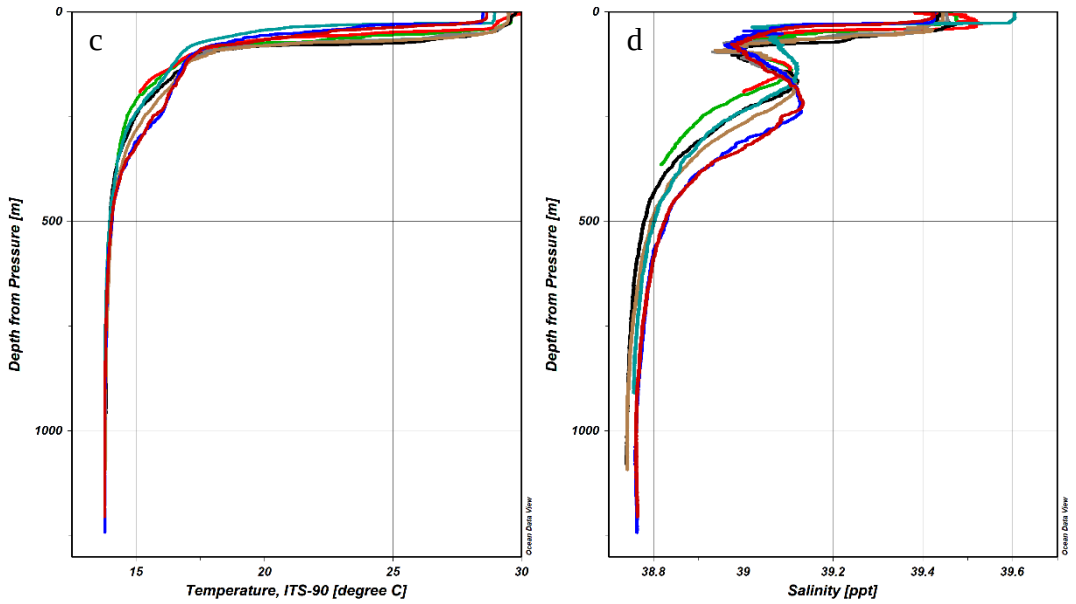

Figure 3.6. Temperature and salinity profiles in dry season for coastal (a, b) and offshore (c, d) stations.

The minimum surface salinity value, 38.42, was reached at St-021 which was located near to Ceyhan River. In general, İskenderun Bay salinity values were lower compared to other stations despite the fact that the bay had the highest temperature values. Moreover, the bay had the lowest surface DO concentrations (lowest 185.00 µM), in contrast with the results of the wet season cruise. There were oxygen minimum zones between 40-50 m depths in the İskenderun Bay, with a minimum value of 115.76 µM (51.11% saturation) at the St-028.

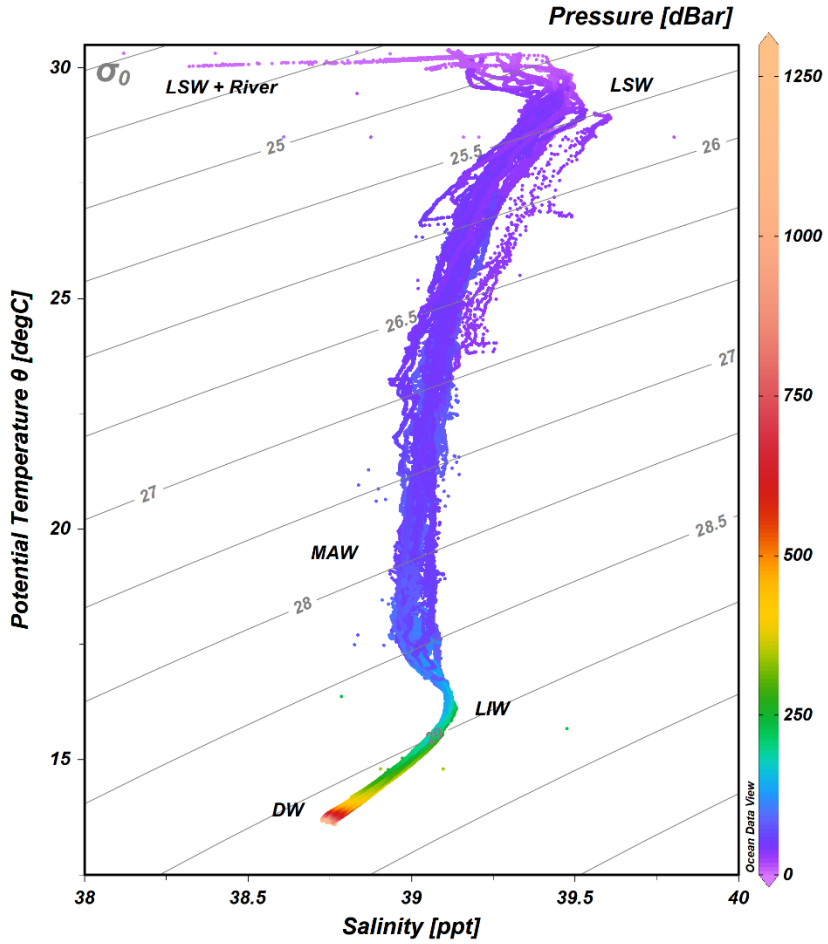

Figure 3.7. T-S (temperature-salinity) diagram showing the water bodies observed in dry season survey. Each dot shows the profile data on the stations, and the color palette shows the pressure/depth. Gray lines are isopycnals.

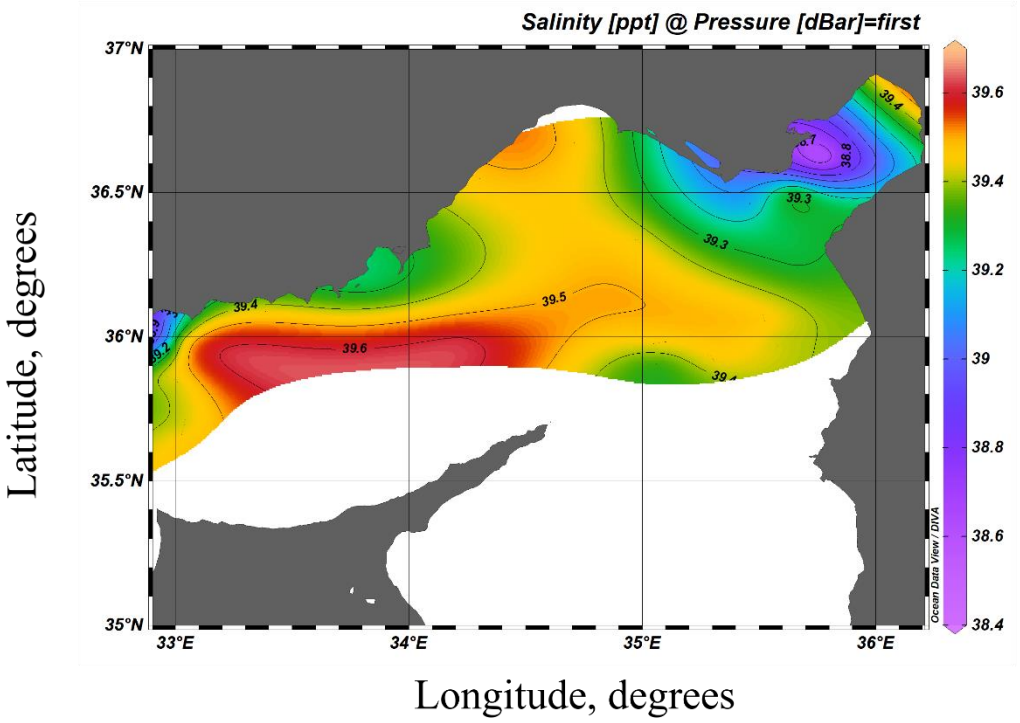

Figure 3.8. September 2022 Sea surface salinity map

3. 1. 3. Nutrient Distribution

3. 1. 3. 1. Riverine nutrient loads

The nutrient concentrations were analyzed in a total of nine different rivers. Although the surveys were conducted in 2022, only the results of one wet season samplings and one dry season samplings are presented here as the verification analyses are still ongoing. The highest PO_4^{3-} and DIN concentrations were found in Deliçay River (Hatay) and Anamur River, respectively, in the wet season (Table 4) with concentrations of 2.77 µM and 460.09 µM. Anamur River had the highest DIN:PO_4 ratio of 3539 where the average DIN:PO_4 of the remaining rivers had a value of 279 in the wet season. Another notable extreme value was found for NH_4^+ concentration in the Deliçay (Hatay), which had 133.39 µM, almost ten times of the second highest concentration in the wet season (Anamur River) (Table 4).

Table 4. River nutrient concentrations

River	PO_4 (µM)	DIN (µM)	NH_4 (µM)	Si (µM)	DIN:PO_4	Season
Anamur	0.13	460.09	0.79	112.93	3539	Wet
Asi	2.02	197.97	14.41	247.57	98	Wet
Berdan	0.78	196.35	12.49	149.31	252	Wet
Ceyhan	0.79	271.05	9.65	137.66	343	Wet
Deliçay (Hatay)	2.77	147.51	133.39	47.49	53	Wet
Deliçay (Mersin)	0.62	145.16	2.21	122.29	234	Wet
Göksu	0.97	79.54	3.82	63.38	82	Wet
Lamas	0.12	115.97	0.86	111.62	966	Wet
Seyhan	0.52	105.58	16.6	130.63	203	Wet
Anamur	0.66	68.67	12.32	45.10	104	Dry
Asi	4.94	292.70	121.66	304.96	59	Dry
Berdan	0.58	107.61	19.10	100.99	186	Dry
Ceyhan	0.61	175.35	11.87	154.28	287	Dry
Deliçay (Hatay)	1.99	80.14	73.19	179.77	40	Dry
Deliçay (Mersin)	3.78	75.01	12.25	180.40	20	Dry
Göksu	0.71	61.66	16.89	78.71	87	Dry
Lamas	0.99	157.99	14.33	140.96	160	Dry
Seyhan	5.2	144.62	11.8	156.50	28	Dry

NH_4^+ concentrations were usually higher in the dry season except for Deliçay (Hatay) and Seyhan Rivers, where Asi River had the peak concentration of 121.66 µM. Conversely, Si concentrations were lower than the wet season concentrations with the exception of the concentrations in Anamur and Berdan Rivers (Table 5). Saliently, Asi River had the highest DIN, NH_4^+, and Si concentrations in the dry season. Moreover, the high PO_4^{3-} levels were observed in Seyhan, Asi, and Deliçay (Hatay) rivers with 5.2, 4.94, and 3.78 µM, respectively. Overall, the results revealed a strong decrease in DIN:PO_4 ratios in the dry season, with the sole instance Göksu River which had an increase from 82 to 87.

Overall, weighted-average concentrations according to the discharges revealed that the maximum PO_4^{3-} and NH_4^+ values were present in Deliçay (Hatay) river (Table 5). The values were more close to the wet season concentrations as it had the major portion of the annual discharge (General Directorate of State Hydraulic Works, Türkiye, 2018).

Table 5. Weighted-averages of river nutrient concentrations

River	PO_4(µM)	DIN(µM)	NH_4(µM)	Si(µM)	DIN:PO_4
Anamur	0.26	362.34	3.67	95.99	1381
Asi	2.39	209.87	27.88	254.78	88
Berdan	0.72	169.24	14.51	134.55	235
Ceyhan	0.73	237.95	10.42	143.41	327
Deliçay (Hatay)	2.62	134.56	121.82	72.91	51
Deliçay (Mersin)	0.85	140.05	2.94	126.52	165
Göksu	0.92	75.97	6.43	66.44	83
Lamas	0.25	122.32	2.89	116.05	487
Seyhan	0.90	108.76	16.21	132.74	121

The long-term averaged discharges and the most recent discharge data (2014-2015) along with the weighted-average nutrient concentrations revealed that total of 0.407, 35.469, 2.619, and 53.289 kT/yr (Table 6) and 0.457, 36.126, 3.096, and 57.351 kT/yr (Table 7) PO_4-P, DIN-N, NH_4-N, and SiO_4-Si loads for long-term averaged discharges and the recent discharge, respectively. Ceyhan River is the main contributor of DIN-N and SiO_4-Si with more than 50% and more than 38%, respectively, while Asi River had the highest loads of PO_4-P with more than 36% of total PO_4-P loads. Furthermore, DIN:PO_4-P ratio of total annual riverine discharge was higher than the Redfield Ratio, by the ratios of 79 and 87 for the recent year and

long-term calculations, respectively. All the rivers had weighted-average values greater than the Redfield ratio, while Anamur River had the highest.

Table 6. Annual riverine nutrient loads estimated by long-term discharge averages

River	Annual Discharge km³/Year	Annual PO_4-P Load kT/Year	Annual DIN-N Load kT/Year	Annual NH_4-N Load kT/Year	Annual SiO_4-Si Load kT/Year	DIN-N:PO_4-P
Anamur	0.735	0.006	3.728	0.038	1.981	624
Asi	2.018	0.149	5.929	0.788	14.438	40
Berdan	0.158	0.004	0.374	0.032	0.597	106
Ceyhan	5.997	0.135	19.979	0.875	24.156	148
Deliçay (Hatay)	0.124	0.010	0.234	0.212	0.254	23
Deliçay (Mersin)	0.046	0.001	0.090	0.002	0.162	74
Göksu	1.076	0.031	1.145	0.097	2.008	37
Lamas	0.087	0.001	0.148	0.004	0.283	220
Seyhan	2.524	0.070	3.843	0.573	9.409	55
TOTAL	**12.765**	**0.407**	**35.469**	**2.619**	**53.289**	**87**

Table 7. Annual riverine nutrient loads estimated by the available most recent year data (2014-2015)

River	Annual Discharge km³/Year	Annual PO_4-P Load kT/Year	Annual DIN-N Load kT/Year	Annual NH_4-N Load kT/Year	Annual SiO_4-Si Load kT/Year	DIN-N:PO_4-P
Anamur	0.679	0.006	3.446	0.035	1.831	624
Asi	2.467	0.182	7.249	0.963	17.654	40
Berdan	0.222	0.005	0.526	0.045	0.840	106
Ceyhan	5.442	0.123	18.130	0.794	21.920	148
Deliçay (Hatay)	0.245	0.020	0.462	0.418	0.502	23
Deliçay (Mersin)	0.062	0.002	0.123	0.003	0.222	74
Göksu	0.931	0.026	0.990	0.084	1.737	37
Lamas	0.095	0.001	0.163	0.004	0.310	220
Seyhan	3.309	0.092	5.038	0.751	12.335	55
TOTAL	**13.453**	**0.457**	**36.126**	**3.096**	**57.351**	**79**

3. 1. 3. 2. Groundwater nutrient concentrations

A total of 87 groundwater samples were analyzed for PO_4^{3-}, NO_3^-+NO_2, NO_2, NH_4^+ and Si from 10 sites (Appendix C). Two of them are located in METU-IMS with different depths and two of them are neighbor wells in Göksu delta. Correlation analysis indicated that there is a significant negative correlation between PO_4^{3-} and DIN, however NH_4^+ is positively and strongly correlated with PO_4^{3-} (Figure 3.9). Furthermore, Shapiro-Wilk Normality test showed that none of the nutrients were distributed normally, therefore median values of nutrient concentrations for each site were used in the SGD-associated nutrient flux estimation to obtain robust statistics. One-way analysis of variance (ANOVA) test without assuming equal variances revealed that Si concentrations are significantly different between wet and dry seasons (*p*-value = 0.0013, Eta2 = 0.15). In general, the dry season Si concentrations were higher than the wet season concentrations (Figure 3.10).

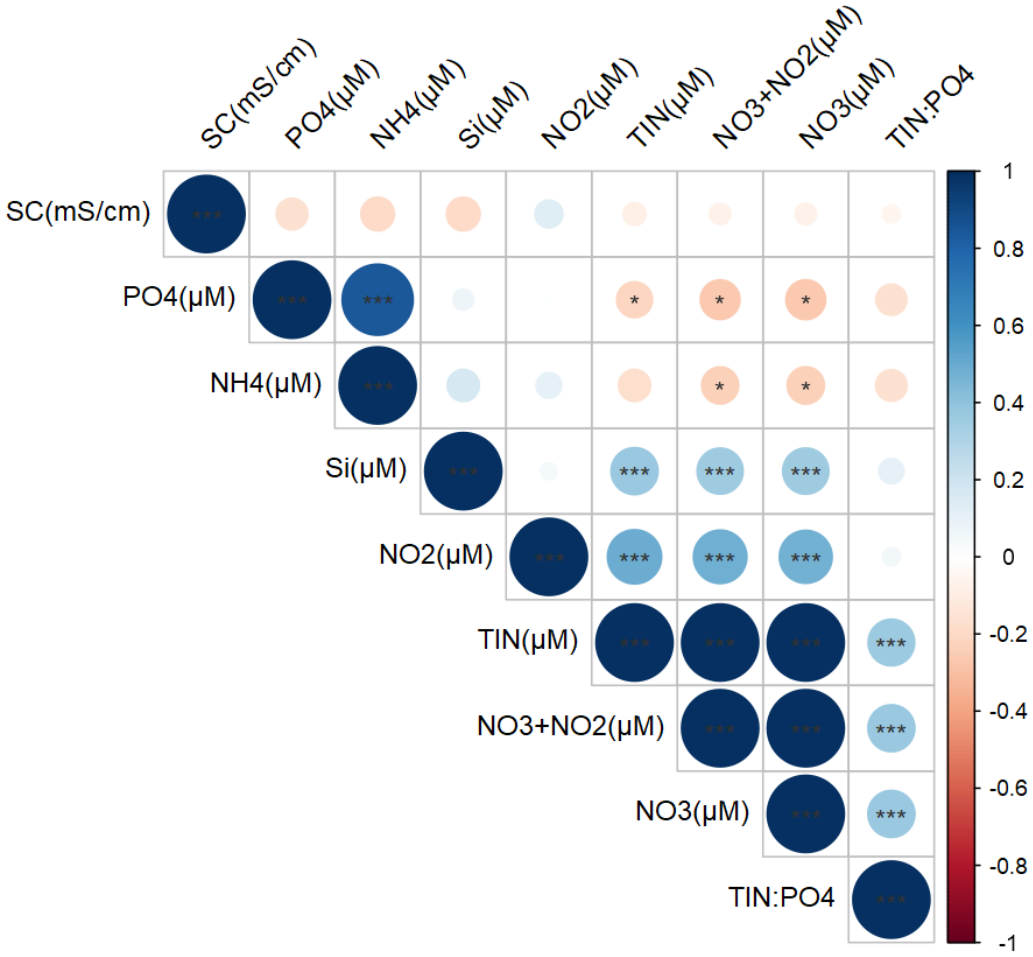

Figure 3.9. Correlation plot of groundwater nutrient concentrations. Color bar: correlation coefficient with significance symbols, *: p<0.05, **: p<0.01, ***: p<0.001.

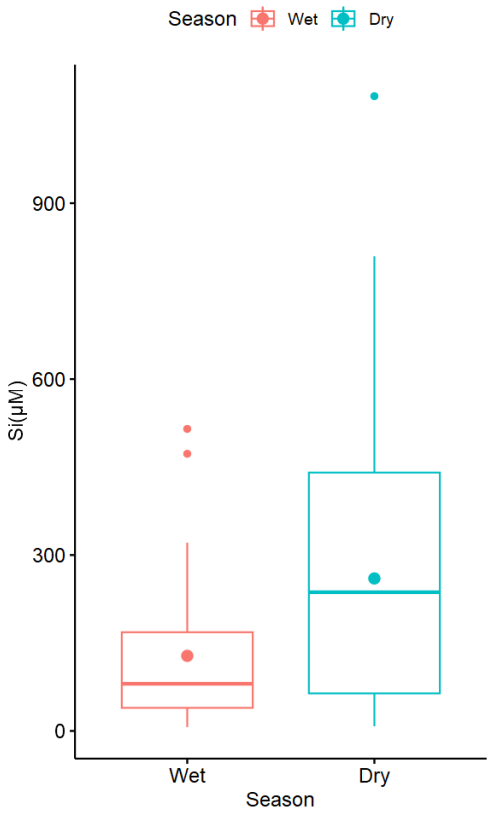

Figure 3.10. Box plot of Si concentrations in groundwater in wet and dry seasons

Table 8 provides the median and mean concentrations of nutrients in each groundwater sampling site. Göksu 1 groundwater had the highest PO_4^{3-} (mean: 6.55 µM; median: 6.28 µM) values by a large difference between the second highest, Dörtyol (mean: 0.71 µM; median: 0.98 µM). Dörtyol had the highest concentrations of DIN (mean: 449.69 µM; median: 529.85 µM) and Si (mean: 432.20 µM; median: 339.67 µM), whereas Göksu 1 had the maximum NH_4^+ levels (mean: 46.30 µM; median: 46.65 µM). In addition, the coastal deep well located in the IMS (IMS 50) had the highest and extreme mean DIN:PO_4 ratio of 4402.95 with a median value of 1523.29 (n=8).

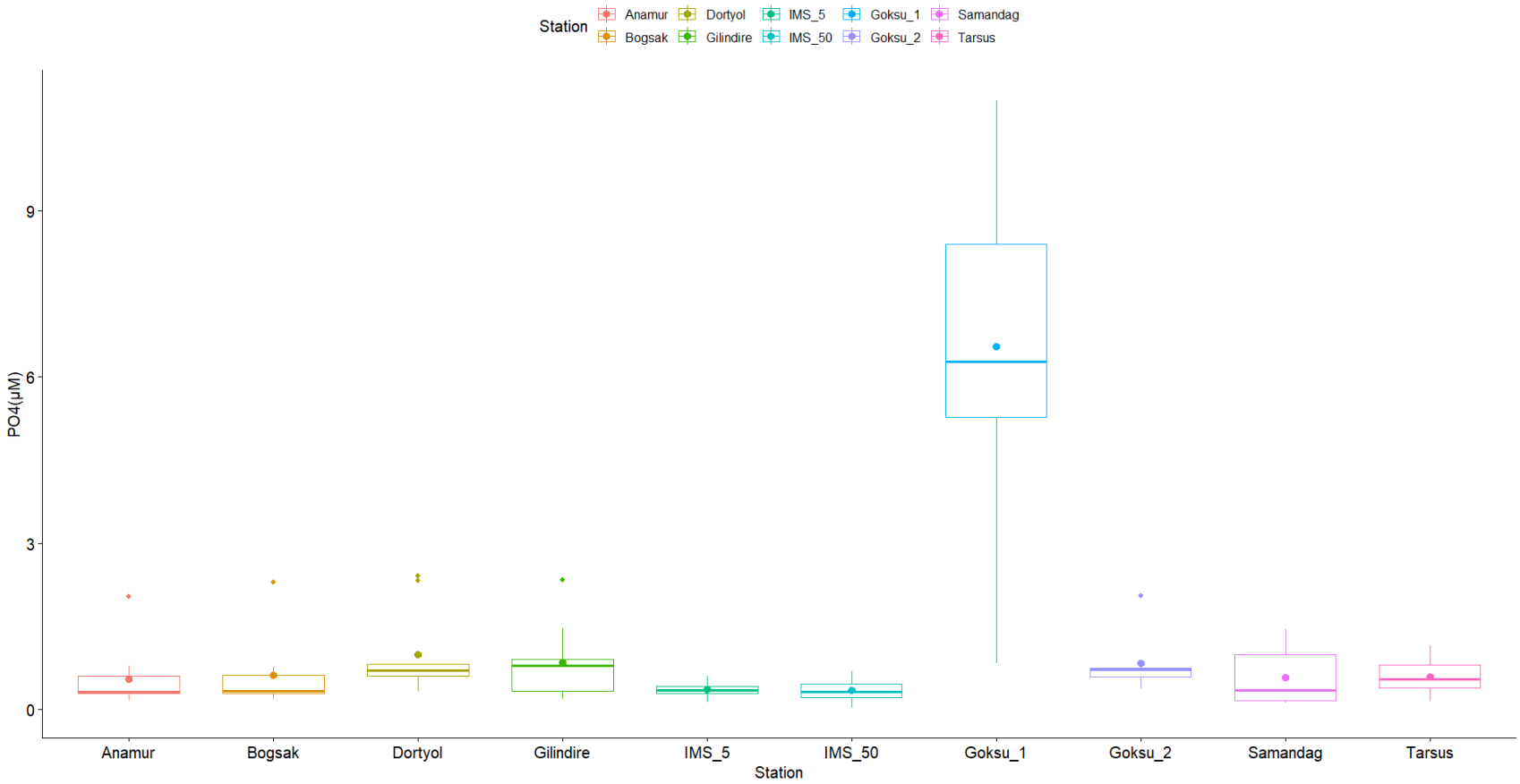

Figure 3.11. Box-plot of PO_4 concentrations in groundwater stations, large points depict average values and small points as outliers

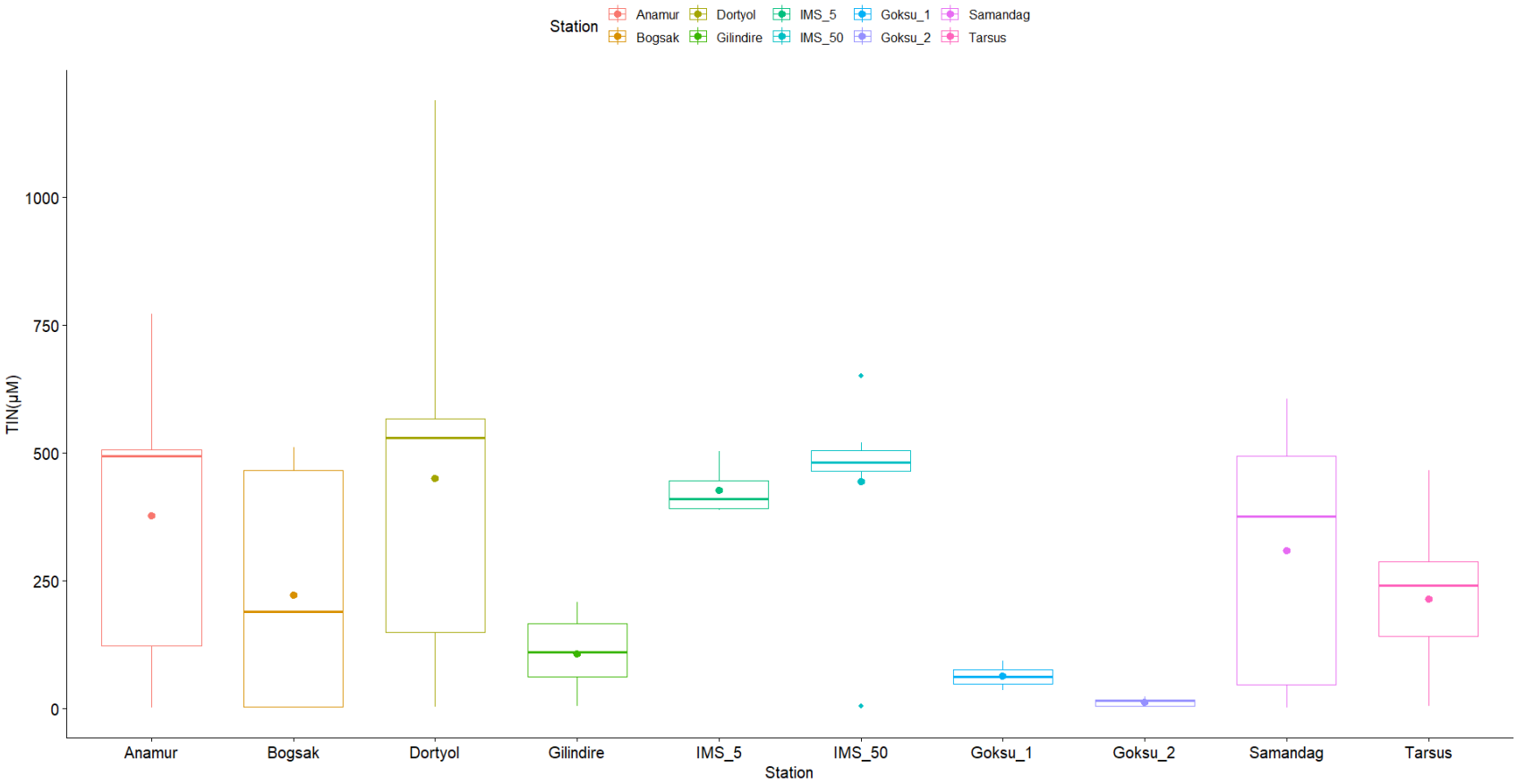

Figure 3.12. Box-plot of TIN concentrations in groundwater stations, large points depict average values and small points as outliers

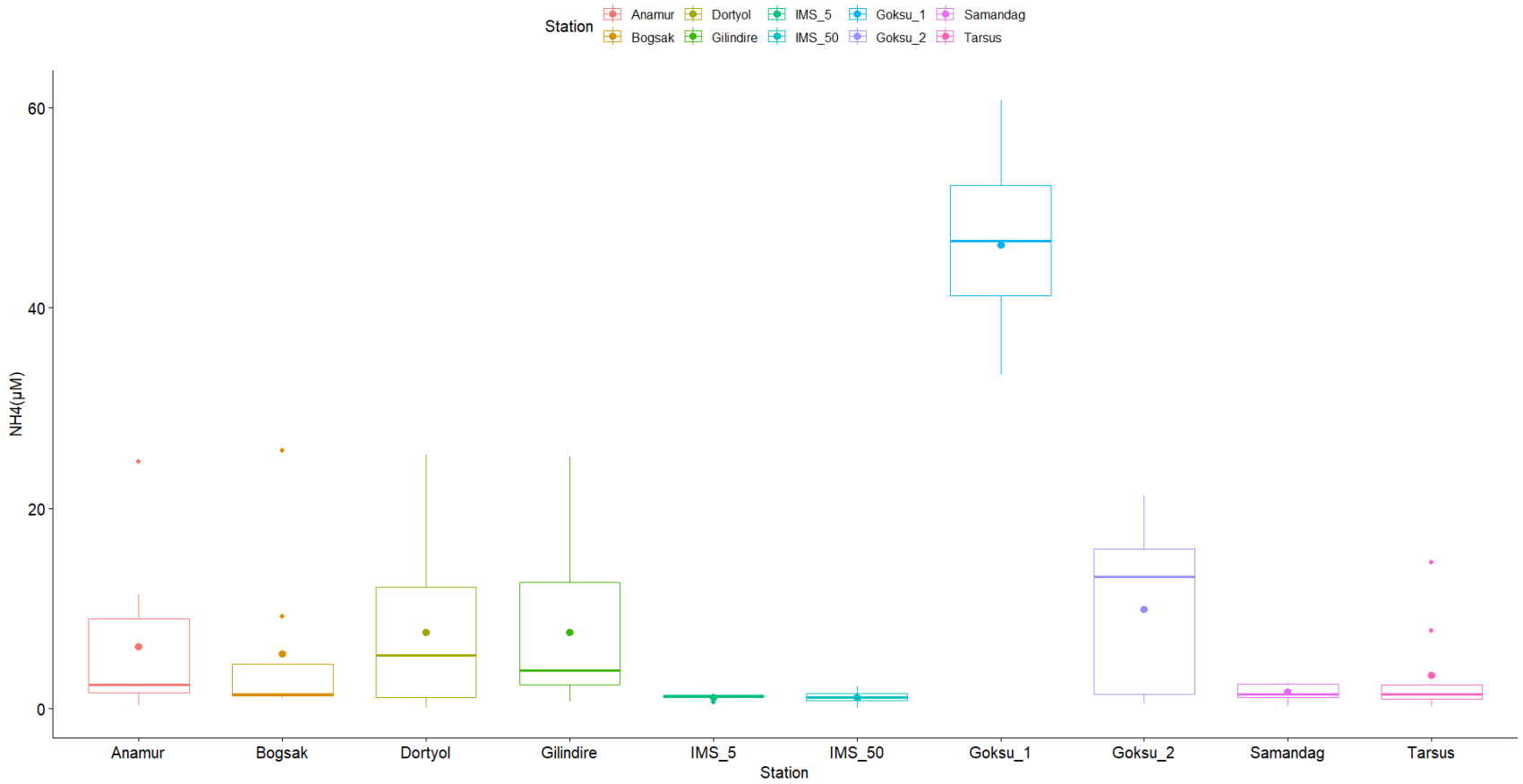

Figure 3.13. Box-plot of NH_4 concentrations in groundwater stations, large points depict average values and small points as outliers

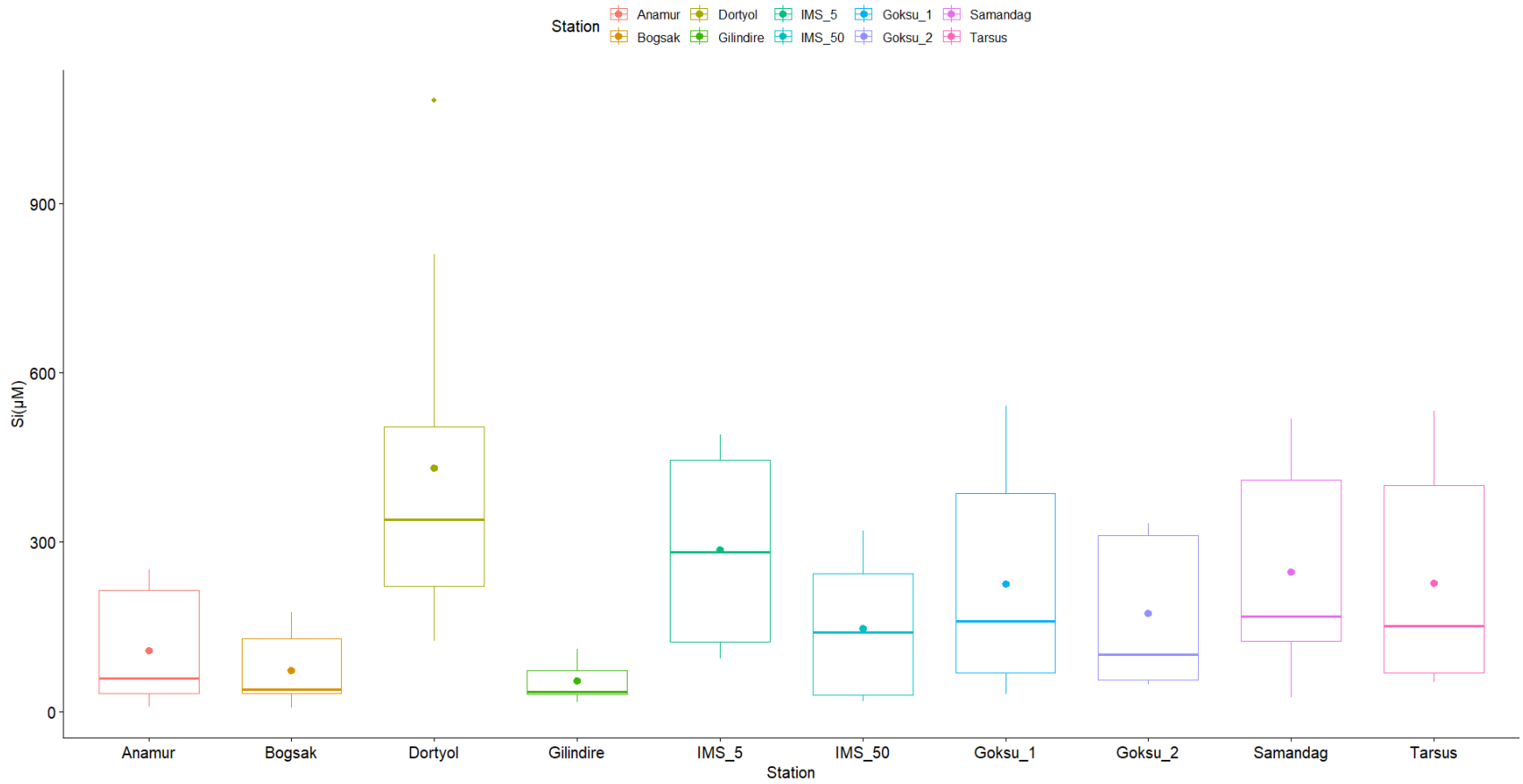

Figure 3.14. Box-plot of Si concentrations in groundwater stations, large points depict average values and small points as outliers

Table 8. Median and mean concentrations of nutrients in groundwater

Station	PO_4(µM)		NH_4(µM)		DIN(µM)		Si(µM)		DIN:PO_4	
	median	**mean**	**median**	**mean**	**median**	**mean**	**median**	**mean**	**median**	**mean**
Anamur	0.32	0.54	2.40	6.17	493.23	377.03	58.01	107.62	702.56	843.63
Boğsak	0.33	0.62	1.41	5.50	189.30	222.61	39.33	72.25	203.13	368.14
Dörtyol	0.71	0.98	5.29	7.63	529.85	449.69	339.67	432.20	677.43	612.01
Gilindire	0.79	0.84	3.77	7.58	110.19	107.87	34.64	54.10	113.82	243.17
Göksu 1	6.28	6.55	46.65	46.30	62.39	63.31	160.61	226.43	12.26	13.68
Göksu 2	0.72	0.83	13.13	9.93	15.31	12.48	100.83	173.74	11.68	18.37
IMS 5	0.35	0.36	1.26	1.15	409.43	427.30	281.77	287.01	1288.19	1575.51
IMS 50	0.32	0.34	1.10	1.12	481.16	443.83	139.71	147.59	1523.29	4402.95
Samandağ	0.34	0.57	1.45	1.67	375.35	308.91	168.33	246.50	301.16	1177.11
Tarsus	0.54	0.58	1.42	3.31	240.99	213.71	151.08	227.26	284.73	658.74
OVERALL	**0.60**	**1.32**	**2.21**	**9.84**	**184.89**	**258.02**	**124.41**	**196.35**	**250.40**	**921.93**

3. 2. Residence Time

The residence time of the Cilician Basin was estimated for the first time, using two different approaches, namely, utilizing the CMEMS product and particle tracking model. In the latter one, the residence time was assessed for only upper 600 meters depth of the basin in order to calculate offshore exchange rates of the box model, where the residence time the whole water body in the basin was calculated in the first method to assess a broader scale circulation dynamics and associated variatons between different years.

3. 2. 1. Hydrodynamic Model Product

Digitizing GEBCO bathymetry data using QGIS software as decribed in **Chapter 2** revealed that the water volume of the basin equals to approximately 14645 km³. Table 9 lists the annual volume transport through the southern boundary, Cape Karpass – Latakia. The average residence time was 172± 34 days, and ranged between 133 and 215, indicating significant inter-annual variability. The maximum annual volume transport was 40170 km^3 in 2019, and the minimum was 27831 in 2020.

Table 9. Volume transports and associated residence time values.

Year	Transport (km³/yr)	Residence time (days)
2016	37346	143
2017	27831	192
2018	29951	178
2019	40170	133
2020	24884	215

3. 2. 2. Particle Tracking Model

Particle tracking model results revealed that the residence time varied significantly with depth. The simulation time was not sufficient to calculate residence time of IL

after 13 months (Figure 3.15) as the median value had not yet been reached. Therefore, to avoid any bias towards lower values, first the time-averages of each depth were taken, then the residence time was calculated as the depth-average. That corresponded to approximately 345 days of residence time for the control volume (Table 10).

Table 10. Summary of residence times calculated by the particle tracking model according to layers

Layers	RT, days
0-150 m (Surface Layer)	55
150-600 m (Intermediate Layer)	442
Weighted average	345

Seasonal and inter-annual variations in the average residence time were much higher in the first 400 m depth with a maximum of 70% variation between dry (158 days) and wet (93 days) seasons in 2019. The seasonal variation in the RT of SL reached its maximum, 304% in 2019. Furthermore, the highest inter-annual variation was 36% in SL (between 2020 and 2021). For the deeper layer, 400-600 m, the seasonal variation in the average residence time was lower than 1%. Moreover, mixing paterns were observed during winter periods by a homogenization in the residence times in the first 200 meters. This effect was weeker in the 2021, yet its effects lasted longer than previous two years.

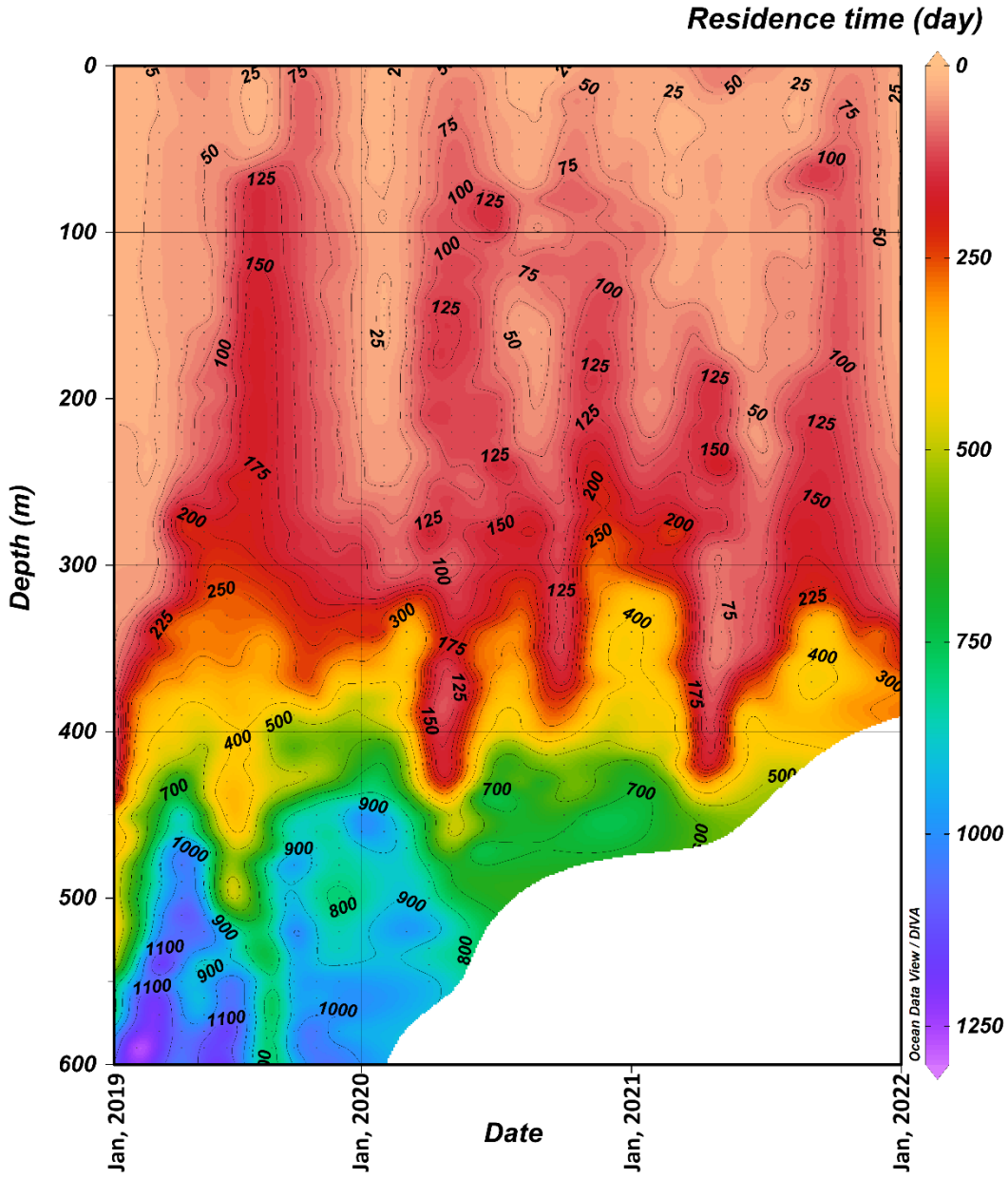

Figure 3.15. Residence times calculated with the particle tracking model.

3. 2. 3. ARGO Float

Moreover, an ARGO float trajectory (World Meteorological Organization #6901876) was analyzed. It entered the basin on December 12, 2015 from the

southern boundary and left on January 12, 2016 (Figure 3.16). Even though it went up to 900 m depths for the stations to get profiles, it resided 31 days in the basin (https://fleetmonitoring.euro-argo.eu/).

Figure 3.16. Trajectory of the ARGO float. Numbers denote the profile IDs.

3. 3. Radium Activities

3. 3. 1. Cilician Basin

Overall, two-hundred-and-eight Radium samples were taken in two basin-wide cruises. Yet, thirty-eight samples were analyzed for Radium within the scope of this study, and they were all wet season samples. Table 11 provides ^{226}Ra and ^{228}Ra activities and associated errors of 38 seawater, 15 catchment (8 rivers, 7 wells) samples from our wet season cruise and catchment survey, in addition to the 17 pilot study samples. Seawater samples consists of 15 stations which all have surface

(depth = 3m) activities. St-001, St-002, St-004, St-007, St-010, St-014, St-015, and St-017 also include samples analyzed and presented at different depths. METU IMS Wells SK-5 and SK-50 from the wet season catchment field expedition were absent, however, the activities were measured from earlier pilot samplings (October and December 2021).

The surface ^{228}Ra activities have a range between 15.61-44.40 dpm/m^3 with a mean activity of 26.83 dpm/m^3 (median activity of 26.90 dpm/m^3). The activities found at the surface of western boundary, where the major outflow occurs, have higher activities (44.4, 35.84 dpm/m^3) than southern inflow boundary (29.5, 18.92 dpm/m^3) with the exception of St-014 (25.86 dpm/m^3). All surface activities are higher than deep sample activities (depth >600). In the stations between 3m and 150m depths, generally there was an increase in ^{228}Ra activities with depth. In contrast, activities are consistently lower in the samples collected at >150 m and reach minimums at depths >= 600m except for St-002, 40 m sample which had 18.90 dpm/m³. Figure 3.19 demonstrates the ^{228}Ra activity distribution according to the seawater layers. Correlation tests revealed that ^{228}Ra activities were not correlated with the salinities, however, there was significant negative correlation between ^{228}Ra activities and depth (Pearson's product-moment correlation coefficient: -0.76, p-value: 2.6 x 10^{-8})

Table 11. Radium activities

Sample ID	**Date**	**Station**	**Depth (m)**	**^{228}Ra dpm. m^{-3}**	**^{228}Ra error %**	**^{226}Ra dpm. m^{-3}**	**^{226}Ra error %**
1	10/13/2021	Offshore Surface (in-Series) 1	3	12.21	24.39	143.56	2.62
2	10/13/2021	Offshore Surface (in-Series) 2	3	0.00	0.00	16.43	16.80
4	10/13/2021	Offshore Deep	580	7.47	15.94	202.50	1.08
5	10/13/2021	Coastal Surface (in-Series) 1	3	25.75	12.57	169.60	2.40

Sample ID	Date	Station	Depth (m)	^{228}Ra dpm. m^{-3}	^{228}Ra error %	^{226}Ra dpm. m^{-3}	^{226}Ra error %
6	10/13/2021	Coastal Surface (in-Series) 2	3	0.00	0.00	11.90	19.20
8	10/13/2021	Coastal Deep 1	20	20.90	10.69	148.46	2.12
10	10/19/2021	IMS SK5 (in-series) 1	5	14.35	14.67	17.64	13.08
11	10/19/2021	IMS SK5 (in-series) 2	5	0.88	298.15	0.00	0.00
13	10/19/2021	IMS SK50 (in-series) 1	50	61.64	5.27	163.34	2.31
14	10/19/2021	IMS SK50 (in-series) 2	50	0.00	0.00	6.03	39.11
16	10/20/2021	Lamas River (in-series) 1	-	32.27	10.30	493.43	1.22
31	12/13/2021	Asi River – US	-	37.73	14.33	327.24	2.52
32	12/13/2021	Asi River – TR	-	44.35	12.41	315.86	2.57
34	12/15/2021	IMS SK50 – US fiber	50	84.00	7.85	195.85	3.24
35	12/15/2021	IMS SK50 – TR fiber	50	75.81	7.53	201.95	3.12
36	12/15/2021	Lamas River - US	-	33.18	17.93	479.78	1.73
37	12/15/2021	Lamas River - TR	-	26.99	13.63	482.39	1.61
38	3/2/2022	Anamur River	-	118.98	3.10	343.48	1.30
39	3/2/2022	Anamur Well	18	63.26	5.81	12.92	3.32
40	3/2/2022	Gilindire Cave	-	138.33	3.64	368.29	1.71
41	3/2/2022	Boğsak Well	1.5	89.75	4.35	428.61	1.33
42	3/2/2022	Göksu Well	9	257.73	2.51	388.80	1.64
43	3/2/2022	Göksu River	-	89.59	6.92	530.98	1.75
44	3/3/2022	Berdan River	-	144.49	3.77	474.30	1.57
45	3/3/2022	Tarsus Well	120	94.31	5.98	265.09	2.53
46	3/3/2022	Seyhan River	-	90.57	5.08	239.31	2.28
47	3/4/2022	Ceyhan River	-	110.75	4.23	335.66	1.76
48	3/4/2022	Dörtyol Well	32	62.90	6.31	437.81	1.45

Sample ID	Date	Station	Depth (m)	^{228}Ra dpm. m^{-3}	^{228}Ra error %	^{226}Ra dpm. m^{-3}	^{226}Ra error %
49	3/4/2022	Deliçay (Hatay) River	-	174.13	5.38	918.01	1.50
50	3/4/2022	Asi River	-	124.36	4.00	583.59	1.24
51	3/4/2022	Samandağ Well	30	43.12	9.35	228.93	2.55
52	3/10/2022	Lamas River	-	40.61	8.14	408.22	1.29
63	4/13/2022	St-012	3	26.90	13.65	155.20	2.67
66	4/13/2022	St-013	3	20.68	15.92	145.20	2.42
69	4/14/2022	St-016	3	35.84	20.25	194.31	3.79
74	4/14/2022	St-015	3	44.4	10.18	167.35	3
75	4/14/2022	St-015	1177	8.1	15.18	21	0.91
77	4/14/2022	St-015	600	3.16	159.78	224.01	2.59
78	4/14/2022	St-015	300	19.78	17.42	199.14	2.15
79	4/14/2022	St-015	160	38.146	15.25	215.48	2.96
81	4/14/2022	St-014	3	25.86	26.31	207.67	3.37
84	4/14/2022	St-014	160	18.71	20.55	167.78	2.64
86	4/14/2022	St-001	3	16.32	30.63	173.17	2.98
87	4/15/2022	St-001	917	7.8	14.91	161.16	1.04
88	4/15/2022	St-001	875	10.68	19.88	216.29	1.47
89	4/15/2022	St-001	600	9.35	26.08	183.34	1.7
90	4/15/2022	St-001	250	11.63	19.57	128.63	1.89
91	4/15/2022	St-001	100	35.71	15.85	184.67	3.15
92	4/15/2022	St-001	40	24.58	15.93	171.66	2.55
93	4/15/2022	St-002	3	29.5	9.59	174.2	1.87
95	4/15/2022	St-002	600	18.90	14.39	233.32	1.56
96	4/15/2022	St-002	250	15.64	28.82	191.7	2.74
97	4/15/2022	St-002	40	25.03	19.71	170.81	3.1
98	4/15/2022	St-002	1083	6.57	33.59	201.32	1.51
104	4/15/2022	St-004	3	18.92	14.1	173.13	1.74
105	4/15/2022	St-004	340	15.32	27.4	224.89	2.24
106	4/15/2022	St-004	225	23.87	16.99	181.65	2.67
107	4/15/2022	St-004	150	19.43	12.29	135.1	1.94
108	4/15/2022	St-004	40	29.33	11.37	161.05	2.47
109	4/15/2022	St-005	3	32.42	13.19	172.86	2.77
112	4/15/2022	St-018	3	15.61	14.23	106.10	2.09
116	4/16/2022	St-007	3	30.29	11.4	150.3	2.43
117	4/16/2022	St-007	62	25.87	9.96	138.04	1.96
127	4/16/2022	St-009	3	33.01	11.52	155.58	2.7
131	4/16/2022	St-017	3	21.6	13.24	140.39	2.07

Sample ID	Date	Station	Depth (m)	^{228}Ra dpm. m^{-3}	^{228}Ra error %	^{226}Ra dpm. m^{-3}	^{226}Ra error %
132	4/16/2022	St-017	105	15.94	16.74	137.93	1.94
133	4/16/2022	St-017	30	26.28	10.69	168.85	2.11
135	4/16/2022	St-010	3	16.69	22.65	162.43	2.35
136	4/16/2022	St-010	47	29.53	9.88	158.16	2.11
138	4/16/2022	St-011	3	34.47	8.94	141.03	2.25

The groundwater end-member activities ranged from 14.35 to 257.73 dpm/m^3 with a mean value of 94.19 dpm/m^3 (median=84.00, Q1=62.90, Q3=94.31 dpm/m^3). The river end-member activities ranged from 40.61 to 174.13 dpm/m^3 with a mean activity of 111.68 dpm/m³ (median=114.86, Q1=90.32, Q3=129.39 dpm/m^3). Göksu groundwater sample had significantly high activity (257.73) as it is almost double that of the second highest groundwater activity (Gilindire - 138.33 dpm/m^3). On the other hand, Lamas River had the lowest activity among river samples as it is lower than half of the second lowest activity in rivers (Göksu River, 89.59 dpm/m^3).

Replicate samples and in series fibers experiments indicated that the both fibers are sufficient to adsorb radium efficiently except for the sample #133, that the second fiber in-series had an activity of 10.73 dpm/m³. For that reason, the activity in St-017 30 m depth was assumed to be the activity found in sample #133.

Figure 3.17 shows the ^{228}Ra activities of the seawater samples at 3m depth, wells, and rivers, where the surface activity map is given in the Figure 3.18.

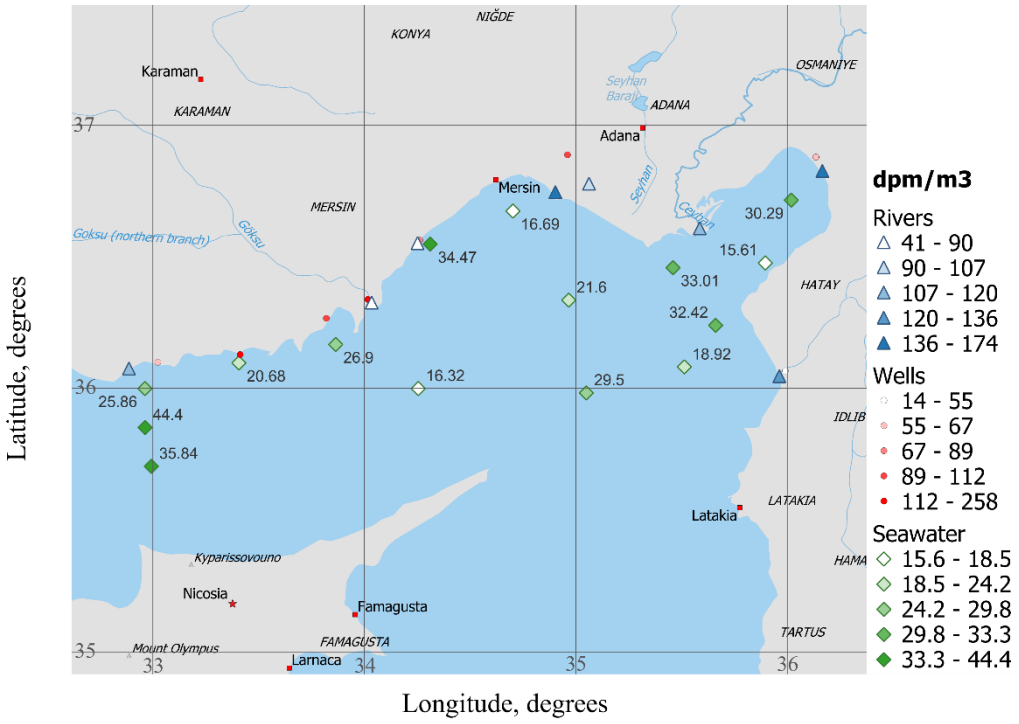

Figure 3.17. Surface ^{228}Ra activities in wet season samplings (Green: surface sea water; Red: groundwater; Blue: rivers)

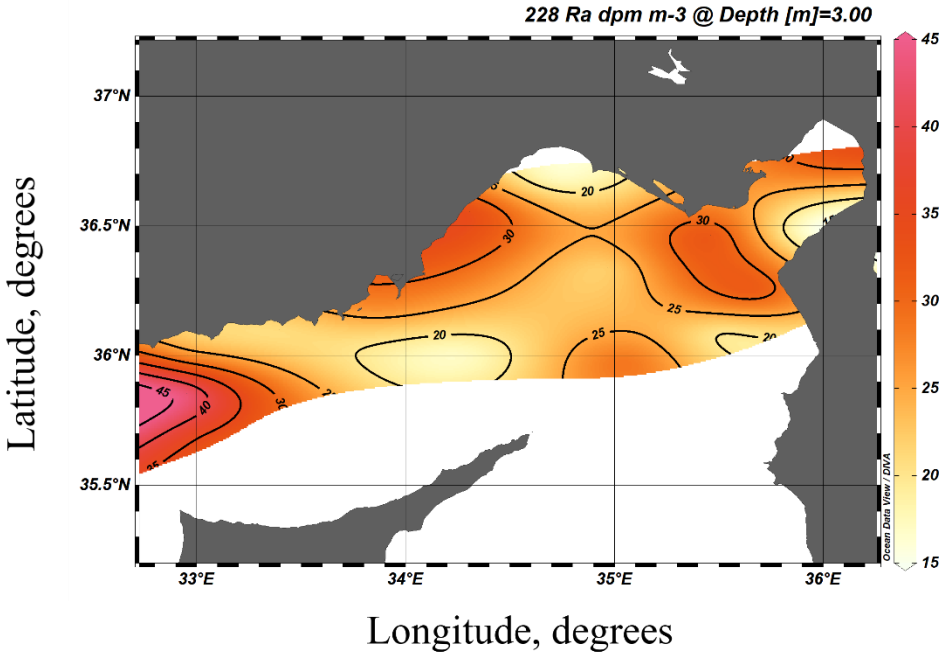

Figure 3.18. Map of ^{228}Ra activities in the surface seawater samples

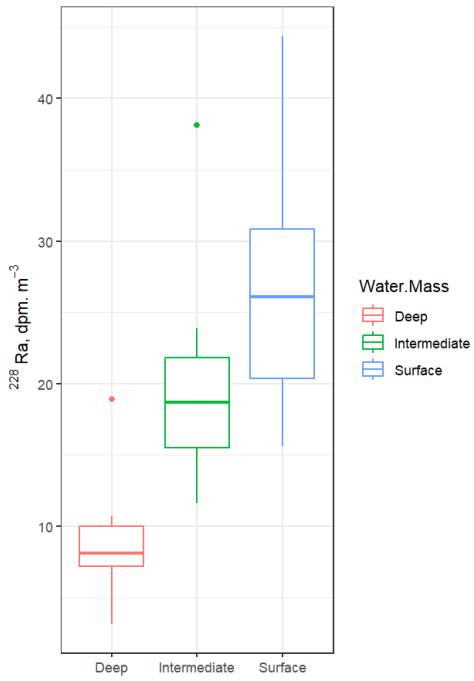

Figure 3.19. ^{228}Ra activity box-plot according to seawater layers

^{228}Ra to ^{226}Ra activity ratios (AR) had a range between 0.66 to 0.01 except for one significantly high value found in Anamur groundwater sample (Sample ID: 39, AR = 4.90). Kruskal-Wallis test revealed that there was no significant difference between river and groundwater samples and the differences were significant between seawater and river, and between seawater and groundwater samples regardless of the inclusion of the obvious outlier, sample 39 (Figure 3.20). Similarly, designated seawater layers were significantly different from each other (Figure 3.21). One relatively high AR (~0.386) was found at 1177 m depth of outflow station, St-015, which is the deepest sample.

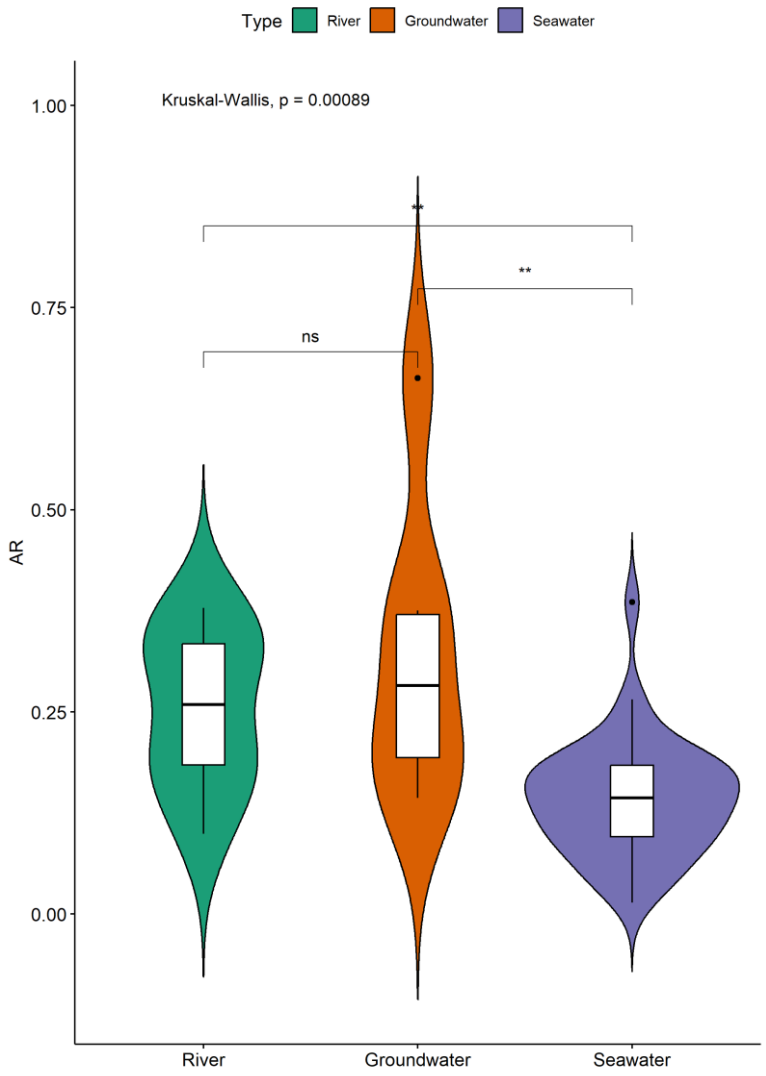

Figure 3.20. Violin plot of AR values according to sample type (**: $p \leq 0.01$, ns (non-significant): $p > 0.05$)

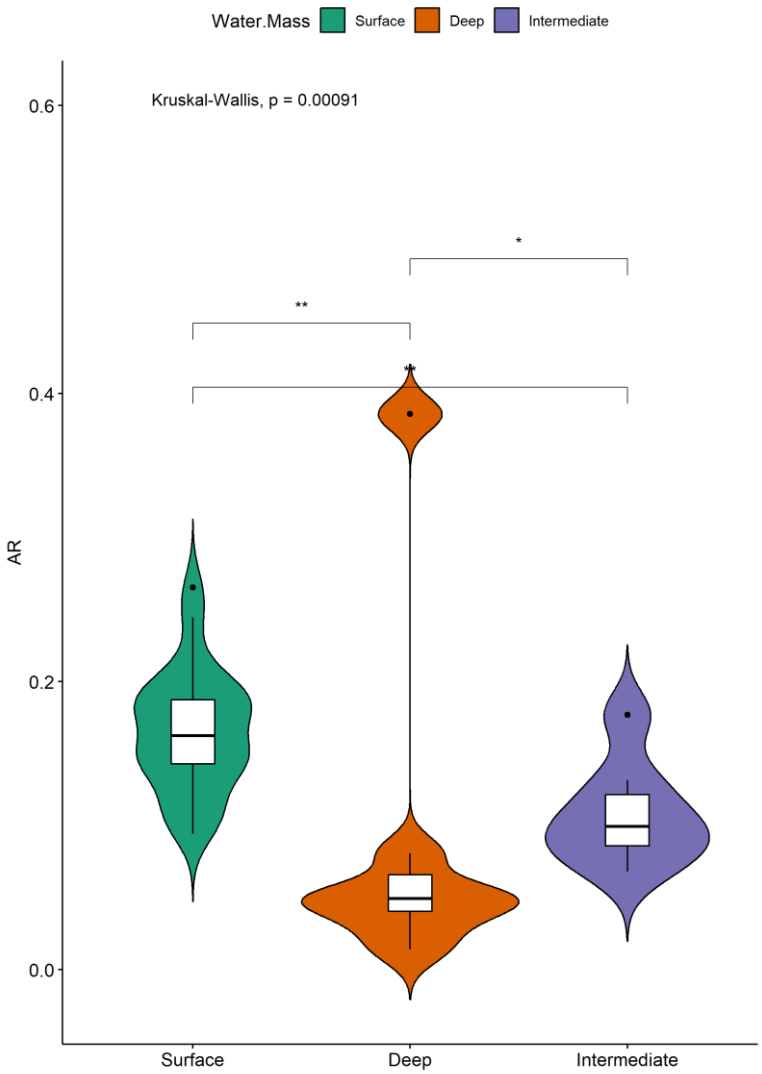

Figure 3.21. Violin plot of AR values of seawater according to layer (*: $p \leq 0.05$, **: $p \leq 0.01$)

3. 3. 2. İskenderun Bay

The ^{228}Ra activities measured in the İskenderun Bay ranged between 31.1 and 91.2 dpm/m³ with a mean activity of 61.35 dpm/m³ (Table 12). Eight samples were from the surface (3 m depth) (Figure 3.22), out of the thirteen samples analyzed. Other five samples were from various depths at three different stations. The deeper waters had a higher average activity than surface waters, yet there were not enough data to

statistically interpret differences. The results were not compared with the Cilician Basin activities as the detectors were not inter-calibrated.

The highest activity was found in St-021 at 20 m depth, contrasting the activities measured in the vicinity of St-021 (St-032: 31.1 dpm/m³, St-034: 37.9 dpm/m³). The Shapiro-Wilk test revealed that the normal distribution can be assumed. Therefore, the average activity was used to determine ^{228}Ra activity in the bay. Figures 3.23 and 3.24 shows the interpolated and extrapolated surface activities in the bay as described in the Chapter 2.

Table 12. İskenderun Bay ^{228}Ra activities

Sample ID	Date	Station	Lat	Long	Depth (m)	228-Ra, dpm/m3
218	3.09.2022	St-006	36.482	35.902	45	81.1
219	3.09.2022	St-006	36.482	35.902	33	53.8
220	3.09.2022	St-007	36.591	35.981	3	55.4
221	3.09.2022	St-030	36.537	35.950	3	49.6
222	3.09.2022	St-029	36.623	36.047	3	57.7
226	3.09.2022	St-018	36.774	36.125	3	80.0
227	3.09.2022	St-019	36.818	35.990	49	71.2
229	3.09.2022	St-025	36.801	36.049	3	52.8
233	3.09.2022	St-023	36.658	35.908	3	65.2
238	3.09.2022	St-032	36.687	35.774	3	31.1
240	3.09.2022	St-021	36.611	35.775	60	70.6
241	3.09.2022	St-021	36.611	35.775	20	91.2
242	3.09.2022	St-034	36.550	35.823	3	37.9

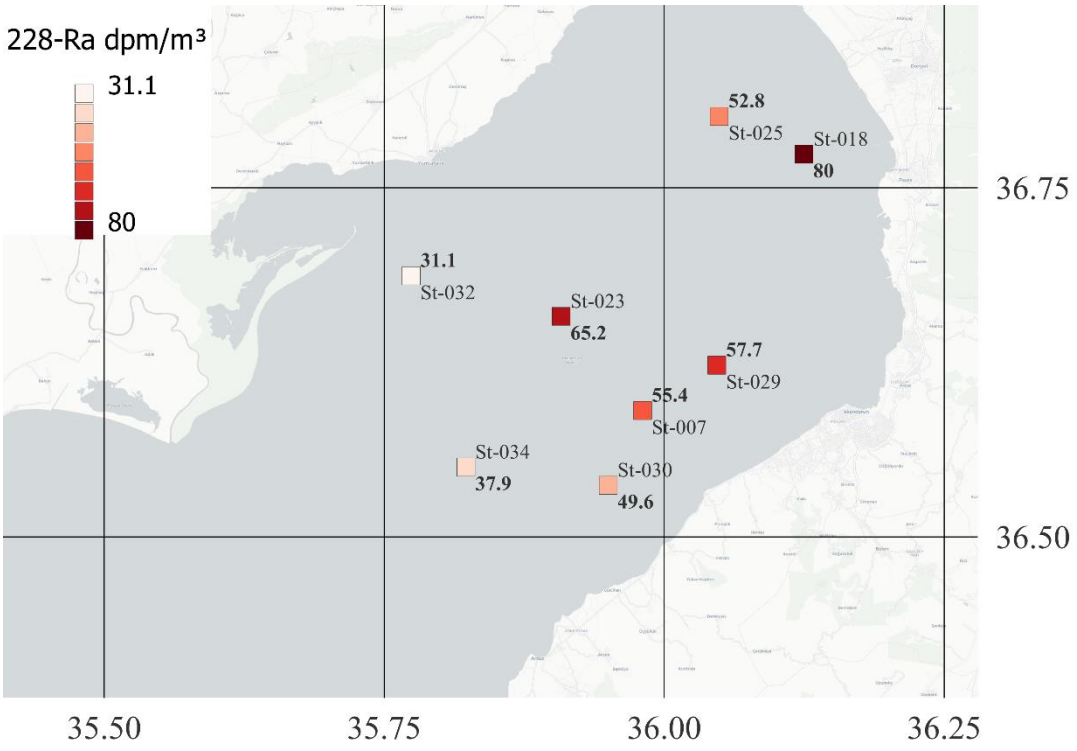

Figure 3.22. ^{228}Ra activities of İskenderun Bay surface waters

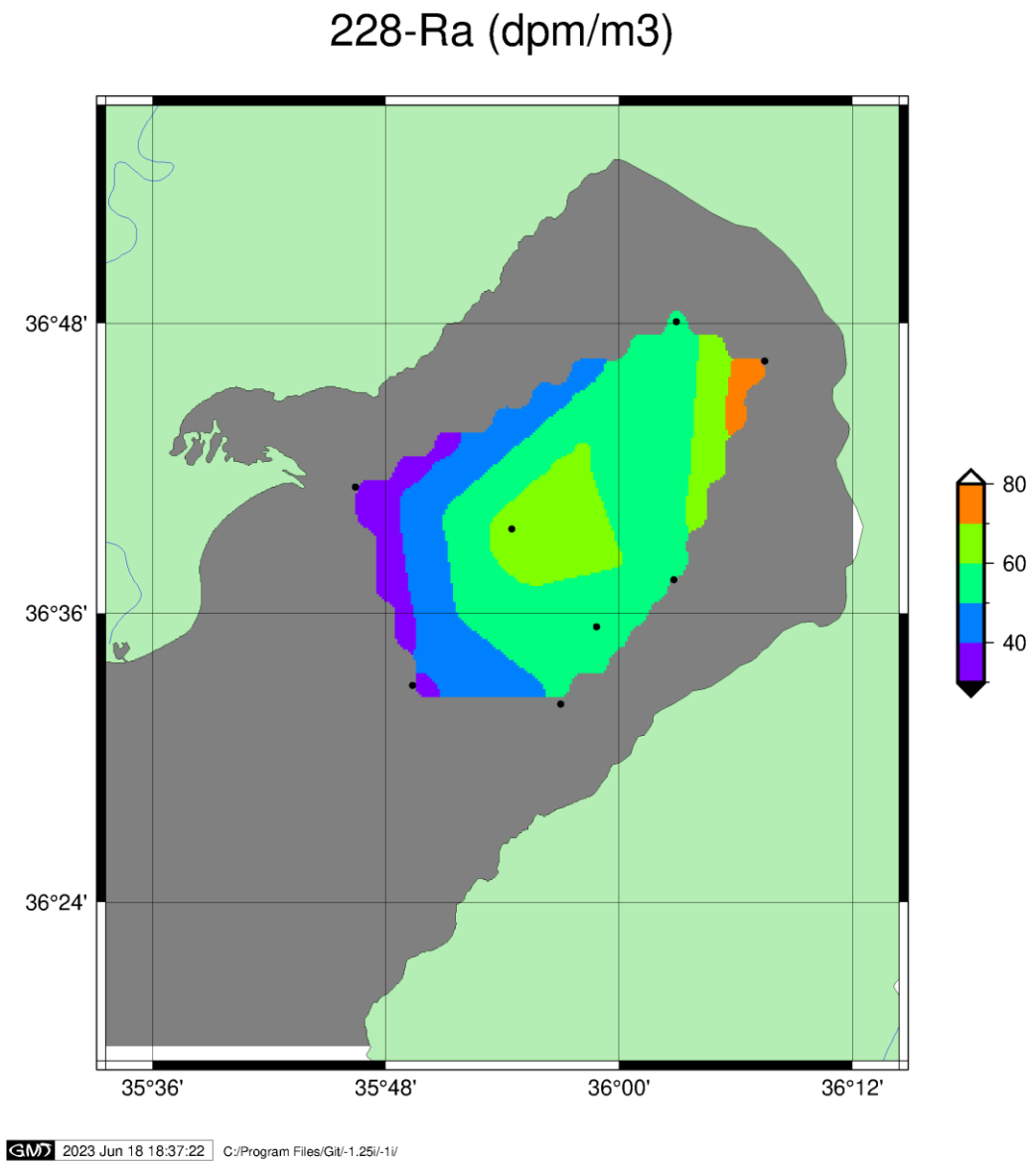

Figure 3.23. Interpolated ^{228}Ra activities of İskenderun Bay surface waters using triangulation method

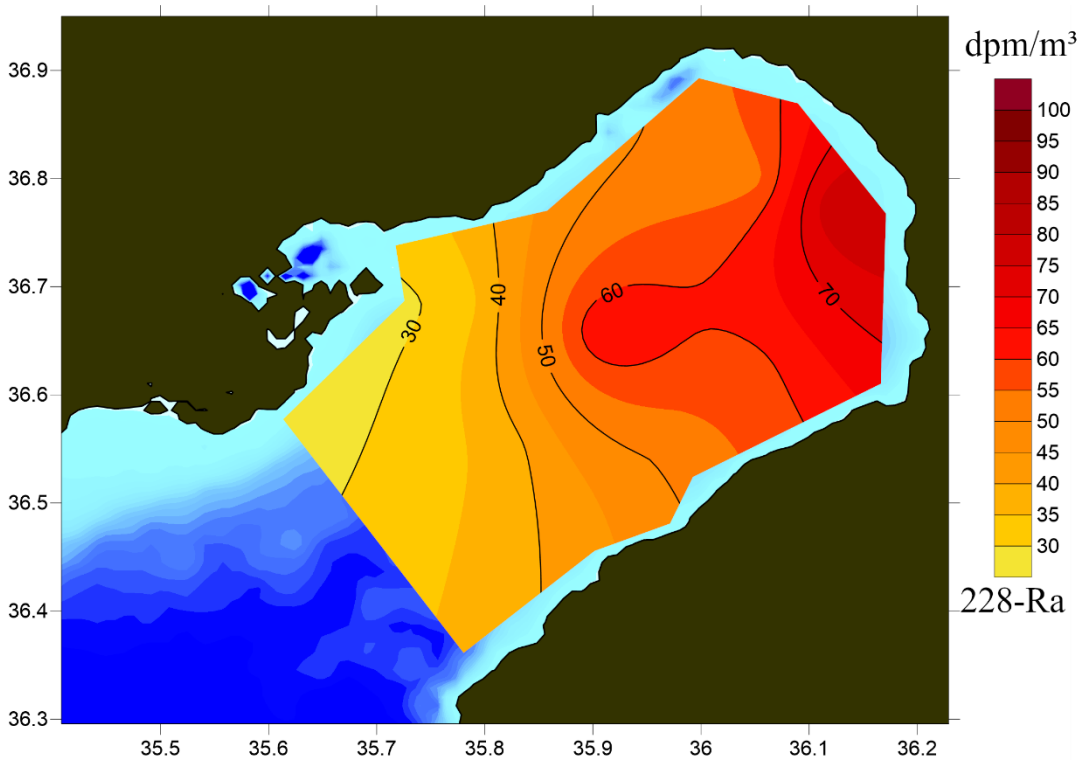

Figure 3.24. Extrapolated ^{228}Ra activities of İskenderun Bay surface waters using krigging method

3. 4. ^{228}Ra Inventories of the Cilician Basin and İskenderun Bay

The bathymetry data shows that the DL has approximately 4103.92 km³ of water mass, where SL and IL have 3507.64 km³ and 7033.02 km³, respectively. Multiplying the volume by the average activity of the layer calculated as 7.818 dpm/m³ excluding inflow stations St-002 and St-004, resulted that ^{228}Ra inventory of DL was ~3.21 x10^{13} dpm. The average and total activities were calculated separately for the SL and IL. SL had an average activity of 26.95 dpm/m³ where the IL had 22.07 dpm/m³. The computation revealed 9.45 x10^{13} dpm and 15.52 x10^{13} dpm inventories for the SL and IL, respectively, that add up to a total of ~24.97 x10^{13} dpm in the UL between 0-600 m depth.

^{228}Ra inventory of İskenderun Bay was found as 5.57 x 10^{12} dpm by multiplying the volume of 90.75 km³ and the average ^{228}Ra activity, 61.35 dpm/m³. The results

showed that the dry season İskenderun Bay inventory might have the 2.2% of the total ^{228}Ra inventory in the Cilician Basin's upper 600 m in the wet season.

3. 5. Submarine Groundwater Discharge and Associated Nutrient Fluxes

3. 5. 1. Mass-balance

3. 5. 1. 1. Sediment Diffusion, F_{sed}

The continental shelf area and slope area (between 400-600 m depth) were calculated as 9868.85 km² and 5543.56 km² using the method described in the **Chapter 2**. Moreover, the shelf area was divided into two according to grain size distribution as fine grained and coarse grained. The integrated data from Yemenicioglu & Tunc (2013) suggested that the average fine-grained sediment contributes 40% of the shelf. Multiplying these areas with the ^{228}Ra diffusion rates reported by (Moore et al., 2008) as 11 ± 5 x10³ dpm·m^{-2}·yr^{-1}, 230 ± 110 dpm·m^{-2}·yr^{-1}, 2.3 ± 1.1 dpm·m^{-2}·yr^{-1}, from fine-grained shelf sediments, coarse-grained shelf sediments, and slope sediments, respectively, resulted in 4.346 x10^{13}, 0.136 x10^{13}, and 1.275 x10^{13} dpm/yr of fluxes (Table 13).

Table 13. ^{228}Ra fluxes from sediments

	Flux, ($\cdot 10^{13}$) dpm/yr	Contribution, %
Fine-grained shelf sediments	4.346	75.49%
Coarse-grained shelf sediments	0.136	2.36%
Slope	1.275	22.15%
F_{sed}, TOTAL	5.757	100.00%

3. 5. 1. 2. River-borne ^{228}Ra fluxes, F_{riv}

Total suspended solid measurements revealed that average TSS concentrations of Berdan, Ceyhan, Göksu, and Seyhan rivers were 60 mg/L and 246.22 mg/L for the

dry and wet seasons, respectively. The total flux in the most recent available year (2014-2015), ~13.453 km³/yr, was used in order to have a conservative approach for estimating the SGD. The total annual TSS load was calculated to be 2059.79 kT.

River-borne ^{228}Ra fluxes, F_{riv}, include both the desorption from suspended particles and the activity in river water. Annual TSS load desorption and the desorption rate of 0.5 dpm/g sediment (Moore & Shaw, 2008; Ollivier et al., 2008; Rodellas et al., 2015) as described in the **Chapter 2** revealed that desorption may have contributed ~1.03 x10^{12} dpm/yr. On the other hand, the product of weighted-average ^{228}Ra activity in rivers and the annual flux showed that ~1.38 x10^{12} dpm/yr of input came from river fluxes. Therefore, total annual river-borne ^{228}Ra fluxes, F_{riv}, yields about 2.35 x10^{12} dpm per year.

3. 5. 1. 3. Atmospheric Deposition, F_{atm}

The atmospheric deposition input of ^{228}Ra was found to be ~1.13 x10^{12} dpm per year by extrapolating annual dust deposition of 20.25 g·m^{-2}·yr^{-1} reported by Ediger (2020) to the area of the Cilician Basin, ~27916.28 km².

3. 5. 1. 4. ^{228}Ra Loss by Radioactive Decay, F_{dec}

The total ^{228}Ra inventory estimated for the UL above with the decay term of ~0.12 yr^{-1} resulted in a ^{228}Ra sink of ~3.01 x10^{13} dpm/yr.

3. 5. 1. 5. Net Vertical Advection From/To the Deep Layer

As it is described in the Chapter 2, another ^{228}Ra mass-balance equation was established for the DL to estimate the advection rate (Eq. 4). From the equation [4], Q_{adv} (km³/yr) was calculated as ~1458.77 km³/yr. Then, the difference of $F_{adv_{in}}$ [Eq. 5] and $F_{adv_{out}}$ [Eq. 6] resulted in a net ^{228}Ra outflow of 0.39 x10^{13} dpm/yr caused by vertical advection.

3. 5. 1. 6. Net Offshore Water Exchange, $F_{net_{ex}}$

The offshore exchange rate, Q_{ex}, was calculated as 11484.6 km³/yr, by dividing the box's volume by the residence time defined in the **Chapter 2** as the amount of time a water parcel spends inside a body of water before departing through one of its boundaries. St-014, St-015, and St-016 were the outflow stations that represent the water mass flowing out of the basin directly through the western boundary. Table 14 indicates that the average ^{228}Ra activities were 35.37 dpm/m³, 19.78 dpm/m³, and 5.63 dpm/m³ for SL, IL, and DL, respectively. However, only the upper 600 m were in concern of the mass-balance. Therefore, the equation [4] was computed for only SL and IL, separately. The loss terms converged to ~2.943 x10^{14} dpm/yr and ~2.497 x10^{13} dpm/yr for SL and IL, respectively.

Table 14. Mean ^{228}Ra activities

Layer	Average Basin Activity, dpm/m³	Inflow Activity, dpm/m³	Outflow Activity, dpm/m³
0-150 m (SL)	26.95 (n=19)	24.44 (n=5)	35.37 (n=3)
150-600 m (IL)	22.07 (n=4)	18.28 (n=3)	25.54 (n=3)
>600 m (DL)	7.82 (n=5)	12.73 (n=2)	5.63 (n=2)

3. 5. 1. 7. ^{228}Ra Fluxes through Submarine Groundwater Discharge, F_{sgd}

The equation [1] revealed that F_{sgd} is the dominant net ^{228}Ra source in the basin with a rate of ~2.872 x10^{14} dpm/yr. It was almost 4 times higher than the second largest net input of ^{228}Ra, sediment diffusion. Offshore exchange brought more ^{228}Ra into

the basin, however overall it was the major sink term as it flushes out a greater amount of ^{228}Ra than any other component of the box model.

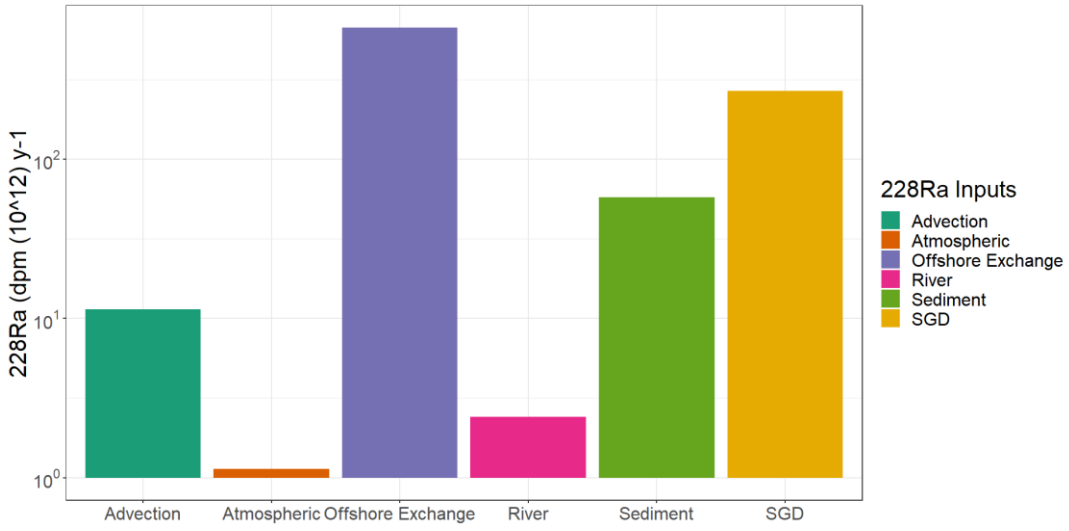

Figure 3.25. ^{228}Ra Sources of the Cilician Basin

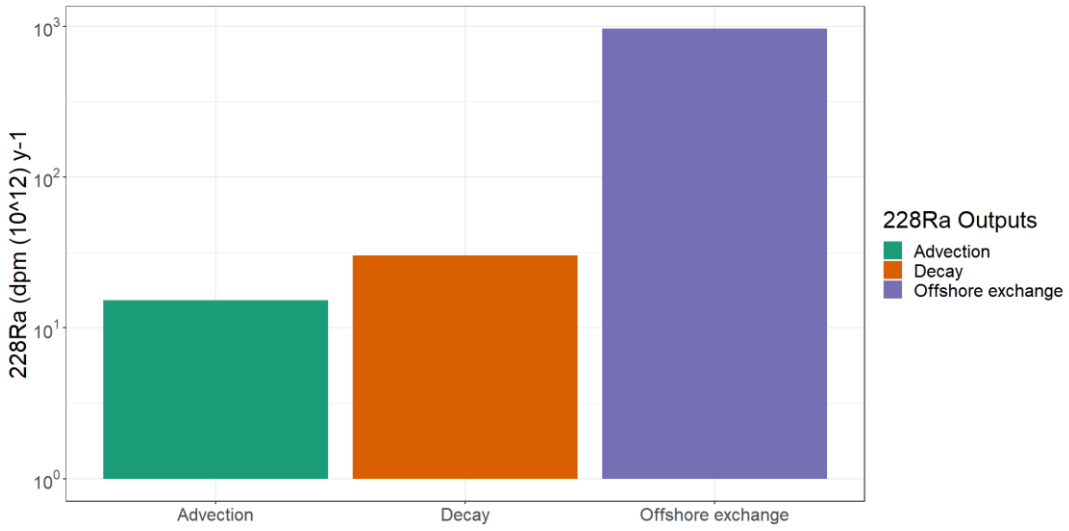

Figure 3.26. ^{228}Ra Sinks of the Cilician Basin

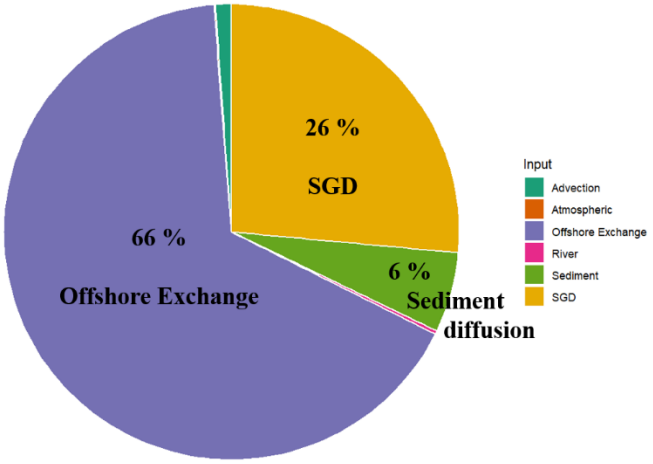

Figure 3.27. Contributions of ^{228}Ra inputs

3. 5. 2. Submarine Groundwater Discharge into the Cilician Basin

Table 15 provides the ranges of end-member activities used in order to calculate SGD rates. As it is described in the **Chapter 2**, F_{sgd} was divided by both the quartile ranges of this study and previously reported groundwater activities (Rodellas et al., 2015), separately.

Table 15. Groundwater end-member activity ranges

End-member activities	This study, dpm/m³	Rodellas et al., 2015, dpm/m³
Q1	63.08	640
Q3	116.32	2200

The results obtained and comparisons with total annual river discharge are set out in Table 16 below. Regardless of which range was selected, SGD rates were at least one order of magnitude higher than the river discharge.

Table 16. SGD rates in to the Cilician Basin, TARD: Total Annual River Discharge)

SGD rates	This study, km^3/yr	Using the range given by Rodellas et al., 2015, km^3/yr
Q1	2297 (x180 TARD)	121 (x10 TARD)
Q3	4236 (x332 TARD)	417 (x33 TARD)

The SGD rates were most sensitive to the residence time of the surface layer, except for the Ra activities. Halving the RT of SL would increase the SGD rate by 94%, while doubling it would yield a 47% decrease. The variation gets more dramatic with a further decrease in RT in contrast to the smoother variation obtained by a further increase (Figure 3.28).

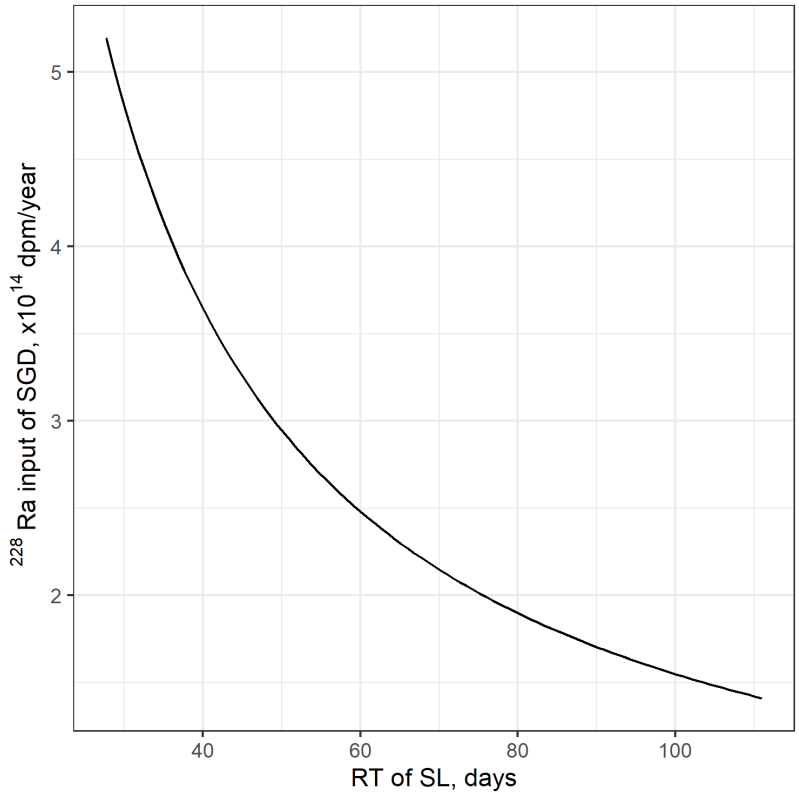

Figure 3.28. Variation in F_{sgd} with respect to the RT of SL

Considering the highest variation in RT of SL, between the wet and dry seasons of 2019 (24 and 74 days, respectively), approximately a three-fold change was presented in SGD rates. It yielded the SGD rates of 7 to 21 times of total annual riverine discharge in the area for dry and wet seasons in 2019, respectively, using the highest end-member activity, 2200 dpm/m^3, given in the Table 15.

3. 5. 3. SGD-associated Nutrient Fluxes

In order to calculate the net nutrient fluxes in a conservative manner, FSGD portion was estimated utilizing the median of minimum FSGD contents reported from ten sites by Bayari et al., (2011) as described in the **Chapter 2**. The median percentage was 12% which indicates at least 14.57 km^3 of annual FSGD into the basin which is ~14 % higher than the annual river discharge, using the minimum SGD rate estimated above (121 km^3/yr). Taking the median PO_4^{3-}, DIN, and Si concentrations of 0.60 μM, 184.89 μM, and 124.41 μM, the net nutrient loads associated with SGD were estimated at least 0.27, 37.73, 50.92 kT/yr, respectively. These values corresponded to 66%, 106%, and 96% of riverine PO4-P, DIN-N, and SiO_4-Si loads, respectively, calculated by using long-term averages of riverine discharge rates. Furthermore, DIN-N:PO_4-P was ~139, which is at least 1.6 times of what is found in rivers. The highest SGD rate estimated above (4236 km^3/yr) would account for 35 times larger nutrient fluxes, more than 23, 37, and 34 times riverine P-PO4, DIN-N, and SiO_4-Si loads, respectively.

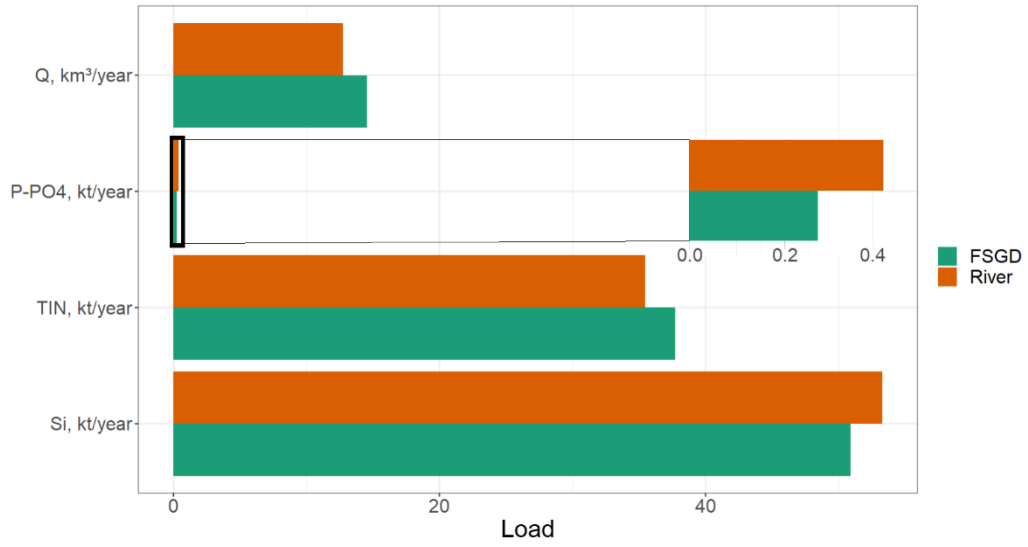

Figure 3.29. Annual minimum FSGD & Annual Riverine Discharge and Nutrient Loads Comparison in kT/yr

CHAPTER 4

DISCUSSION

4. 1. Physico-chemistry of the Basin and the Catchment

Salinity profiles collected in the Cilician Basin showed a typical pattern of "scorpion tail" with a salinity maximum between 150-250 m in the wet season and between 100-200 m in the dry season, which defines LIW. Subsurface oxygen maxima were also prevalent for both seasons, most likely owing to the strong ventilation during the winter, as it was also depicted in previous studies (Fach et al., 2021; Manca et al., 2004). Interestingly, surface temperatures were lower that what was observed 6 years ago, April 18 – 19, 2016 (Fach et al., 2021). It can be deduced that warming took place earlier in 2016, resulting in LIW being situated at a deeper part in this study. Additionally, salinity and DO values found in the coastal areas indicated that river discharges had a significant impact on these values. DO concentrations were consistently higher in the vicinity of river mouths that might be due to the high concentrations in river waters and aeration effect of the discharge.

İskenderun bay had the highest temperatures, although overall the salinity levels there were lower than at other sites, likely due to the fresh riverine water input to the bay. Asi, Ceyhan and Deliçay (Hatay) rivers are three of the main rivers in the catchment, and all three might have an influence on the salinity of the İskenderun Bay. Moreover, the minimum DO concentrations were found between the depths of 40 and 50 meters might have been the consequence of biological processes such as the respiration of organic matter produced in the upper photic zone. Ventilation and circulation dynamics could be other factors contributing to the lower oxygen concentrations, yet further study on metabolic regimes is needed to better understand these dynamics and their impacts on the bay's ecosystem.

High nutrient concentrations found in river and groundwater samples indicated a significant nutrient pollution that could be derived from the intense agricultural and industrial activities. Riverine inputs were estimated using both long-term averaged fluxes and 2014-2015 flux data which was the most recently recorded, and the total riverine flux was 5% higher in the recent year data than the long-term average (Table 6 & Table 7). The Deliçay (Hatay) River's annual discharge showed the largest shift, nearly doubled compared to the most recent data, likely due to variations in precipitation throughout the year. The highest concentrations found in Ceyhan (for DIN-N and SiO_4-Si) and in Asi River (for PO_4-P) indicated that İskenderun Bay might be prone to riverine nutrient pollution. The semi-enclosed structure of the bay also increases the potential for eutrophication events since the flushing of the bay waters is limited.

Göksu 1 groundwater had an extremely high concentration of PO_4^{3-}, approximately nine times higher than the second-highest, Dörtyol groundwater. This is most likely caused by a connection with the local sewage system in the area. The scent of the sample and the well observed during the fieldwork also strengthened the doubt of contamination. The highest DIN and Si concentrations were found in Dörtyol, which might have been sustained by excessive use of fertilizers and longer residence time of water in the aquifers as the area is not dominated by karst structures (Figure 2.3). Furthermore, the positive correlation between PO_4^{3-} and NH_4^+ might be due to organic matter breakdown, especially where higher organic matter levels persist through sewage connections. The negative correlation between DIN and PO_4^{3-} on the other hand, could arise from PO_4^{3-} depletion caused by enhanced biological activity with high concentrations of NO_3^-. Complex biological dynamics in aquifers might have led to these correlations; therefore, investigating environmental conditions and microbial interactions can be useful in the future to have a more precise understanding of these dynamics.

4. 2. Residence Time

The residence time of the Cilician Basin was estimated for the first time, which can be a major factor controlling eutrophication dynamics (Defne & Ganju, 2015). According to hydrodynamic product results, this value averaged out at approximately 172 days but varied depending on certain factors as circulation dynamics. Specifically, temporal changes responsible for fluctuations appear linked to variations within both Latakia Eddy (Robinson et al., 1991) & mesoscale eddy patterns (Fach et al., 2021). In addition, the eddies formed by northward currents along the eastern coasts (coasts of Lebanon Syria) may have an influence on the variations as they may avert the Atlantic waters carried by the Mid-Mediterranean Jet, and feed the Cilician current (Alhammoud et al., 2005).

This disparity in observations pointed out earlier directly relates to how accurately Particle Tracking Methods account for particulars such as ingress, egress, and re-entry until final exit. It's important to mention that this distinctive process comes up through the consideration of a phenomenon named return flow (Savatier & Rocha, 2021).

Particle tracking results also indicated considerable fluctuations occurring seasonally and inter-annually, especially in the first 400 meters depth. Since this model is operated to a depth of 600 meters, caution is advisable when comparing the results with the first method results. Nevertheless, the 345-day mean value found is considerably higher than those calculated analytically with the flow data. The disparity is attributed to the particle tracking method that calculated the particles entering and leaving the basin and then re-enter until the last exit date, which can be explained by the return flow term (Savatier & Rocha, 2021). Furthermore, the seasonal and inter-annual variations can be associated with the reasons explained above. Lower residence times estimated in the wet season indicated a more rapid circulation, which is most probably related to atmospheric variability considering wind-driven circulation in the basin. As a result, higher seasonal differences with more contrasting meteorological conditions can be expected. Long-term monitoring

of hydrological, meteorological, and oceanographic data is required for any statistical data to be presented and correlated with variables.

The ARGO float's residence time in the basin was also consistent with the particle tracking results, considering it entered the basin in December 2015 and left in January 2016. Rapid circulation at that time of the year may have led the float to reside in the basin for only 31 days, where the average residence time of the surface layer was estimated as 37 days and 27 days for December and January, respectively, using the particle tracking method.

Although residence time estimation of open water bodies is not always straightforward (Moore et al., 2006; Savatier & Rocha, 2021), residence time calculations are crucial for determining the ^{228}Ra inventory and, ultimately, the SGD discharge in the basin. Variability in both time and space must be considered. Although these results need to be interpreted with caution due to the caveats stated below (4.1. Caveats and Limitations), the residence time of the Cilician Basin is estimated for the first time here, and the results revealed that it is the major loss term of ^{228}Ra. The residence time may also be employed as well to establish comparable box models in the area for interpreting mixing dynamics, which might be essential for both biogeochemical and circulation dynamics.

4. 3. Radium Activities

Overall, the average ^{228}Ra activities found in the basin (27 dpm/m³ for SL, and 22 dpm/m³ for IL) were generally consistent with what was previously reported in Levantine Sea waters (28 ± 2 dpm/m³ for SL, and 27 ± 2 dpm/m³ for IL) (Rodellas et al., 2015). The increasing activities through depth until 150 m might be caused by higher ^{228}Ra input until 150 m and rapid circulation in the surface waters. Rapid surface water circulation might have contributed to the increased activity at higher depths up to 150 m.

All groundwater activities were below 300 dpm/m³, with the Göksu delta having the maximum activity with 257.73 dpm/m³. The higher activity found in Göksu might have been caused by longer residence time of water in aquifers or saline water intrusion. However, all the groundwater samples were fresh at the time of sampling. Hence, the increase in ^{228}Ra could be attributed to any contamination as previously noted. ^{228}Ra activities were generally lower than previously reported ones as the quartile range was presented as 640-2200 dpm/m³ (Rodellas et al., 2015 and references therein) for the Mediterranean sea. The significantly lower activities can be attributed to two main reasons. First, all groundwater samples were freshwater (Specific conductivity<3500 µS/cm) (Table 1), as higher activities can be expected with salinity due to the higher ionic strength in saline waters lead radium to desorb (Moore, 2003; Paytan et al., 2006). Second, the karstic geology of the area can cause very low activities due to rapid flow of groundwater in cracks and fractures, which does not provide the necessary time for radium to enrich in the groundwater (Parise et al., 2018). Another potential reason could be the inefficiency of Mn-fibers due to the potential anoxic conditions in groundwater (Vinson et al., 2013). However, an additional survey conducted in April 2023 revealed that the measured DO levels together with the high nitrate concentrations do not allow for escaping Ra isotopes from Mn-fibers (Table 3) as the existence of dissolved oxygen or nitrate creates thermodynamically steady circumstances for solid-phase metal oxides, which facilitate the extraction of Ra from groundwater (Vinson et al., 2013).

Dissolved ^{228}Ra activities in rivers exhibited a range between 41 and 175 dpm/m³ (n = 8), where only a single sample (Lamas River) demonstrated an activity below 80 dpm/m³. The potential reasons of lowest activity found in Lamas River can be speculated as high adsorption and sedimentation rates. To fully understand the processes underlying this low activity, additional research is required. These results agreed well with the previously reported activities in the Mediterranean rivers that had a range of 80-180 dpm/m³ (Garcia-Solsona et al., 2008; Ollivier et al., 2008; Rapaglia et al., 2010; Rodellas et al., 2015 and references therein). However, TSS measurements revealed that, the average riverine suspended particle inputs were

significantly lower than the prevailing assumption for the entire Mediterranean (Rodellas et al., 2015). However, the current TSS measurements include only regular flow and are not representative of extreme flow and flooding TSS loads, thus probably underestimating annual average TSS loads. In addition, another study in the region showed significantly lower concentrations than the Mediterranean Sea assumption (Ediger, 2020). Low discharge rates, increasing number of dams in the catchment, geologic, and geomorphic factors might be the reasons of low suspended matters measured (Hoos et al., 2000; Sow et al., 2016; Vasylenko et al., 2018; Wildhaber, 2013).

Elevated activities found in the outflow provides evidence for an overall ^{228}Ra enrichment within the basin. The ^{228}Ra enrichment zones (>30 dpm/m^3) might be explained by the coastal submarine groundwater discharge distribution along the coast (Luijendijk et al., 2020) (Figure 4.1).

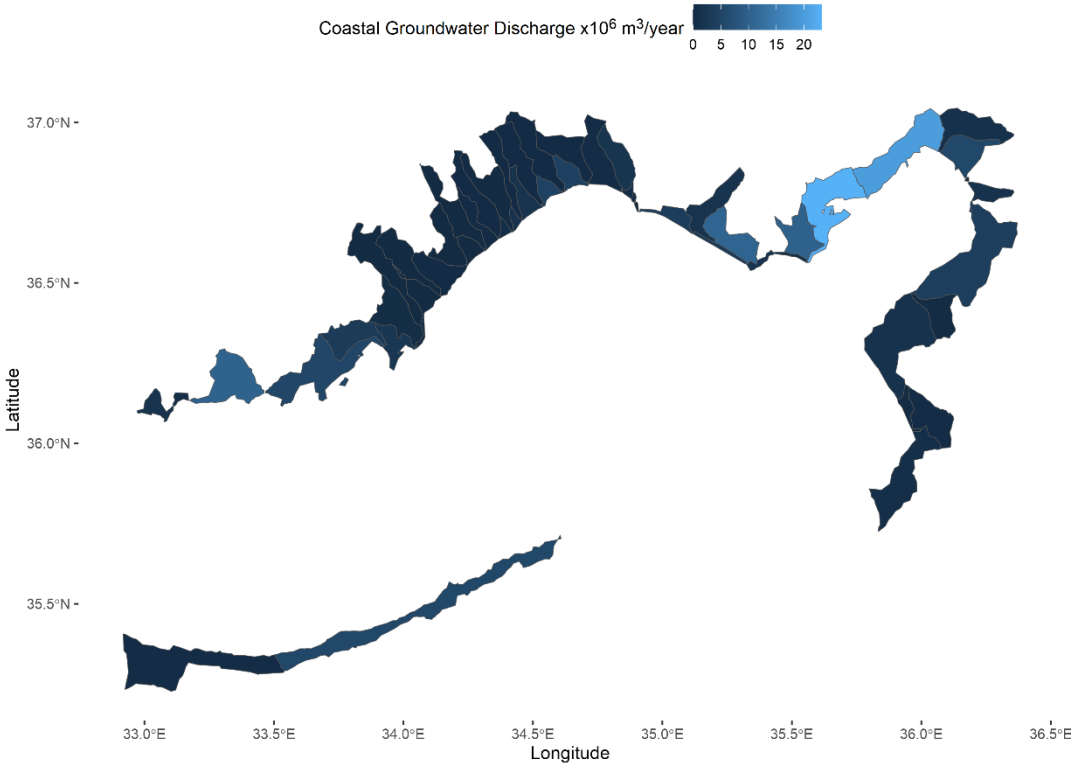

Figure 4.1. Coastal Groundwater Discharge rates according to Luijendijk et al. (2020)

The significant difference between AR values of seawater and catchment samples may imply that the residence time, hence inflowing water, and other Radium sources such as sediment diffusion had an impact on overall Radium inventory in the basin (Moore, 2015). Moreover, there were notable variations between AR's of each layer in basin. It can provide information about different water masses and their movements in the basin (Krest & Moore, 1999; Mears et al., 2020). Further investigation is needed to have more insight about distinguishing water masses and their flow patterns using AR. Yet, observed ratios were consistent with the residence times of the layers as the lowest residence time had the highest AR (Surface Layer), where the maximum residence times were estimated at the deep layer which had the minimum AR.

^{228}Ra inventory calculations revealed that upper 600 meters of the Cilician Basin had approximately 3.4% of the upper 600 m inventories of the Levantine Basin (Rodellas et al., 2015). Considering the water volumes, 2.28 x 10^{15} m³ (Rodellas et al., 2015) for the Levantine Basin and 1.05 x 10^{14} m³ for the Cilician Basin (~4.6% of the Levantine Basin), the activities in the Cilician Basin were lower than what might have been anticipated from these volumes. Presumably, the heterogeneous nature of radium sources and circulation patterns are the main drivers of the uneven distribution of ^{228}Ra in the Levantine basin.

Generally, İskenderun Bay had elevated ^{228}Ra activities. One of the potential drivers of the enrichment in the bay might be the high activities found in Deliçay (Hatay) river. St-018, the closest station to the Deliçay (Hatay) River, had the maximum activity in the bay (Table 11), which further supported the argument. The bay's catchment geology is not dominated by karst structures (undivided quaternary deposits and peridotite were dominant) in contrast to the remaining catchment of the Cilician Basin (Figure 2.3) (General Directorate of Mineral Research and Exploration, Türkiye, 2002). Correspondingly, infiltration rates can be lower than what is expected in karst, and the longer residence times in aquifers might lead to an increase in Ra activities in the submarine groundwater. Furthermore, the enrichment

in the İskenderun Bay has been anticipated as the bay's semi enclosed structure limits the offshore seawater exchange.

4. 4. Submarine Groundwater Discharge and Associated Nutrient Fluxes

SGD rates were higher than riverine discharges, even though the mass-balance was established with a conservative approach by using the higher quartile end-member activity, and it resulted in at least 10 times larger discharge rates than riverine discharges. The estimation yielded shore normalized rate of 152 x 10^6 $m^3.km^{-1}.y^{-1}$, which is comparable with the upper end of the range estimated for the Mediterranean Sea (6 x 10^6 to 100 x 10^6 $m^3.km^{-1}.y^{-1}$) (Rodellas et al., 2015), and the lower end of range estimated for the Atlantic Ocean (230 x 10^6 to 470 x 10^6 $m^3.km^{-1}.y^{-1}$) (Moore et al., 2008). The area normalized SGD rate (4350 x 10^3 $m^3.km^{-2}.y^{-1}$) was higher than the predicted ranges of the Mediterranean Sea (110 x 10^3 to 1900 x 10^3 $m^3.km^{-2}.y^{-1}$) (Rodellas et al., 2015) and the Atlantic Ocean (200 x 10^3 to 410 x 10^3 $m^3.km^{-2}.y^{-1}$) (Moore et al., 2008) that is most likely a consequence of using wet season ^{228}Ra end-member and seawater activities (see. 4.5). Furthermore, the DIN-N, PO_4-P, and SiO_4-Si annual loads associated with SGD were 9%, 44%, and 18% of DIN-N, DIP-P, and DIS-Si annual loads estimated for the Mediterranean Sea (Rodellas et al., 2015), respectively. Estimated shore-normalized loads were significantly higher in the Cilician Basin than what were reported for the Mediterranean Sea (Rodellas et al., 2015) by factors of 7, 35, and 15 for the DIN-N, PO_4-P, and SiO_4-Si, respectively. This comparison further implies that SGD-associated nutrient fluxes may have a huge impact on the nutrient budget of the Cilician Basin.

The mass-balance approach revealed that the largest net ^{228}Ra contributor was SGD (Figure 3.25 & 3.26). F_{sed} was the second largest net source of ^{228}Ra and contributed approximately 23% of F_{sgd}. The dominant fine-grained shelf sediment composition was the main factor that led to high ^{228}Ra inputs through sediment diffusion (Table 13). The lower ^{228}Ra contribution of rivers can be attributed the low levels of TSS.

These results demonstrated that SGD may have a huge impact on water budget in the Cilician Basin. Along with the discharge rates, it might be deduced that SGD is one of the critical processes for any material transport in to the basin. The PO_4^{3-}, DIN, and Si contribution by solely FSGD were calculated to obtain net nutrient fluxes driven by SGD. The findings highlighted that SGD associated nutrient fluxes might have a substantial influence on nutrient budget of the basin. The large DIN-N:PO_4-P ratios found to be supplied by SGD support the hypothesis that SGD contributes to the severe P limitation in the area, in addition to the high ratios of atmospheric input (Koçak et al., 2010). In fact, this might cause changes in phytoplankton community and interactions between trophic levels by reducing carbon uptake and fluxes between trophic levels or generating different phenotypes for phytoplankton through variations in epigenetic regulations and gene expression (Cabrerizo et al., 2022; Lin, 2023). Correspondingly, SGD can have an impact on primary production. Although very high DIN:PO_4^{3-} ratios (Table 8), there is also a significant amount of PO_4^{3-} transported to the basin which can lead to an increase in the primary production and may cause coastal eutrophication, especially in shallow sub-basins such as İskenderun Bay, where the SGD-associated nutrient fluxes can directly enter the euphotic zone. Assuming the median value of minimum FSGD contributions and selecting the highest end-member ^{228}Ra activity in the given range (Table 15) yielded 0.27 kT of SGD-driven PO_4^{3-} annual load. While selecting this approach enabled a more conservative SGD estimation, the karst-dominant geology and measured activities in the catchment raise the possibility of larger SGD rates and associated nutrient fluxes.

Moreover, temporal variations might be the key element to understand occasional coastal eutrophication in the basin as extreme SGD rates can lead to episodic nutrient enrichment (Diego-Feliu et al., 2022).

The conservative approach by taking the literature end-member activities into account resulted in an imprecise span (131—4553 km^3/yr of SGD) as no saline groundwater was sampled during the study. Future work is needed to obtain saline

end-member activities that enable more precise estimations by having precise values for end-member activities and FSGD content.

4. 5. Caveats and Limitations

The large range of end-member activity that arose from the lack of saline end-members has led to a wide span of SGD rates. Furthermore, the annual estimation made by using wet season activities and high temporal variability in the residence time further increased the uncertainty in the estimations. The maximum estimated SGD rate was substantially higher than the riverine discharge by a factor of 332, which may not be realistic. Therefore, caution is advised when using these rates, and future work is suggested to obtain more precise and accurate results, although this study showed that the SGD and associated nutrient input might have a crucial role in the water and nutrient budgets in the Cilician Basin for the first time.

The particle tracking model used in this study does not have vertical fluxes and particles are not allowed to move vertically. Therefore, the estimated residence times should not be regarded as general values for the region, and furthermore, cannot be representative of coastal areas. Case specific analysis for each sub-region is required. In the future, a 3D hydrodynamic model may be used to calculate the resident time in the sub-basin scale so that the impact of vertical motions can be considered.

There might be significant variability in the SGD rates and associated nutrient fluxes considering that the seasonal variation only in the calculated RT values accounts for a significant change in SGD rates, therefore, mass-balance approaches must be considered tentatively when extrapolating the results temporally. ^{228}Ra activities constrained through a year using the snapshot results can lead to uncertainties in SGD rate estimations as there might be significant temporal variations in the activities and the residence time (Tamborski et al., 2020).

Measurements of Ra activities were carried out at LSU and TARLA simultaneously because of the logistics. Although the detector in TARLA was calibrated with a

standard material and necessary background measurements were carried out, the fact that the detectors were not inter-calibrated makes it impractical to compare the measured activities of different detectors. Accordingly, only the activities measured at LSU were used in SGD estimations. These samples included only the wet season samples, therefore SGD rates might be overestimated in the study. Although approximately two-hundred-and-eighty Ra samples were taken, only thirty-eight seawater, fifteen catchment samples were analyzed to use in the mass balance within the scope of this study. Future work including the other samples may allow more precise and accurate estimations as well as the inclusion of future saline end-member activities. Similarly, nutrient loads associated with the SGD would vary with more precise SGD estimations. Moreover, TN and TP analysis that will be conducted in the future may enhance the comprehension of the nutrient loads and their impacts on the ecosystem, in addition to the verification of nutrient analysis.

There are inherent uncertainties emerging from the methodology in addition to the temporal heterogeneity, such as the assumption of steady-state for the ^{228}Ra mass balance. Nevertheless, because the spatial scale is large and radium is not prone to gas exchange, it is unlikely that it resulted in a significant error (Rodellas et al., 2021). On the contrary, lacking any saline end-member might result in remarkable overestimation in SGD rates. In order to overcome these issues, a large range of end-member activity were used as a conservative approach.

CHAPTER 5

CONCLUSION

The Cilician Basin is a peculiar marine environment as a formation place for the LIW (Fach et al., 2021; Özsoy et al., 1993; Sur et al., 1992) and with a karst-dominant catchment (General Directorate of Mineral Research and Exploration, Türkiye, 2002), playing a crucial role in the variability of water masses and circulation dynamics in the Mediterranean Sea. Despite the oligotrophic nature of the Eastern Mediterranean waters (Béthoux et al., 1998; Krom et al., 2004), increasing industrial and agricultural activities along its coast expose the basin to a serious eutrophication threat. In fact, eutrophication takes place especially where the circulation is limited (i.e., İskenderun Bay, Mersin Bay) (I. Akçay et al., 2018; Yilmaz et al., 1992). Therefore, the ecosystem health is in great danger and there is an urgent need to define and monitor nutrient sources to the basin that will allow efficient ecosystem management (Ali et al., 2022).

SGD has been shown to be a major component of both the global and the Mediterranean Sea nutrient budgets (Kwon et al., 2014; Rodellas et al., 2015). The study hypothesized that SGD might contribute to the water and nutrient budgets of the Cilician Basin significantly. The objectives of the study were identified as follows: first, to estimate the residence time of the Cilician Basin and quantify the water exchange rate between the open sea and the basin; second, to establish ^{228}Ra inventories of the Cilician Basin and İskenderun Bay; third, to assess the SGD rates by utilizing ^{228}Ra mass balance, assuming a steady-state condition; and fourth, to estimate the nutrient flows associated with the groundwater discharge and evaluate their potential effects on primary production. This study revealed the SGD rates and associated nutrient fluxes into the Cilician Basin for the first time, and filled the gap in the literature that had overlooked the SGD and associated nutrient fluxes into the basin so far. Moreover, the residence time of the basin was estimated for the first

time, which can be an essential element in any future box model studies as it represents the offshore water exchange rate (Garcia-Orellana et al., 2021). ^{228}Ra mass balance approach was utilized by establishing a box model. Defining each source and sink in the balance equation provided SGD related ^{228}Ra fluxes as the residual of the equation. The activities were measured by gamma-spectrometry for the samples collected through a basin-wide cruise in April 2022 and a catchment survey conducted in March 2022. The measurements yielded approximately 24.97 x 10^{13} dpm ^{228}Ra inventory in the defined box, and the inventory of İskenderun bay was found as 5.57 x 10^{12} dpm. Furthermore, the residence time of the basin using numerical modeling was reported for the first time, indicating a rapid circulation through the surface layer with a high temporal variability. Assuming a large range of end-member activity including also the available literature data yielded at least 121 km³ of annual discharge, while the maximum rate was estimated as 4236 km³/yr. SGD rates were most sensitive to the residence time of the surface layer except for the Ra activities as the maximum seasonal variation in residence time of the surface layer, 24 days in the wet season and 74 days in the dry season, corresponded approximately threefold change in SGD rate. Consequently, calculating SGD rates taking the variability into account is advisable for more accurate estimates.

These results indicated that SGD might have had a substantial role in the nutrient budget of the basin, even in the most conservative scenario, where the loads corresponded to 66%, 106%, and 96% of riverine PO_4-P, DIN-N, and SiO_4-Si loads. Moreover, the high DIN:PO_4^{3-} ratio, 139, suggested that SGD might be the major driver of observed phosphorus limitation in the area (Krom et al., 2010). Therefore, it might have a potential influence on primary production by altering phytoplankton community structure and dynamics between trophic levels (Cabrerizo et al., 2022; Lin, 2023). Nonetheless, further investigation is needed to better estimate the SGD related fluxes to the basin and understand the effects of SGD on the marine ecosystem.

REFERENCES

Akçay, İ. (2015). Spatial variations of Particulate Organic Matter (POM) composition and concentrations in surface waters and sediments of the Mersin Bay [M.Sc.]. Institute of Marine Sciences, Midde East Technical Universiy.

Akçay, I., Tugrul, S., & Uysal, Z. (2018). Biochemical quality elements for the assessment of eutrophication in Mersin & Iskenderun Bays (northeastern Mediterranean). International Marine & Freshwater Sciences Symposium Proceedings (MARFRESH2018).

Alhammoud, B., Béranger, K., Mortier, L., Crépon, M., & Dekeyser, I. (2005). Surface circulation of the Levantine Basin: Comparison of model results with observations. Progress in Oceanography, 66(2–4), 299–320. https://doi.org/10.1016/j.pocean.2004.07.015

Ali, E., W. Cramer, J. Carnicer, E. Georgopoulou, N.J.M. Hilmi, G. Le Cozannet, and P. Lionello, 2022: Cross-Chapter Paper 4: Mediterranean Region. In: Climate Change 2022: Impacts, Adaptation and Vulnerability. Contribution of Working Group II to the Sixth Assessment Report of the Intergovernmental Panel on Climate Change [H.-O. Pörtner, D.C. Roberts, M. Tignor, E.S. Poloczanska, K. Mintenbeck, A. Alegría, M. Craig, S. Langsdorf, S. Löschke, V. Möller, A. Okem, B. Rama (eds.)]. Cambridge University Press, Cambridge, UK and New York, NY, USA, pp. 2233–2272, doi:10.1017/9781009325844.021

Anderson, B. A., Maslia, M. L., Caparoso, J. L., Ausdemore, D., & Aral, M. M. (2010). Stochastic Analysis of Pesticide Transport in the Shallow Groundwater of Oatland Island, Georgia, USA. Water Quality, Exposure and Health, 2(1), 47–64. https://doi.org/10.1007/s12403-010-0023-6

Anderson, D. M., Glibert, P. M., & Burkholder, J. M. (2002). Harmful algal blooms and eutrophication: Nutrient sources, composition, and consequences. Estuaries, 25(4), 704–726. https://doi.org/10.1007/BF02804901

Bakalowicz, M. (2015). Karst and karst groundwater resources in the Mediterranean. Environmental Earth Sciences, 74(1), 5–14. https://doi.org/10.1007/s12665-015-4239-4

Barth, A., Beckers, J.-M., Troupin, C., Alvera-Azcárate, A., & Vandenbulcke, L. (2014). divand-1.0: N-dimensional variational data analysis for ocean observations. Geoscientific Model Development, 7(1), 225–241. https://doi.org/10.5194/gmd-7-225-2014

Bayari, C. S., Ozyurt, N. N., Oztan, M., Bastanlar, Y., Varinlioglu, G., Koyuncu, H., Ulkenli, H., & Hamarat, S. (2011). Submarine and coastal karstic groundwater discharges along the southwestern Mediterranean coast of Turkey. Hydrogeology Journal, 19(2), 399–414. https://doi.org/10.1007/s10040-010-0677-y

Ben-Shachar, M. S., Lüdecke, D., & Makowski, D. (2020). effectsize: Estimation of Effect Size Indices and Standardized Parameters. Journal of Open Source Software, 5(56), 2815. https://doi.org/10.21105/joss.02815

Béthoux, J. P., Morin, P., Chaumery, C., Connan, O., Gentili, B., & Ruiz-Pino, D. (1998). Nutrients in the Mediterranean Sea, mass balance and statistical analysis of concentrations with respect to environmental change. Marine Chemistry, 63(1–2), 155–169. https://doi.org/10.1016/S0304-4203(98)00059-0

Beusen, A. H. W., Slomp, C. P., & Bouwman, A. F. (2013). Global land–ocean linkage: Direct inputs of nitrogen to coastal waters via submarine groundwater discharge. Environmental Research Letters, 8(3), 034035. https://doi.org/10.1088/1748-9326/8/3/034035

Burnett, W. C., Aggarwal, P. K., Aureli, A., Bokuniewicz, H., Cable, J. E., Charette, M. A., Kontar, E., Krupa, S., Kulkarni, K. M., Loveless, A., Moore, W. S., Oberdorfer, J. A., Oliveira, J., Ozyurt, N., Povinec, P., Privitera, A. M. G., Rajar, R., Ramessur, R. T., Scholten, J., … Turner, J. V. (2006). Quantifying submarine groundwater discharge in the coastal zone via multiple methods. Science of The Total Environment, 367(2–3), 498–543. https://doi.org/10.1016/j.scitotenv.2006.05.009

Burnett, W. C., Bokuniewicz, H., Moore, W. S., & Taniguchi, M. (2003). Groundwater and pore water inputs to the coastal zone. Biogeochemistry, 66, 3–33.

Cabrerizo, M. J., Medina-Sánchez, J. M., González-Olalla, J. M., Sánchez-Gómez, D., & Carrillo, P. (2022). Microbial plankton responses to multiple environmental drivers in marine ecosystems with different phosphorus

limitation degrees. Science of The Total Environment, 816, 151491. https://doi.org/10.1016/j.scitotenv.2021.151491

Cardenas, M. B., Rodolfo, R. S., Lapus, M. R., Cabria, H. B., Fullon, J., Gojunco, G. R., Breecker, D. O., Cantarero, D. M., Evaristo, J., Siringan, F. P., & Zhang, T. (2020). Submarine Groundwater and Vent Discharge in a Volcanic Area Associated With Coastal Acidification. Geophysical Research Letters, 47(1), 1–9. https://doi.org/10.1029/2019GL085730

Caspers, H. (1970). J. D. H. Strickland and T. R. Parsons: A Practical Handbook of Seawater Analysis. Ottawa: Fisheries Research Board of Canada, Bulletin 167, 1968. 293 pp. $ 7.50. Internationale Revue Der Gesamten Hydrobiologie Und Hydrographie, 55(1), 167–167. https://doi.org/10.1002/iroh.19700550118

Charette, M. A., Dulaiova, H., Gonneea, M. E., Henderson, P. B., Moore, W. S., Scholten, J. C., & Pham, M. K. (2012). GEOTRACES radium isotopes interlaboratory comparison experiment: Radium Intercomparison. Limnology and Oceanography: Methods, 10(6), 451–463. https://doi.org/10.4319/lom.2012.10.451

Chen, L., & Xu, J. (2004). OPTIMAL DELAUNAY TRIANGULATIONS. Journal of Computational Mathematics, 22(2), 299–308. JSTOR.

De Weys, J., Santos, I. R., & Eyre, B. D. (2011). Linking groundwater discharge to severe estuarine acidification during a flood in a modified wetland. Environmental Science and Technology, 45(8), 3310–3316. https://doi.org/10.1021/es104071r

Defne, Z., & Ganju, N. K. (2015). Quantifying the Residence Time and Flushing Characteristics of a Shallow, Back-Barrier Estuary: Application of Hydrodynamic and Particle Tracking Models. Estuaries and Coasts, 38(5), 1719–1734. https://doi.org/10.1007/s12237-014-9885-3

Delandmeter, P., & van Sebille, E. (2019). The Parcels v2.0 Lagrangian framework: New field interpolation schemes. Geoscientific Model Development, 12(8), 3571–3584. https://doi.org/10.5194/gmd-12-3571-2019

Demirel, Z., & Güler, C. (2006). Hydrogeochemical evolution of groundwater in a Mediterranean coastal aquifer, Mersin-Erdemli basin (Turkey). Environmental Geology, 49(3), 477–487. https://doi.org/10.1007/s00254-005-0114-z

Diego-Feliu, M., Rodellas, V., Alorda-Kleinglass, A., Saaltink, M., Folch, A., & Garcia-Orellana, J. (2022). Extreme precipitation events induce high fluxes of groundwater and associated nutrients to coastal ocean. Hydrology and Earth System Sciences, 26(18), 4619–4635. https://doi.org/10.5194/hess-26-4619-2022

Dulaiova, H., & Burnett, W. C. (2004). An efficient method for γ-spectrometric determination of radium-226,228 via manganese fibers: Radium determination by manganese fiber. Limnology and Oceanography: Methods, 2(8), 256–261. https://doi.org/10.4319/lom.2004.2.256

Ediger, V. (2020). Grain size distributions in airborne dust, river-suspended loads, and marine sediments from southeastern Turkey (NE Mediterranean Sea).

TURKISH JOURNAL OF EARTH SCIENCES, 29(6), 1033–1047. https://doi.org/10.3906/yer-2002-19

E.U. Copernicus Marine Service Information (CMEMS). (n.d.). Mediterranean Sea Physics Reanalysis [dataset]. Marine Data Store (MDS). https://doi.org/10.25423/CMCC/MEDSEA_MULTIYEAR_PHY_006_004_E3R1

Fach, B. A., Orek, H., Yilmaz, E., Tezcan, D., Salihoglu, I., Salihoglu, B., & Latif, M. A. (2021). Water Mass Variability and Levantine Intermediate Water Formation in the Eastern Mediterranean Between 2015 and 2017. Journal of Geophysical Research: Oceans, 126(2). https://doi.org/10.1029/2020JC016472

Fan, C., Wang, G. S., Chen, Y. C., & Ko, C. H. (2009). Risk assessment of exposure to volatile organic compounds in groundwater in Taiwan. Science of The Total Environment, 407(7), 2165–2174. https://doi.org/10.1016/J.SCITOTENV.2008.12.015

Fitts, C. R. (2013). Groundwater: The Big Picture. Groundwater Science, 1–22. https://doi.org/10.1016/B978-0-12-384705-8.00001-7

Garcia-Orellana, J., Rodellas, V., Tamborski, J., Diego-Feliu, M., van Beek, P., Weinstein, Y., Charette, M., Alorda-Kleinglass, A., Michael, H. A., Stieglitz, T., & Scholten, J. (2021). Radium isotopes as submarine groundwater discharge (SGD) tracers: Review and recommendations. Earth-Science Reviews, 103681. https://doi.org/10.1016/j.earscirev.2021.103681

Garcia-Solsona, E., Masqué, P., Garcia-Orellana, J., Rapaglia, J., Beck, A. J., Cochran, J. K., Bokuniewicz, H. J., Zaggia, L., & Collavini, F. (2008). Estimating submarine groundwater discharge around Isola La Cura, northern Venice Lagoon (Italy), by using the radium quartet. Marine Chemistry, 109(3–4), 292–306. https://doi.org/10.1016/j.marchem.2008.02.007

General Directorate of Mineral Research and Exploration, Türkiye. (2002). GEOLOGICAL MAP OF TURKEY [Map]. General Command of Mapping, Türkiye.

General Directorate of State Hydraulic Works, Türkiye. (2018). 2015 AKIM GÖZLEM YILLIĞI. DSİ Teknoloji Dairesi Başkanlığı Basım ve Foto-Film Şube Müdürlüğü.

George, C., Moore, W. S., White, S. M., Smoak, E., Joye, S. B., Leier, A., & Wilson, A. M. (2020). A New Mechanism for Submarine Groundwater Discharge From Continental Shelves. Water Resources Research, 56(11), 1–17. https://doi.org/10.1029/2019WR026866

Grasshoff, K., Kremling, K., & Ehrhardt, M. (2007). Methods of Seawater Analysis: Third, Completely Revised and Extended Edition (3rd ed.). https://doi.org/10.1002/9783527613984

Güler, C., Kurt, M. A., Alpaslan, M., & Akbulut, C. (2012). Assessment of the impact of anthropogenic activities on the groundwater hydrology and chemistry in Tarsus coastal plain (Mersin, SE Turkey) using fuzzy

clustering, multivariate statistics and GIS techniques. Journal of Hydrology, 414–415, 435–451. https://doi.org/10.1016/j.jhydrol.2011.11.021

Hecht, A., Pinardi, N., & Robinson, A. R. (1988). Currents, Water Masses, Eddies and Jets in the Mediterranean Levantine Basin. Journal of Physical Oceanography, 18(10), 1320–1353. https://doi.org/10.1175/1520-0485(1988)018<1320:CWMEAJ>2.0.CO;2

Hoos, A. B., Robinson, J. A., Aycock, R. A., Knight, R., & Woodside, M. D. (2000). Sources, instream transport, and trends of nitrogen, phosphorus, and sediment in the lower Tennessee River basin, 1980-96. Water-Resources Investigations Report. https://api.semanticscholar.org/CorpusID:126605591

Hu, C., Muller-Karger, F. E., & Swarzenski, P. W. (2006). Hurricanes, submarine groundwater discharge, and Florida's red tides. Geophysical Research Letters, 33(11). https://doi.org/10.1029/2005GL025449

Hugh-Jones, D. (2023). ggmagnify: Create a Magnified Inset of Part of a "ggplot" Object. https://github.com/hughjonesd/ggmagnify

Hwang, D. W., Lee, Y. W., & Kim, G. (2005). Large submarine groundwater discharge and benthic eutrophication in Bangdu Bay on volcanic Jeju Island, Korea. Limnology and Oceanography, 50(5), 1393–1403. https://doi.org/10.4319/lo.2005.50.5.1393

Isola, I., Bini, M., Ribolini, A., Zanchetta, G., & D'Agata, A. L. (2017). Geomorphology of the Ceyhan River lower plain (Adana Region, Turkey). Journal of Maps, 13(2), 133–141. https://doi.org/10.1080/17445647.2016.1274684

Jassim, F. A., & Altaany, F. H. (2013). Image Interpolation Using Kriging Technique for Spatial Data.

Jayne, S., Roemmich, D., Zilberman, N., Riser, S., Johnson, K., Johnson, G., & Piotrowicz, S. (2017). The Argo Program: Present and Future. Oceanography, 30(2), 18–28. https://doi.org/10.5670/oceanog.2017.213

Jenkins, W. J. (2003). 6.08—Tracers of Ocean Mixing. In H. D. Holland & K. K. Turekian (Eds.), Treatise on Geochemistry (pp. 223–246). Pergamon. https://doi.org/10.1016/B0-08-043751-6/06110-7

Kassambara, A. (2023a). ggpubr: "ggplot2" Based Publication Ready Plots. https://CRAN.R-project.org/package=ggpubr

Kassambara, A. (2023b). rstatix: Pipe-Friendly Framework for Basic Statistical Tests. https://CRAN.R-project.org/package=rstatix

Kehl, C., Nooteboom, P. D., Kaandorp, M. L. A., & van Sebille, E. (2023). Efficiently simulating Lagrangian particles in large-scale ocean flows—Data structures and their impact on geophysical applications. Computers & Geosciences, 175, 105322. https://doi.org/10.1016/j.cageo.2023.105322

Knee, K. L., & Paytan, A. (2012). Submarine Groundwater Discharge: A Source of Nutrients, Metals, and Pollutants to the Coastal Ocean. In Treatise on Estuarine and Coastal Science (Vol. 4). Elsevier Inc. https://doi.org/10.1016/B978-0-12-374711-2.00410-1

Koçak, M., Kubilay, N., Tuğrul, S., & Mihalopoulos, N. (2010). Atmospheric nutrient inputs to the northern levantine basin from a long-term observation:

Sources and comparison with riverine inputs. Biogeosciences, 7(12), 4037–4050. https://doi.org/10.5194/bg-7-4037-2010

Kohout, F. A. (1966). Submarine springs: A neglected phenomenon of coastal hydrology. Hydrology, 26, 391–413.

Kolker, D., Bookman, R., Herut, B., David, N., & Silverman, J. (2021). An Initial Assessment of the Contribution of Fresh Submarine Ground Water Discharge to the Alkalinity Budget of the Mediterranean Sea. Journal of Geophysical Research: Oceans, 126(8), 1–10. https://doi.org/10.1029/2020JC017085

Kousa, A., Komulainen, H., Hatakka, T., Backman, B., & Hartikainen, S. (2021). Variation in groundwater manganese in Finland. Environmental Geochemistry and Health, 43(3), 1193–1211. https://doi.org/10.1007/s10653-020-00643-x

Krest, J. M., & Moore, W. S. (1999). 226Ra and 228Ra in the mixing zones of the Mississippi and Atchafalaya Rivers: Indicators of groundwater input.

Krom, M. D., Emeis, K. C., & Van Cappellen, P. (2010). Why is the Eastern Mediterranean phosphorus limited? Progress in Oceanography, 85(3–4), 236–244. https://doi.org/10.1016/j.pocean.2010.03.003

Krom, M. D., Herut, B., & Mantoura, R. F. C. (2004). Nutrient budget for the Eastern Mediterranean: Implications for phosphorus limitation. Limnology and Oceanography, 49(5), 1582–1592. https://doi.org/10.4319/lo.2004.49.5.1582

Kwon, E. Y., Kim, G., Primeau, F., Moore, W. S., Cho, H., DeVries, T., Sarmiento, J. L., Charette, M. A., & Cho, Y. (2014). Global estimate of submarine groundwater discharge based on an observationally constrained radium isotope model. Geophysical Research Letters, 41(23), 8438–8444. https://doi.org/10.1002/2014GL061574

Lecher, A. L., Mackey, K., Kudela, R., Ryan, J., Fisher, A., Murray, J., & Paytan, A. (2015). Nutrient loading through submarine groundwater discharge and phytoplankton growth in Monterey bay, CA. Environmental Science and Technology, 49(11), 6665–6673. https://doi.org/10.1021/acs.est.5b00909

Lecher, A. L., Mackey, K. R. M., & Paytan, A. (2017). River and Submarine Groundwater Discharge Effects on Diatom Phytoplankton Abundance in the Gulf of Alaska. Hydrology, 4(4). https://doi.org/10.3390/hydrology4040061

Lilkendey, J., Pisternick, T., Neumann, S. I., Dumur Neelayya, D., Bröhl, S., Neehaul, Y., & Moosdorf, N. (2019). Fresh Submarine Groundwater Discharge Augments Growth in a Reef Fish. Frontiers in Marine Science, 6(October), 1–11. https://doi.org/10.3389/fmars.2019.00613

Lin, S. (2023). Phosphate limitation and ocean acidification co-shape phytoplankton physiology and community structure. Nature Communications, 14(1), 2699. https://doi.org/10.1038/s41467-023-38381-0

Luijendijk, E., Gleeson, T., & Moosdorf, N. (2020). Fresh groundwater discharge insignificant for the world's oceans but important for coastal ecosystems.

Nature Communications, 11(1). https://doi.org/10.1038/s41467-020-15064-8

Maidment, D. R. (1993). Handbook of hydrology (Issue 631.587). McGraw-Hill,.

Malanotte-Rizzoli, P., Artale, V., Borzelli-Eusebi, G. L., Brenner, S., Crise, A., Gacic, M., Kress, N., Marullo, S., Ribera d'Alcalà, M., Sofianos, S., Tanhua, T., Theocharis, A., Alvarez, M., Ashkenazy, Y., Bergamasco, A., Cardin, V., Carniel, S., Civitarese, G., D'Ortenzio, F., … Triantafyllou, G. (2014). Physical forcing and physical/biochemical variability of the Mediterranean Sea: A review of unresolved issues and directions for future research. Ocean Science, 10(3), 281–322. https://doi.org/10.5194/os-10-281-2014

Manca, B., Burca, M., Giorgetti, A., Coatanoan, C., Garcia, M.-J., & Iona, A. (2004). Physical and biochemical averaged vertical profiles in the Mediterranean regions: An important tool to trace the climatology of water masses and to validate incoming data from operational oceanography. Journal of Marine Systems, 48(1–4), 83–116. https://doi.org/10.1016/j.jmarsys.2003.11.025

Mariotti, A., Vittoria Struglia, M., Zeng, N., & Lau, K.-M. (2002). The Hydrological Cycle in the Mediterranean Region and Implications for the Water Budget of the Mediterranean Sea. Journal of Climate, 15(13), 1674–1690. https://doi.org/10.1175/1520-0442(2002)015\textless{}1674:THCITM\textgreater{}2.0.CO;2

Mayfield, K. K., Eisenhauer, A., Santiago Ramos, D. P., Higgins, J. A., Horner, T. J., Auro, M., Magna, T., Moosdorf, N., Charette, M. A., Gonneea, M. E., Brady, C. E., Komar, N., Peucker-Ehrenbrink, B., & Paytan, A. (2021). Groundwater discharge impacts marine isotope budgets of Li, Mg, Ca, Sr, and Ba. Nature Communications, 12(1), 1–9. https://doi.org/10.1038/s41467-020-20248-3

Mears, C., Thomas, H., Henderson, P. B., Charette, M. A., MacIntyre, H., Dehairs, F., Monnin, C., & Mucci, A. (2020). Using 226Ra and 228Ra isotopes to distinguish water mass distribution in the Canadian Arctic Archipelago. Biogeosciences, 17(20), 4937–4959. https://doi.org/10.5194/bg-17-4937-2020

Menna, M., Gerin, R., Notarstefano, G., Mauri, E., Bussani, A., Pacciaroni, M., & Poulain, P.-M. (2021). On the Circulation and Thermohaline Properties of the Eastern Mediterranean Sea. Frontiers in Marine Science, 8, 671469. https://doi.org/10.3389/fmars.2021.671469

Michael, H. A., Charette, M. A., & Harvey, C. F. (2011). Patterns and variability of groundwater flow and radium activity at the coast: A case study from Waquoit Bay, Massachusetts. Marine Chemistry, 127(1–4), 100–114. https://doi.org/10.1016/J.MARCHEM.2011.08.001

Montiel, D., Lamore, A., Stewart, J., & Dimova, N. (2019). Is Submarine Groundwater Discharge (SGD) Important for the Historical Fish Kills and Harmful Algal Bloom Events of Mobile Bay? Estuaries and Coasts, 42(2), 470–493. https://doi.org/10.1007/s12237-018-0485-5

Moore, W. S. (1976). Sampling 228Ra in the deep ocean. Deep-Sea Research, 23, 647–651.

Moore, W. S. (1996). Large groundwater inputs to coastal waters revealed by 226Ra enrichments. Nature, 380(6575), 612–614. https://doi.org/10.1038/380612a0

Moore, W. S. (2003). Sources and fluxes of submarine groundwater discharge delineated by radium isotopes. Biogeochemistry, 66(1/2), 75–93. https://doi.org/10.1023/B:BIOG.0000006065.77764.a0

Moore, W. S. (2010). The Effect of Submarine Groundwater Discharge on the Ocean. Annual Review of Marine Science, 2(1), 59–88. https://doi.org/10.1146/annurev-marine-120308-081019

Moore, W. S. (2015). Inappropriate attempts to use distributions of 228Ra and 226Ra in coastal waters to model mixing and advection rates. Continental Shelf Research, 105, 95–100. https://doi.org/10.1016/j.csr.2015.05.014

Moore, W. S., Blanton, J. O., & Joye, S. B. (2006). Estimates of flushing times, submarine groundwater discharge, and nutrient fluxes to Okatee Estuary, South Carolina. Journal of Geophysical Research, 111(C9), C09006. https://doi.org/10.1029/2005JC003041

Moore, W. S., & Reid, D. F. (1973). Extraction of radium from natural waters using manganese-impregnated acrylic fibers. Journal of Geophysical Research (1896-1977), 78(36), 8880–8886. https://doi.org/10.1029/JC078i036p08880

Moore, W. S., Sarmiento, J. L., & Key, R. M. (2008). Submarine groundwater discharge revealed by 228Ra distribution in the upper Atlantic Ocean. Nature Geoscience, 1(5), 309–311. https://doi.org/10.1038/ngeo183

Moore, W. S., & Shaw, T. J. (2008). Fluxes and behavior of radium isotopes, barium, and uranium in seven Southeastern US rivers and estuaries. Marine Chemistry, 108(3–4), 236–254. https://doi.org/10.1016/j.marchem.2007.03.004

Nazik, L., Poyraz, M., & Karabıyıkoğlu, M. (2019). Karstic Landscapes and Landforms in Turkey. In C. Kuzucuoğlu, A. Çiner, & N. Kazancı (Eds.), Landscapes and Landforms of Turkey (pp. 181–196). Springer International Publishing. https://doi.org/10.1007/978-3-030-03515-0_5

Neuwirth, E. (2022). RColorBrewer: ColorBrewer Palettes. https://CRAN.R-project.org/package=RColorBrewer

Ollivier, P., Claude, C., Radakovitch, O., & Hamelin, B. (2008). TIMS measurements of 226Ra and 228Ra in the Gulf of Lion, an attempt to quantify submarine groundwater discharge. Marine Chemistry, 109(3–4), 337–354. https://doi.org/10.1016/j.marchem.2007.08.006

Ooms, J. (2023). writexl: Export Data Frames to Excel “xlsx” Format. https://CRAN.R-project.org/package=writexl

Özsoy, E., Hecht, A., Ünlüata, Ü., Brenner, S., Sur, H. I., Bishop, J., Latif, M. A., Rozentraub, Z., & Oğuz, T. (1993). A synthesis of the Levantine Basin circulation and hydrography, 1985–1990. Deep Sea Research Part II:

Topical Studies in Oceanography, 40(6), 1075–1119. https://doi.org/10.1016/0967-0645(93)90063-S

Paerl, H. W. (1997). Coastal eutrophication and harmful algal blooms: Importance of atmospheric deposition and groundwater as “new” nitrogen and other nutrient sources. Limnology and Oceanography, 42(5part2), 1154–1165. https://doi.org/10.4319/lo.1997.42.5_part_2.1154

Paerl, H. W., & Otten, T. G. (2013). Harmful Cyanobacterial Blooms: Causes, Consequences, and Controls. Microbial Ecology, 65(4), 995–1010. https://doi.org/10.1007/s00248-012-0159-y

Parise, M., Gabrovsek, F., Kaufmann, G., & Ravbar, N. (2018). Recent advances in karst research: From theory to fieldwork and applications. Geological Society, London, Special Publications, 466(1), 1–24. https://doi.org/10.1144/SP466.26

Paytan, A., Shellenbarger, G. G., Street, J. H., Gonneea, M. E., Davis, K., Young, M. B., & Moore, W. S. (2006). Submarine groundwater discharge: An important source of new inorganic nitrogen to coral reef ecosystems. Limnology and Oceanography, 51(1), 343–348. https://doi.org/10.4319/lo.2006.51.1.0343

Peterson, B. G., & Carl, P. (2020). PerformanceAnalytics: Econometric Tools for Performance and Risk Analysis. https://CRAN.R-project.org/package=PerformanceAnalytics

Polat, S. (2007). Seasonal Dynamics of Phytoplankton in a Coastal Marine Ecosystem: İskenderun Bay, Northeastern Mediterranean Sea. Fresenius Environmental Bulletin, 16(7), 8.

Posit team. (2023). RStudio: Integrated Development Environment for R. Posit Software, PBC. http://www.posit.co/

Powley, H. R., Cappellen, P. Van, & Krom, M. D. (2017). Nutrient Cycling in the Mediterranean Sea: The Key to Understanding How the Unique Marine Ecosystem Functions and Responds to Anthropogenic Pressures. In B. Fuerst-Bjelis (Ed.), Mediterranean Identities. IntechOpen. https://doi.org/10.5772/intechopen.70878

Powley, H. R., Krom, M. D., & Van Cappellen, P. (2016). Circulation and oxygen cycling in the Mediterranean Sea: Sensitivity to future climate change: OXYGEN CYCLING IN THE MEDITERRANEAN SEA. Journal of Geophysical Research: Oceans, 121(11), 8230–8247. https://doi.org/10.1002/2016JC012224

Pujo-Pay, M., Conan, P., Oriol, L., Cornet-Barthaux, V., Falco, C., Ghiglione, J. F., Goyet, C., Moutin, T., & Prieur, L. (2011). Integrated survey of elemental stoichiometry (C, N, P) from the western to eastern Mediterranean Sea. Biogeosciences, 8(4), 883–899. https://doi.org/10.5194/bg-8-883-2011

QGIS Development Team. (2022). QGIS Geographic Information System. QGIS Association. httpswww.qgis.org

R Core Team. (2022). R: A Language and Environment for Statistical Computing. R Foundation for Statistical Computing. https://www.R-project.org/

Rapaglia, J. P., Ferrarin, C., Zaggia, L., Moore, W. S., Umgiesser, G., García-Solsona, E., García-Orellana, J., & Masqué, P. (2010). Investigation of residence time and groundwater flux in Venice Lagoon: Comparing radium isotope and hydrodynamic models. Journal of Environmental Radioactivity, 101 7, 571–581.

Redfield, A. C. (1963). The influence of organisms on the composition of seawater. The Sea, 2, 26–77.

Robinson, A. R., Golnaraghi, M., Leslie, W. G., Artegiani, A., Hecht, A., Lazzoni, E., Michelato, A., Sansone, E., Theocharis, A., & Ünlüata, Ü. (1991). The eastern Mediterranean general circulation: Features, structure and variability. Dynamics of Atmospheres and Oceans, 15(3–5), 215–240. https://doi.org/10.1016/0377-0265(91)90021-7

Robinson, A. R., Leslie, W. G., Theocharis, A., & Lascaratos, A. (2001). Mediterranean Sea Circulation. In Encyclopedia of Ocean Sciences (pp. 1689–1705). Elsevier. https://doi.org/10.1006/rwos.2001.0376

Rodellas, V., Garcia-Orellana, J., Masqué, P., Feldman, M., Weinstein, Y., & Boyle, E. A. (2015). Submarine groundwater discharge as a major source of nutrients to the Mediterranean Sea. Proceedings of the National Academy of Sciences of the United States of America, 112(13), 3926–3930. https://doi.org/10.1073/pnas.1419049112

Rodellas, V., Stieglitz, T. C., Tamborski, J. J., Beek, P., Andrisoa, A., & Cook, P. G. (2021). Conceptual uncertainties in groundwater and porewater fluxes

estimated by radon and radium mass balances. Limnology and Oceanography, 66(4), 1237–1255. https://doi.org/10.1002/lno.11678

Sanchez-Cabeza, J. A., Ortega, M., Merino, J., & Masqué, P. (2002). Long-term box modelling of 137Cs in the Mediterranean Sea. Journal of Marine Systems, 33–34, 457–472. https://doi.org/10.1016/S0924-7963(02)00071-4

Santos, I. R., Chen, X., Lecher, A. L., Sawyer, A. H., Moosdorf, N., Rodellas, V., Tamborski, J., Cho, H.-M., Dimova, N., Sugimoto, R., Bonaglia, S., Li, H., Hajati, M.-C., & Li, L. (2021). Submarine groundwater discharge impacts on coastal nutrient biogeochemistry. Nature Reviews Earth & Environment, 2(5), 307–323. https://doi.org/10.1038/s43017-021-00152-0

Santos, I. R., Eyre, B. D., & Huettel, M. (2012). The driving forces of porewater and groundwater flow in permeable coastal sediments: A review. Estuarine, Coastal and Shelf Science, 98, 1–15. https://doi.org/10.1016/j.ecss.2011.10.024

Savatier, M., & Rocha, C. (2021). Rethinking tracer-based (Ra, Rn, salinity) approaches to estimate point-source submarine groundwater discharge (SGD) into coastal systems. Journal of Hydrology, 598, 126247. https://doi.org/10.1016/j.jhydrol.2021.126247

Sow, M. M., Majdi, N., Muylaert, K., Tackx, M. L. M., Julien, F., Probst, J.-L., Mialet, B., Sutra, C., Probst, A., Thébault, J. M., Kenarlikdjian, M., & Gerino, M. (2016). Retention of nutrients, suspended particulate matter and phytoplankton in a pondage associated with a run-of-the-river type hydroelectric power plant. Ecohydrology, 9, 229–237.

Sur, H. İ., Özsoy, E., & Ünlüata, Ü. (1992). Simultaneous deep Deep water formation Intermediate water formation Convection Northem Levantine and intermediate depth convection Wmter 1992 in the Northem Levantine Sea, winter 1992. Oceanologica Acta, 1(16), 33–43.

Tamborski, J., Cochran, J. K., Bokuniewicz, H., Heilbrun, C., Garcia-Orellana, J., Rodellas, V., & Wilson, R. (2020). Radium Mass Balance Sensitivity Analysis for Submarine Groundwater Discharge Estimation in Semi-Enclosed Basins: The Case Study of Long Island Sound. Frontiers in Environmental Science, 8, 108. https://doi.org/10.3389/fenvs.2020.00108

Taniguchi, M., Burnett, W. C., Cable, J. E., & Turner, J. V. (2002). Investigation of submarine groundwater discharge. Hydrological Processes, 16(11), 2115–2129. https://doi.org/10.1002/hyp.1145

Taniguchi, M., Dulai, H., Burnett, K. M., Santos, I. R., Sugimoto, R., Stieglitz, T., Kim, G., Moosdorf, N., & Burnett, W. C. (2019). Submarine Groundwater Discharge: Updates on Its Measurement Techniques, Geophysical Drivers, Magnitudes, and Effects. Frontiers in Environmental Science, 7(October), 1–26. https://doi.org/10.3389/fenvs.2019.00141

Trezzi, G., Garcia-Orellana, J., Rodellas, V., Masqué, P., Garcia-Solsona, E., & Andersson, P. S. (2017). Assessing the role of submarine groundwater discharge as a source of Sr to the Mediterranean Sea. Geochimica et Cosmochimica Acta, 200, 42–54. https://doi.org/10.1016/j.gca.2016.12.005

Tugrul, S., Ozhan, K., & Akcay, I. (2019). Assessment of trophic status of the northeastern Mediterranean coastal waters: Eutrophication classification

tools revisited. Environmental Science and Pollution Research, 26(15), 14742–14754. https://doi.org/10.1007/s11356-018-2529-6

Utsunomiya, T., Hata, M., Sugimoto, R., Honda, H., Kobayashi, S., Miyata, Y., Yamada, M., Tominaga, O., Shoji, J., & Taniguchi, M. (2017). Higher species richness and abundance of fish and benthic invertebrates around submarine groundwater discharge in Obama Bay, Japan. Journal of Hydrology: Regional Studies, 11, 139–146. https://doi.org/10.1016/j.ejrh.2015.11.012

Vasylenko, A., Vasylenko, L., Fedorenko, S., Zhukova, O., & Honcharenko, A. (2018). ESTIMATION OF WATER ECOSYSTEM STRUCTURAL-FUNCTIONAL CHANGES AS A RESULT OF CLIMATE CHANGES. https://api.semanticscholar.org/CorpusID:134218260

Vinson, D. S., Tagma, T., Bouchaou, L., Dwyer, G. S., Warner, N. R., & Vengosh, A. (2013). Occurrence and mobilization of radium in fresh to saline coastal groundwater inferred from geochemical and isotopic tracers (Sr, S, O, H, Ra, Rn). Applied Geochemistry, 38, 161–175. https://doi.org/10.1016/j.apgeochem.2013.09.004

Wang, G., Jing, W., Wang, S., Xu, Y., Wang, Z., Zhang, Z., Li, Q., & Dai, M. (2014). Coastal acidification induced by tidal-driven submarine groundwater discharge in a coastal coral reef system. Environmental Science and Technology, 48(22), 13069–13075. https://doi.org/10.1021/es5026867

Wei, T., & Simko, V. (2021). R package “corrplot”: Visualization of a Correlation Matrix. https://github.com/taiyun/corrplot

Weinstein, Y., Less, G., Kafri, U., & Herut, B. (2006). Submarine groundwater discharge in the southeastern Mediterranean (Israel). In Radioactivity in the Environment (Vol. 8, Issue C). Elsevier Masson SAS. https://doi.org/10.1016/S1569-4860(05)08029-0

Weinstein, Y., Yechieli, Y., Shalem, Y., Burnett, W. C., Swarzenski, P. W., & Herut, B. (2011). What is the role of fresh groundwater and recirculated seawater in conveying nutrients to the coastal ocean? Environmental Science and Technology, 45(12), 5195–5200. https://doi.org/10.1021/es104394r

Wessel, P., Luis, J. F., Uieda, L., Scharroo, R., Wobbe, F., Smith, W. H. F., & Tian, D. (2019). The Generic Mapping Tools Version 6. Geochemistry, Geophysics, Geosystems, 20(11), 5556–5564. https://doi.org/10.1029/2019GC008515

Wickham, H., Averick, M., Bryan, J., Chang, W., McGowan, L. D., François, R., Grolemund, G., Hayes, A., Henry, L., Hester, J., Kuhn, M., Pedersen, T. L., Miller, E., Bache, S. M., Müller, K., Ooms, J., Robinson, D., Seidel, D. P., Spinu, V., … Yutani, H. (2019). Welcome to the tidyverse. Journal of Open Source Software, 4(43), 1686. https://doi.org/10.21105/joss.01686

Wickham, H., & Bryan, J. (2023). readxl: Read Excel Files. https://CRAN.R-project.org/package=readxl

Wickham, H., & Seidel, D. (2022). scales: Scale Functions for Visualization. https://CRAN.R-project.org/package=scales

Wildhaber, Y. S. (2013). The impact of fine sediments in small rivers: Method development and effects on brown trout redds. https://api.semanticscholar.org/CorpusID:129750492

Yemenicioglu, S., & Tunc, S. C. (2013). Geology and Geochemistry of Recent Sediments from the Mediterranean Sea: Sediment Texture of Northeastern Mediterranean Basin. Open Journal of Geology, 03(06), 371–378. https://doi.org/10.4236/ojg.2013.36042

Yilmaz, A., Basturk, O., Saydam, C., Ediger, D., Yilmaz, K., & Hatipoglu, E. (1992). Eutrophication in Iskenderun Bay, north-eastern Mediterranean. Science of the Total Environment, SUPPL., 705–717. https://doi.org/10.1016/b978-0-444-89990-3.50062-6

Yılmaz, A., & Tuğrul, S. (1998). The effect of cold- and warm-core eddies on the distribution and stoichiometry of dissolved nutrients in the northeastern Mediterranean. Journal of Marine Systems, 16(3–4), 253–268. https://doi.org/10.1016/S0924-7963(97)00022-5

Yucel, N. (2018). Spatio-temporal variability of the size-fractionated primary production and chlorophyll in the Levantine Basin (northeastern Mediterranean). Oceanologia, 60(3), 288–304. https://doi.org/10.1016/j.oceano.2017.12.003

Zektser, I. S., & Everett, L. G. (2004). Groundwater resources of the world and their use. IhP Series on Groundwater. No. 6, 6, 1–346.

Zektser, I. S., Everett, L. G., & Dzhamalov, R. G. (2006). Submarine groundwater (1st ed.). CRC Press. https://doi.org/10.1201/9781420005257

APPENDICES

A. Sea sample stations

Sample ID	Date	Station	Type	Latitude (decimal degrees)	Longitude (decimal degrees)	Depth (m)
1	10/13/2021	Offshore Surface (in-Series) 1	Seawater	36.0460	33.9320	3
2	10/13/2021	Offshore Surface (in-Series) 2	Seawater	36.0460	33.9320	3
3	10/13/2021	Offshore Surface (Single)	Seawater	33.9320	36.0460	3
4	10/13/2021	Offshore Deep	Seawater	36.0460	33.9320	580
5	10/13/2021	Coastal Surface (in-Series) 1	Seawater	36.3050	33.8800	3
6	10/13/2021	Coastal Surface (in-Series) 2	Seawater	36.3050	33.8800	3
7	10/13/2021	Coastal Surface (Single)	Seawater	33.8800	36.3050	3
8	10/13/2021	Coastal Deep 1	Seawater	36.3050	33.8800	20
9	10/13/2021	Coastal Deep 2	Seawater	36.3050	33.8800	20
62*	15.04.2022	St-005 109 Double	Seawater	36.2431	35.6657	3

Sample ID	Date	Station	Type	Latitude (decimal degrees)	Longitude (decimal degrees)	Depth (m)
63	13.04.2022	St-012	Seawater	36.1697	33.8571	3
64	13.04.2022	St-012	Seawater	36.1697	33.8571	49
65	13.04.2022	St-012	Seawater	36.1697	33.8571	20
66	13.04.2022	St-013	Seawater	36.0986	33.3970	3
67	13.04.2022	St-013	Seawater	36.0986	33.3970	30
68	13.04.2022	St-013	Seawater	36.0986	33.3970	92
69	14.04.2022	St-016	Seawater	35.6977	32.9087	3
70	14.04.2022	St-016	Seawater	35.6977	32.9087	1230
71	14.04.2022	St-016	Seawater	35.6977	32.9087	600
72	14.04.2022	St-016	Seawater	35.6977	32.9087	250
73	14.04.2022	St-016	Seawater	35.6977	32.9087	100
74	14.04.2022	St-015	Seawater	35.8710	32.9624	3
75	14.04.2022	St-015	Seawater	35.8710	32.9624	1177
76	14.04.2022	St-015	Seawater	35.8710	32.9624	1121
77	14.04.2022	St-015	Seawater	35.8710	32.9624	600
78	14.04.2022	St-015	Seawater	35.8710	32.9624	300
79	14.04.2022	St-015	Seawater	35.8710	32.9624	160
80	14.04.2022	St-015	Seawater	35.8710	32.9624	30
81	14.04.2022	St-014	Seawater	36.0074	32.9618	3
82	14.04.2022	St-014	Seawater	36.0074	32.9618	339
83	14.04.2022	St-014	Seawater	36.0074	32.9618	270
84	14.04.2022	St-014	Seawater	36.0074	32.9618	160
85	14.04.2022	St-014	Seawater	36.0074	32.9618	30
86	14.04.2022	St-001	Seawater	36.0000	34.2294	3
87	15.04.2022	St-001	Seawater	36.0000	34.2294	917
88	15.04.2022	St-001	Seawater	36.0000	34.2294	875
89	15.04.2022	St-001	Seawater	36.0000	34.2294	600
90	15.04.2022	St-001	Seawater	36.0000	34.2294	250
91	15.04.2022	St-001	Seawater	36.0000	34.2294	100
92	15.04.2022	St-001	Seawater	36.0000	34.2294	40
93	15.04.2022	St-002	Seawater	35.9691	35.0476	3
94	15.04.2022	St-002	Seawater	35.9691	35.0476	958
95	15.04.2022	St-002	Seawater	35.9691	35.0476	600
96	15.04.2022	St-002	Seawater	35.9691	35.0476	250
97	15.04.2022	St-002	Seawater	35.9691	35.0476	40

Sample ID	Date	Station	Type	Latitude (decimal degrees)	Longitude (decimal degrees)	Depth (m)
98	15.04.2022	St-002	Seawater	35.9691	35.0476	1083
99	15.04.2022	St-003	Seawater	35.9499	35.3147	3
100	15.04.2022	St-003	Seawater	35.9499	35.3147	1014
101	15.04.2022	St-003	Seawater	35.9499	35.3147	600
102	15.04.2022	St-003	Seawater	35.9499	35.3147	250
103	15.04.2022	St-003	Seawater	35.9499	35.3147	40
104	15.04.2022	St-004	Seawater	36.0911	35.5133	3
105	15.04.2022	St-004	Seawater	36.0911	35.5133	340
106	15.04.2022	St-004	Seawater	36.0911	35.5133	225
107	15.04.2022	St-004	Seawater	36.0911	35.5133	150
108	15.04.2022	St-004	Seawater	36.0911	35.5133	40
109*	15.04.2022	St-005	Seawater	36.2431	35.6657	3
110	15.04.2022	St-005	Seawater	36.2431	35.6657	99
111	15.04.2022	St-005	Seawater	36.2431	35.6657	40
112	15.04.2022	St-018	Seawater	36.4823	35.9019	3
113	15.04.2022	St-006	Seawater	36.5897	35.9805	3
114	15.04.2022	St-006	Seawater	36.5897	35.9805	71
115	15.04.2022	St-006	Seawater	36.5897	35.9805	30
116	16.04.2022	St-007	Seawater	36.7182	36.0254	3
117	16.04.2022	St-007	Seawater	36.7182	36.0254	62
118	16.04.2022	St-007	Seawater	36.7182	36.0254	50
119	16.04.2022	St-007	Seawater	36.7182	36.0254	20
120*	16.04.2022	St-019	Seawater	36.7739	36.1248	3
121*	16.04.2022	St-020	Seawater	36.8183	35.9897	3
122	16.04.2022	St-021	Seawater	36.7174	35.8198	3
123	16.04.2022	St-008	Seawater	36.6117	35.7738	3
124	16.04.2022	St-008	Seawater	36.6117	35.7738	69
125	16.04.2022	St-008	Seawater	36.6117	35.7738	25
126	16.04.2022	St-008 125 Double	Seawater	36.6117	35.7738	25
127	16.04.2022	St-009	Seawater	36.4641	35.4622	3
128	16.04.2022	St-009	Seawater	36.4641	35.4622	70
129	16.04.2022	St-009	Seawater	36.4641	35.4622	30

Sample ID	Date	Station	Type	Latitude (decimal degrees)	Longitude (decimal degrees)	Depth (m)
130	16.04.2022	St-009 129 Double	Seawater	36.4641	35.4622	30
131	16.04.2022	St-017	Seawater	36.3407	34.9669	3
132	16.04.2022	St-017	Seawater	36.3407	34.9669	105
133	16.04.2022	St-017	Seawater	36.3407	34.9669	30
134	16.04.2022	St-017 133 Double	Seawater	36.3407	34.9669	30
135	16.04.2022	St-010	Seawater	36.6813	34.6999	3
136	16.04.2022	St-010	Seawater	36.6813	34.6999	47
137	16.04.2022	St-010	Seawater	36.6813	34.6999	7
138	16.04.2022	St-011	Seawater	36.5540	34.3070	3
139	16.04.2022	St-011	Seawater	36.5540	34.3070	70
140	16.04.2022	St-011	Seawater	36.5540	34.3070	30
141	16.04.2022	St-019 120 Double	Seawater	36.7739	36.1248	3
142	16.04.2022	St-020 121 Double	Seawater	36.8183	35.9897	3
143	31.08.2022	St-012	Seawater	36.1702	33.8563	3
144	31.08.2022	St-012	Seawater	36.1702	33.8563	51
145	31.08.2022	St-012	Seawater	36.1702	33.8563	20
146	31.08.2022	St-013	Seawater	36.0898	33.3899	3
147	31.08.2022	St-013	Seawater	36.0898	33.3899	110
148	31.08.2022	St-013	Seawater	36.0898	33.3899	30
149	31.08.2022	St-014	Seawater	36.0000	32.9500	364
150	31.08.2022	St-014	Seawater	36.0000	32.9500	3
151	31.08.2022	St-014	Seawater	36.0000	32.9500	460
152	31.08.2022	St-014	Seawater	36.0000	32.9500	600
153	31.08.2022	St-014	Seawater	36.0000	32.9500	160
154	1.09.2022	St-014	Seawater	36.0000	32.9500	60
156	1.09.2022	St-015	Seawater	35.8500	32.9500	3
157	1.09.2022	St-015	Seawater	35.8500	32.9500	1118
158	1.09.2022	St-015	Seawater	35.8500	32.9500	1085

Sample ID	Date	Station	Type	Latitude (decimal degrees)	Longitude (decimal degrees)	Depth (m)
159	1.09.2022	St-015	Seawater	35.8500	32.9500	600
160	1.09.2022	St-015	Seawater	35.8500	32.9500	300
161	1.09.2022	St-015	Seawater	35.8500	32.9500	160
162	1.09.2022	St-015	Seawater	35.8500	32.9500	10
163	1.09.2022	St-016	Seawater	35.7000	32.9800	3
164	1.09.2022	St-016 163 Double	Seawater	35.7000	32.9800	3
165	1.09.2022	St-016	Seawater	35.7000	32.9800	3
166	1.09.2022	St-016 165 Double	Seawater	35.7000	32.9800	3
167	1.09.2022	St-016	Seawater	35.7000	32.9800	1212 1240
168	1.09.2022	St-016	Seawater	35.7000	32.9800	1158 1154
169	1.09.2022	St-016	Seawater	35.7000	32.9800	600
170	1.09.2022	St-016	Seawater	35.7000	32.9800	250
171	1.09.2022	St-016	Seawater	35.7000	32.9800	75
172	1.09.2022	St-016 171 Double	Seawater	35.7000	32.9800	75
173	1.09.2022	St-016	Seawater	35.7000	32.9800	75
174	1.09.2022	St-016 173 Double	Seawater	35.7000	32.9800	75
175	1.09.2022	St-016	Seawater	35.7000	32.9800	20
176	1.09.2022	St-001	Seawater	36.0000	34.2500	3
177	1.09.2022	St-001 176 Double	Seawater	36.0000	34.2500	3
178	1.09.2022	St-001	Seawater	36.0000	34.2500	3
179	1.09.2022	St-001 178 Double	Seawater	36.0000	34.2500	3
180	1.09.2022	St-001	Seawater	36.0000	34.2500	908
181	1.09.2022	St-001	Seawater	36.0000	34.2500	867

Sample ID	Date	Station	Type	Latitude (decimal degrees)	Longitude (decimal degrees)	Depth (m)
182	2.09.2022	St-001	Seawater	36.0000	34.2500	600
183	2.09.2022	St-001	Seawater	36.0000	34.2500	150
184	2.09.2022	St-001	Seawater	36.0000	34.2500	50
185	2.09.2022	St-001	Seawater	36.0000	34.2500	20
186	2.09.2022	St-002	Seawater	35.9833	35.0500	1092
187	2.09.2022	St-002	Seawater	35.9833	35.0500	3
188	2.09.2022	St-002	Seawater	35.9833	35.0500	1067
189	2.09.2022	St-002	Seawater	35.9833	35.0500	600
190	2.09.2022	St-002	Seawater	35.9833	35.0500	180
191	2.09.2022	St-002	Seawater	35.9833	35.0500	80
192	2.09.2022	St-002	Seawater	35.9833	35.0500	30
193	2.09.2022	St-035	Seawater	35.9067	35.0600	3
194	2.09.2022	St-035	Seawater	35.9067	35.0600	180
195	2.09.2022	St-035	Seawater	35.9067	35.0600	80
196	2.09.2022	St-035	Seawater	35.9067	35.0600	20
197	2.09.2022	St-003	Seawater	35.9444	35.2854	3
198	2.09.2022	St-003	Seawater	35.9444	35.2854	1094
199	2.09.2022	St-003	Seawater	35.9444	35.2854	600
200	2.09.2022	St-003	Seawater	35.9444	35.2854	160
201	2.09.2022	St-003	Seawater	35.9444	35.2854	80
202	2.09.2022	St-003	Seawater	35.9444	35.2854	20
203	2.09.2022	St-036	Seawater	36.0011	35.5612	3
204	2.09.2022	St-036	Seawater	36.0011	35.5612	180
205	2.09.2022	St-036	Seawater	36.0011	35.5612	80
206	2.09.2022	St-036	Seawater	36.0011	35.5612	30
207	2.09.2022	St-004	Seawater	36.0833	35.5167	364
208	2.09.2022	St-004	Seawater	36.0833	35.5167	140
209	2.09.2022	St-004	Seawater	36.0833	35.5167	80
210	2.09.2022	St-004	Seawater	36.0833	35.5167	20
211	2.09.2022	St-004	Seawater	36.0833	35.5167	3
212	2.09.2022	St-005	Seawater	36.2418	35.6696	101
213	2.09.2022	St-005	Seawater	36.2418	35.6696	60
214	2.09.2022	St-005	Seawater	36.2418	35.6696	3
215	2.09.2022	St-005	Seawater	36.2418	35.6696	20
216	3.09.2022	St-038	Seawater	36.4071	35.7324	3

Sample ID	Date	Station	Type	Latitude (decimal degrees)	Longitude (decimal degrees)	Depth (m)
217	3.09.2022	St-038	Seawater	36.4071	35.7324	75
218	3.09.2022	St-006	Seawater	36.4823	35.9019	45
219	3.09.2022	St-006	Seawater	36.4823	35.9019	33
220	3.09.2022	St-007	Seawater	36.5905	35.9807	3
221	3.09.2022	St-030	Seawater	36.5370	35.9500	3
222	3.09.2022	St-029	Seawater	36.6230	36.0470	3
223	3.09.2022	St-022	Seawater	36.6540	36.0990	60
224	3.09.2022	St-022	Seawater	36.6540	36.0990	31
225	3.09.2022	St-026	Seawater	36.7230	36.1370	3
226	3.09.2022	St-018	Seawater	36.7739	36.1248	3
227	3.09.2022	St-019	Seawater	36.8183	35.9897	49
228	3.09.2022	St-019	Seawater	36.8183	35.9897	20
229	3.09.2022	St-025	Seawater	36.8010	36.0490	3
230	3.09.2022	St-008	Seawater	36.7221	36.0253	3
231	3.09.2022	St-028	Seawater	36.6890	35.9730	55
232	3.09.2022	St-028	Seawater	36.6890	35.9730	30
233	3.09.2022	St-023	Seawater	36.6580	35.9080	3
234	3.09.2022	St-031	Seawater	36.6230	35.8580	3
235	3.09.2022	St-024	Seawater	36.7750	35.9040	3
236	3.09.2022	St-027	Seawater	36.7470	35.8660	3
237	3.09.2022	St-020	Seawater	36.7174	35.8198	3
238	3.09.2022	St-032	Seawater	36.6870	35.7740	3
239	3.09.2022	St-033	Seawater	36.6500	35.7190	3
240	3.09.2022	St-021	Seawater	36.6111	35.7751	60
241	3.09.2022	St-021	Seawater	36.6111	35.7751	20
242	3.09.2022	St-034	Seawater	36.5500	35.8230	3
243	3.09.2022	St-037	Seawater	36.5155	35.6597	67
244	3.09.2022	St-037	Seawater	36.5155	35.6597	20
245	3.09.2022	St-009	Seawater	36.4641	35.4626	3
246	3.09.2022	St-009	Seawater	36.4641	35.4626	74
247	3.09.2022	St-009	Seawater	36.4641	35.4626	60
248	3.09.2022	St-009	Seawater	36.4641	35.4626	20
249	3.09.2022	St-017	Seawater	36.3400	34.9667	3
250	3.09.2022	St-017	Seawater	36.3400	34.9667	106
251	3.09.2022	St-017	Seawater	36.3400	34.9667	80

Sample ID	Date	Station	Type	Latitude (decimal degrees)	Longitude (decimal degrees)	Depth (m)
252	3.09.2022	St-017	Seawater	36.3400	34.9667	44
253	3.09.2022	St-010	Seawater	36.6808	34.7009	50
254	3.09.2022	St-010	Seawater	36.6808	34.7009	3
255	3.09.2022	St-010	Seawater	36.6808	34.7009	30
256	3.09.2022	St-010	Seawater	36.6808	34.7009	15
257	4.09.2022	St-011	Seawater	36.5532	34.3078	3
258	4.09.2022	St-011	Seawater	36.5532	34.3078	75
259	4.09.2022	St-011	Seawater	36.5532	34.3078	55
260	4.09.2022	St-011	Seawater	36.5532	34.3078	16

B. Catchment sample stations

Sample ID	Date	Station	Type	Latitude (decimal degrees)	Longitude (decimal degrees)	Depth (m)
10	10/19/2021	METU Well SK5 (in-series) 1	Well	36.5688	34.2576	5
11	10/19/2021	METU Well SK5 (in-series) 2	Well	36.5688	34.2576	5
12	10/19/2021	METU Well SK5 (Single)	Well	36.5688	34.2576	5
13	10/19/2021	METU Well SK50 (in-series) 1	Well	36.5688	34.2576	50
14	10/19/2021	METU Well SK50 (in-series) 2	Well	36.5688	34.2576	50
15	10/19/2021	METU Well SK50 (Single)	Well	36.5688	34.2576	50
16	10/20/2021	Lamas River (in-series) 1	River	36.5580	34.2470	-
17	10/20/2021	Lamas River (in-series) 2	River	36.5580	34.2470	-
18	10/20/2021	Lamas River (Single)	River	36.5580	34.2470	-
19	12/11/2021	Gilindire Cave	Karstic Underground Lake	36.1309	33.4027	-

20	12/11/2021	Anamur River	River	36.0772	32.8734	-
21	12/11/2021	Anamur Well	Well	36.1013	33.0109	18
22	12/11/2021	Boğsak Well	Well	36.2702	33.8131	1.5
23	12/12/2021	Göksu River	River	36.3305	34.0285	-
24	12/12/2021	Göksu Well	Well	36.3428	34.0105	9
25	12/12/2021	Deliçay	River	36.8150	34.7078	-
26	12/12/2021	Berdan River	River	36.7528	34.9028	-
27	12/12/2021	Seyhan River	River	36.7850	35.0630	-
28	12/13/2021	Ceyhan River	River	36.6149	35.5898	-
29	12/13/2021	Dörtyol Well	Well	36.8861	36.1427	32
30	12/13/2021	Samandağ Well	Well	36.0683	35.9976	30
31	12/13/2021	Asi River – US	River	36.0459	35.9647	-
32	12/13/2021	Asi River – TR	River	36.0459	35.9647	-
33	12/14/2021	Tarsus Well	Well	36.8949	34.9604	120
34	12/15/2021	METU Well SK50 - US	Well	36.5688	34.2576	50
35	12/15/2021	METU Well SK50 - TR	Well	36.5688	34.2576	50
36	12/15/2021	Lamas River - US	River	36.5580	34.2470	-
37	12/15/2021	Lamas river - TR	River	36.5580	34.2470	-
38	3/2/2022	Anamur River	River	36.0772	32.8734	-
39	3/2/2022	Anamur Well	Well	36.1013	33.0109	18

40	3/2/2022	Gilindire Cave	Karstic Undergr ound Lake	36.1309	33.4027	-
41	3/2/2022	Boğsak Well	Well	36.2702	33.8131	1.5
42	3/2/2022	Göksu Well	Well	36.3428	34.0105	9
43	3/2/2022	Göksu River	River	36.3305	34.0285	-
44	3/3/2022	Berdan River	River	36.7528	34.9028	-
45	3/3/2022	Tarsus Well	Well	36.8949	34.9604	120
46	3/3/2022	Seyhan River	River	36.7850	35.0630	-
47	3/4/2022	Ceyhan River	River	36.6149	35.5898	-
48	3/4/2022	Dörtyol Well	Well	36.8861	36.1427	32
49	3/4/2022	Deliçay (Hatay) River	River	36.8334	36.1734	-
50	3/4/2022	Asi River	River	36.0477	35.9688	-
51	3/4/2022	Samandağ Well	Well	36.0683	35.9976	30
52	3/10/2022	Lamas River	River	36.5580	34.2470	-
53	3/10/2022	METU Well SK50	Well	36.5688	34.2576	50
261	14.9.2022	Gilindire Cave	Karstic Undergr ound Lake	36.1309	33.4027	-
262	14.9.2022	Anamur River	River	36.0772	32.8734	
263	14.9.2022	Anamur Well	Well	36.1013	33.0109	18
264	14.9.2022	Boğsak Well	Well	36.2702	33.8131	1.5
265	15.9.2022	Göksu River	River	36.3305	34.0285	

266	15.9.2022	Göksu Well-2	Well	36.3414	34.0101	
267	15.9.2022	Tarsus Well	Well	36.8949	34.9604	120
268	15.9.2022	Berdan River	River	36.7528	34.9028	
269	15.9.2022	Seyhan River	River	36.7850	35.0630	
270	16.9.2022	Ceyhan River	River	36.6149	35.5898	
271	16.9.2022	Dörtyol Well	Well	36.8861	36.1427	32
272	16.9.2022	Asi River	River	36.0477	35.9688	
273	16.9.2022	Samandağ Well	Well	36.0683	35.9976	30
274	16.9.2022	Samandağ Well	Well	36.0683	35.9976	30
275	17.9.2022	Deliçay	River	36.8150	34.7078	
276	20.9.2022	SK-50	Well	36.5688	34.2576	50
277	20.9.2022	SK-50 276 Double	Well	36.5688	34.2576	50
278	20.9.2022	SK-50	Well	36.5688	34.2576	50
279	20.9.2022	SK-50 278 Double	Well	36.5688	34.2576	50
280	20.9.2022	Lamas	River	36.5580	34.2470	
281	20.9.2022	Lamas 280 Double	River	36.5580	34.2470	
282	20.9.2022	Lamas	River	36.5580	34.2470	
283	20.9.2022	Lamas 282 Double	River	36.5580	34.2470	

C. Nutrient concentrations in groundwater samples

Station	Date	PO_4 (µM)	NO_3+NO_2 (µM)	NO_2 (µM)	NH_4 (µM)	Si (µM)	DIN (µM)
IMS 50	13.12.2021	0.03	649.80	0.22	0.09	321.00	649.89
Anamur	11.12.2021	0.16	0.94	0.41	0.97	58.21	1.91
Gilindire	12.12.2021	0.53	3.17	0.28	2.37	19.42	5.54
Boğsak	13.12.2021	0.23	1.37	0.47	1.34	39.57	2.71
Göksu 1	14.12.2021	7.82	46.94	0.25	45.91	226.15	92.85
Tarsus	13.12.2021	0.34	2.02	0.51	7.77	154.72	9.79
Dörtyol	11.12.2021	0.53	3.20	0.42	0.94	198.95	4.14
Samandağ	11.12.2021	0.40	2.38	0.60	2.44	73.09	4.82
Anamur	22.01.2022	0.67	498.66	0.11	2.18	34.88	500.84
Gilindire	22.01.2022	0.79	88.28	0.08	1.64	15.83	89.92
Boğsak	22.01.2022	0.61	103.93	0.21	2.82	31.21	106.75
Göksu 1	22.01.2022	0.83	1.98	0.07	36.11	30.98	38.09
Tarsus	23.01.2022	0.86	183.98	0.67	0.91	65.23	184.89
Dörtyol	23.01.2022	0.82	530.14	0.10	1.52	147.71	531.66
Samandağ	23.01.2022	0.83	171.40	0.57	1.48	151.60	172.88
IMS 50	28.02.2022	0.13	470.33	0.33	0.88	229.88	471.21
Anamur	02.03.2022	0.29	475.08	0.26	0.34	115.54	475.42
Gilindire	02.03.2022	0.18	107.81	0.36	2.38	62.57	110.19
Göksu 1	02.03.2022	6.02	2.88	0.13	43.33	220.24	46.21
Tarsus	03.03.2022	0.14	465.06	8.77	0.79	235.57	465.85
Dörtyol	04.03.2022	0.31	516.08	0.31	0.10	515.06	516.18
Samandağ	04.03.2022	0.28	515.53	5.86	1.07	304.03	516.60
IMS 50	26.04.2022	0.26	444.56	0.31	1.07	17.35	445.63
IMS 5	26.04.2022	0.34	387.10	0.29	0.68	93.98	387.78

Station	Date	PO_4 (µM)	NO_3+NO_2 (µM)	NO_2 (µM)	NH_4 (µM)	Si (µM)	DIN (µM)
Anamur	26.04.2022	0.34	483.33	0.26	6.09	30.79	489.42
Gilindire	26.04.2022	0.90	59.00	0.42	3.77	34.00	62.77
Boğsak	26.04.2022	0.31	188.23	0.55	1.07	39.33	189.30
Göksu 1	26.04.2022	10.99	3.35	0.29	33.33	60.70	36.68
Göksu 2	26.04.2022	0.57	0.74	0.08	18.18	63.37	18.92
Tarsus	26.04.2022	0.52	125.71	0.31	1.58	80.90	127.29
Dörtyol	27.04.2022	0.67	519.15	0.41	8.88	291.94	528.03
Samandağ	27.04.2022	0.14	603.33	7.78	2.66	168.33	605.99
IMS 50	26.05.2022	0.39	518.18	0.49	1.54	49.53	519.72
IMS 5	26.05.2022	0.35	501.33	0.24	1.22	133.32	502.55
Anamur	26.05.2022	0.29	495.67	0.36	1.37	57.81	497.04
Gilindire	26.05.2022	0.23	133.23	0.52	0.75	30.33	133.98
Boğsak	26.05.2022	0.28	215.25	0.31	1.29	6.60	216.54
Göksu 1	26.05.2022	8.59	6.59	0.14	49.61	79.99	56.20
Göksu 2	26.05.2022	0.73	1.61	0.05	1.04	100.83	2.65
Tarsus	26.05.2022	0.91	288.12	0.47	2.22	147.43	290.34
Dörtyol	26.05.2022	0.77	543.08	0.35	0.92	472.68	544.00
Samandağ	26.05.2022	0.14	603.33	7.78	2.66	168.33	605.99
IMS 50	22.06.2022	0.23	469.40	0.37	0.53	29.33	469.93
Anamur	22.06.2022	0.16	0.97	0.46	2.54	7.95	3.51
Boğsak	22.06.2022	0.17	1.01	0.42	1.10	24.56	2.11
Göksu 1	22.06.2022	6.10	36.61	0.20	40.49	64.71	77.10
Göksu 2	22.06.2022	0.76	4.57	0.33	1.76	47.94	6.33
Tarsus	23.06.2022	0.60	221.27	0.37	0.27	64.09	221.54
Dörtyol	23.06.2022	0.65	3.89	0.22	1.70	341.46	5.59
Samandağ	23.06.2022	0.11	0.65	0.30	1.42	24.94	2.07

Station	Date	PO_4 (µM)	NO_3+NO_2 (µM)	NO_2 (µM)	NH_4 (µM)	Si (µM)	DIN (µM)
Anamur	19.07.2022	0.37	2.20	0.44	2.25	24.34	4.45
Gilindire	19.07.2022	0.86	5.15	0.72	6.56	34.64	11.71
Boğsak	19.07.2022	0.33	1.98	1.25	1.48	33.29	3.46
Göksu 1	19.07.2022	6.46	38.77	0.38	47.38	100.97	86.15
Göksu 2	19.07.2022	0.59	3.56	0.44	0.59	47.35	4.15
Tarsus	20.07.2022	0.52	3.10	0.17	1.25	50.93	4.35
Dörtyol	20.07.2022	2.41	14.47	0.22	11.71	124.41	26.18
Samandağ	20.07.2022	0.21	1.26	0.76	2.46	116.35	3.72
IMS 50	21.07.2022	0.37	2.23	0.25	2.20	27.50	4.43
Anamur	14.09.2022	0.28	497.74	0.32	9.87	248.51	507.61
Gilindire	14.09.2022	0.32	170.32	0.10	13.00	107.63	183.32
Boğsak	14.09.2022	0.60	506.52	0.65		171.93	506.52
Göksu 1	15.09.2022	5.03	14.42	0.20	60.64	498.69	75.06
Göksu 2	15.09.2022	0.37	2.44	0.16	13.63	309.56	16.07
Tarsus	15.09.2022	1.14	270.86	0.17	14.60	485.06	285.46
Dörtyol	16.09.2022	0.74	565.71	0.15	12.95	809.42	578.66
Samandağ	16.09.2022	1.44	425.15	0.79	0.21	444.98	425.36
Anamur	18.10.2022	0.79	508.09	0.41	11.42	250.99	519.51
Gilindire	18.10.2022	1.46	194.85	0.28	12.60	110.14	207.45
Boğsak	18.10.2022	0.76	501.74	1.14	9.16	175.09	510.90
Göksu 1	18.10.2022	4.76	14.14	0.23	53.14	541.26	67.28
Göksu 2	18.10.2022	0.72	2.18	0.15	13.13	314.10	15.31
Tarsus	19.10.2022	0.55	284.72	2.93	2.45	532.47	287.17
Dörtyol	19.10.2022	0.58	562.45	0.26	12.22	1082.49	574.67
Samandağ	20.10.2022	1.04	424.96	0.91	1.36	519.35	426.32
IMS 50	23.11.2022	0.64	497.18	0.12	1.56	269.54	498.74

Station	Date	PO_4 (µM)	NO_3+NO_2 (µM)	NO_2 (µM)	NH_4 (µM)	Si (µM)	DIN (µM)
IMS 5	23.11.2022	0.13	390.51	0.16	1.30	430.21	391.81
Anamur	26.11.2022	2.03	745.94	10.10	24.65	247.18	770.59
Gilindire	26.11.2022	2.33	140.85	11.47	25.12	72.38	165.97
Boğsak	26.11.2022	2.29	439.43	10.64	25.73	128.71	465.16
Göksu 1	26.11.2022	8.89	4.43	0.10	53.06	440.61	57.49
Göksu 2	26.11.2022	2.05	2.74	0.09	21.21	333.03	23.95
IMS 50	25.11.2022	0.68	489.97	0.10	1.13	236.57	491.10
IMS 5	25.11.2022	0.60	425.66	0.18	1.39	490.51	427.05
Tarsus	23.11.2022	0.20	259.18	1.03	1.25	456.17	260.43
Dörtyol	24.11.2022	2.32	1162.45	19.99	25.32	337.87	1187.77
Samandağ	25.11.2022	1.06	324.38	1.13	0.96	494.00	325.34